PREPARATION, STRUCTURE AND ELECTRONIC PROPERTIES OF THE SERIES $RETiO_3$, RE ≡ La, Ce, Pr, Nd, Sm, Gd, Y, AND La_xY_{1-x}

DOCTOR OF PHILOSOPHY (1980)
(Chemistry)

McMASTER UNIVERSITY
Hamilton, Ontario

TITLE: Preparation, Structure and Electronic Properties of the Series $RETiO_3$, RE = La, Ce, Pr, Nd, Sm, Gd, Y, and La_xY_{1-x}.

AUTHOR: David A. MacLean, B.Sc. (Dalhousie University)

SUPERVISOR: Dr. J.E. Greedan

NUMBER OF PAGES: xiii, 168

ABSTRACT:

ABSTRACT

Members of the $RETiO_3$ series, RE = La, Ce, Pr, Nd, Gd, Y and La_xY_{1-x}, have been prepared and characterized. Single crystals (or crystals with a small volume of twinned component) of many of these phases have been obtained from the melt for the first time using Czochralski and Stockbarger techniques.

Crystal structures of selected members of this series have been solved using single crystal X-ray diffraction data. The solutions were complicated in some cases by twinning, but all phases were found to be isostructural with $GdFeO_3$, space group Pbnm. While most aspects of the structures varied smoothly across the series, the environment of the Ti^{+3} ion becomes distorted in a tetragonal-like fashion for RE = Gd and Y.

The electronic behaviour of the d-electron associated with Ti^{+3} has been investigated. In transport studies, metallic behaviour is observed at high temperatures for RE = La and Ce, accompanied by a transition to semiconducting behaviour at lower temperature. The other $RETiO_3$ show semiconducting behaviour over the temperature range investigated, the activation energies increasing with decreasing RE^{+3} radius. In the magnetic properties, all phases show critical temperatures well above 4.2 K, except for RE = Nd.

An attempt is made to account for the observed properties of the $RETiO_3$ phases in terms of a model proposed by J.B. Goodenough in which the d-electron behaviour depends upon the effectiveness of relevant orbital overlaps.

ACKNOWLEDGEMENTS

I would like to thank my research director, Dr. J.E. Greedan, for his support, patience and understanding during the course of this work, and for the relentless enthusiasm he has shown. I would also like to thank the members of my supervisory committee, Drs. C.V. Stager and D.P. Santry, for their guidance and suggestions.

Many thanks to Dr. H.N. Ng for numerous invaluable discussions leading to an understanding of the crystallographic twinning found for some of these materials.

I would like to acknowledge the outstanding technical assistance of Jim Garrett, Frank Gibbs and Romolo Faggiani, without whom portions of this work could not have been done.

I would like to thank Dr. R. Datars for the use of his equipment in some transport studies, and to Mr. E. Batella for his assistance in performing those experiments. Thanks are due to Dr. T. Timusk for the use of his far-infrared spectrometer, and to Mr. F. Lin and Ms. G. Zaraté for technical assistance. Thanks to Dr. R. Shannon for performing some of the transport experiments, and to Dr. A.P.B. Lever for some magnetic susceptibility data.

Financial support from the National Research Council of Canada in the form of a graduate scholarship and from McMaster University in the form of scholarships and teaching assistantships is gratefully acknowledged.

Finally, I would like to thank my wife, Susan, for her patience and understanding while this manuscript was being prepared.

TABLE OF CONTENTS

TABLE OF CONTENTS (Continued)

LIST OF FIGURES

LIST OF FIGURES (Continued)

LIST OF FIGURES (Continued)

LIST OF FIGURES (Continued)

LIST OF TABLES

Chapter 1

INTRODUCTION

1.1 Scope and Perspective

Transition metal oxides with the perovskite structure have been studied extensively in recent years because of their interesting electronic properties.[1-6] The fascination with these materials arises from the fact that in some cases they provide an opportunity to investigate a transition between the two limiting behaviours of the transition metal d-electrons. In one extreme, the outer d-electrons are localized on atomic sites, and the theory used to describe their behaviour is the ligand field theory. In the other limiting case, the electrons are assumed to be collective and the description is generally a one-electron band theory.

In perovskite oxides, the outer s and p orbitals of oxygen and the transition metal overlap sufficiently that they are usually described by band theory.[3] Electrons in these orbitals are responsible for the binding energy of the crystal. 4f Electrons, on the other hand, are tightly bound to the atomic nuclei and the ligand field theory is always used to describe them. It is the outer d-electrons which are intermediate in character. In some

crystals, they must be treated on the local model while in others on the collective electron model.

1.2 Energy Diagram for the $RETiO_3$ Perovskites

The large electronegativity difference between the transition metal and oxygen in these compounds causes the outer s and p orbitals to form filled valence bands and empty conduction bands that are separated by a large energy gap (10-20 eV).[7] The cation d-orbital energies and the Fermi energy fall within this forbidden energy range.

A schematic one-electron energy diagram for the $RETiO_3$ is shown in Figure 1-1 for localized d-electrons. A similar diagram for collective d-electrons would have some or all of the d-levels broadened into bands. If the d-orbitals do interact to form a band, it is generally narrow compared to that in the transition metals since in the oxides the transition metal ions are further apart and have smaller spatial extension.[6] It is the d-electrons in materials like these that are responsible for many of the observed physical properties.

1.3 Operational Criteria for Distinguishing Localized from Delocalized Electron Behaviour

The physical properties of collective electrons can be quite different from those of localized electrons and often serve as a means of distinguishing between

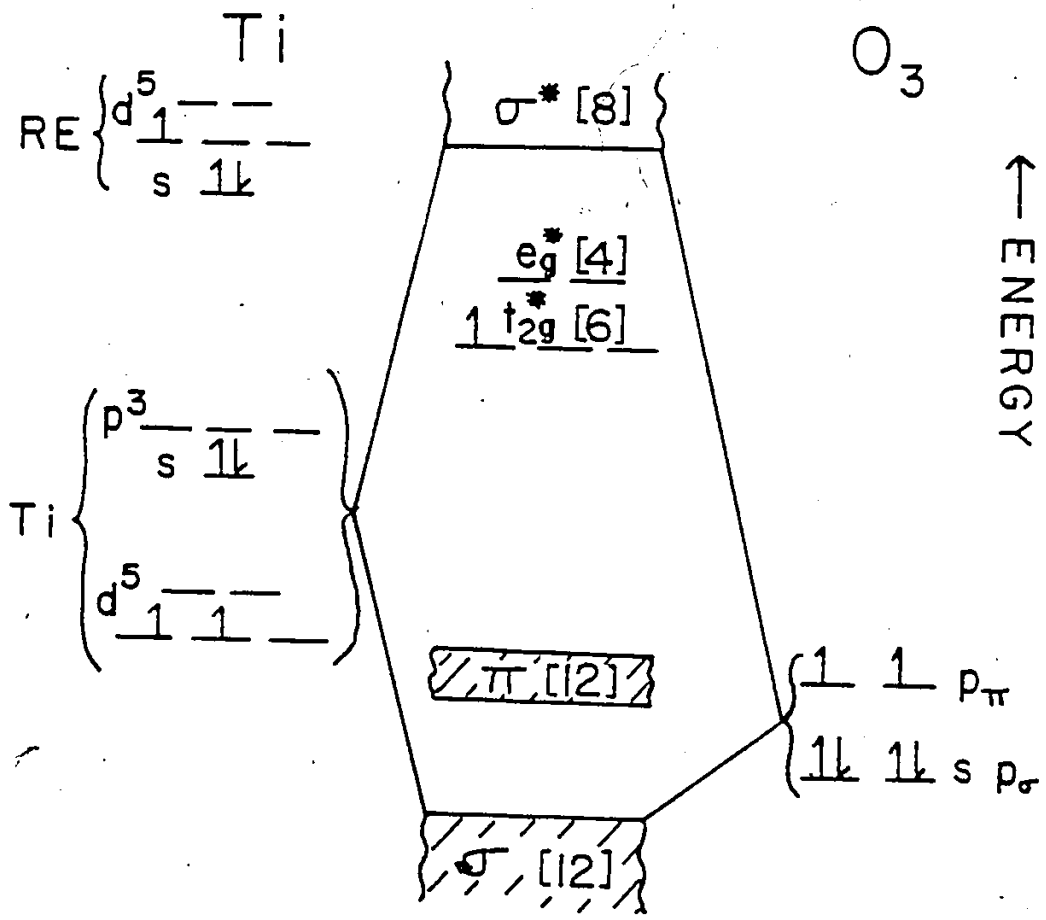

Figure 1-1. A schematic one-electron energy diagram suggested for the $RETiO_3$ by Goodenough.[19] It is drawn here for localized Ti^{+3} d-electrons. Degeneracies of levels and bands (including spin) are shown in brackets. Each of the oxygen orbitals at the right must be multiplied by three.

the two cases. Table 1-1 indicates some physical properties that may differ for localized and collective electrons in solids. Properties that are investigated in this work are magnetic, transport and optical behaviour.

Localized electrons have associated with them localized magnetic moments. These give rise to a molar susceptibility, χ_M, that normally obeys a Curie-Weiss law of the form[9]

$$\chi_M = C_M/(T-\theta) \qquad (1-1)$$

where C is the Curie constant and θ is the Weiss constant. Collective electrons, on the other hand, usually exhibit a weak, temperature independent magnetic susceptibility, referred to as Pauli paramagnetism.[10] Magnetic measurements can quite often easily distinguish between localized and collective electrons in solids.

The transport behaviour in many localized d-electron systems is believed to occur via small polaron conduction.[11,12,13] A small polaron is an electron confined to a single atom and its nearest neighbours by cooperative atomic displacements. There is inherently a strong electron-phonon interaction.

Two possible mechanisms are proposed for conductivity in such systems.[2] In one, the electron carries its local deformation with it and it moves from one site

Table 1-1

Operational Criteria that may Help in Distinguishing Localized from Delocalized Electron Behaviour

Property	Localized	Collective
Definite Fermi Surface Existence	no	yes
Optical Reflectance*		
Atomic Moment	"atomic"[a]	reduced or none
Paramagnetic Susceptibility*		
Superconductivity	no	possible
Polarons	small	large
Conductivity*		

* See discussion in text.

[a] Crystal field may quench orbital moment.

to a neighbouring one by hopping over the energy barrier, E_a, associated with the motion of the deformation. For this case, the mobility is described by diffusion theory and involves an activation energy[14]

$$\mu_{loc} \propto \exp(-E_a/k_BT) \tag{1-2}$$

The alternate mechanism is that the charge carrier may be excited out of its low mobility small polaron state into a higher mobility large polaron state, becoming trapped again in a small polaron state after travelling for a mean free time τ. In this case, the charge carrier mobility is of the same form as for collective electrons

$$\mu_{coll} = e\tau/m^* \tag{1-3}$$

where m^* is the effective mass. However, in this latter case, the number of such higher mobility charge carriers is

$$n \propto \exp(-E_p/k_BT) \tag{1-4}$$

where E_p is the energy difference between the narrow small polaron band and the bottom of the large polaron band. For both mechanisms, the conductivity will contain an activation energy for localized electrons, even if the mobility does not.

For collective electrons in a partially-filled band, the mobility of the charge carriers has the form

given in equation (1-3) while the number of charge carriers remains essentially constant, so that there is no activation energy in the conductivity. Collective electrons in a filled band separated from an empty conduction band by an energy E_g will, however, show an activated conductivity as the number of charge carriers will have the form

$$n \propto \exp(-E_g/k_BT) \qquad (1\text{-}5)$$

One must be cautious, then, in the interpretation of an activated conductivity, as it may arise from either localized electron (small polaron) conductivity or from collective electron semiconducting behaviour. The absence of an activated conductivity, however, strongly suggests collective electron behaviour.

Optical studies also provide a mechanism for distinguishing localized from collective electrons.[2] Localized electrons normally absorb light at distinct frequencies or within narrow frequency ranges. Small polarons (mobile, but localized charge carriers) absorb radiation over a wide frequency range at energies greater than E_a of equation (1-2). Collective electrons when occupying a partially filled band, normally exhibit a reflectivity which undergoes a sharp cut off at the plasma frequency. Collective electrons in a filled band normally show transparency at energies below the band gap (E_g in equation (1-5)) and strong absorption at energies greater than that.

1.4 Goodenough's Model to Account for d-electron Behaviour in Perovskites

Although numerous theories have been proposed to account for the electronic behaviour of d-electrons in oxides,* only one theory has been directly applied to materials like $RETiO_3$. This is a model proposed by John B. Goodenough.[3,19] His model is a qualitative approach which is based upon the principles of chemical bonding. The essential features of this model are presented here.

In Goodenough's approach, the cation-cation (transition metal-transition metal) and cation-anion-cation (transition metal-oxygen-transition metal) interactions are of primary importance in determining the d-electron behaviour. He starts with the localized model for the transition metal ion and examines how the crystal field theory breaks down depending upon the extent of orbital overlap.

The ideal cubic perovskite structure, shown in Figure 1-2(a), is closely related to that of the $RETiO_3$ compounds, and will be referred to in the development of Goodenough's arguments. (The details of the structures of the $RETiO_3$ are presented in Chapter 3.) Note that the

*See, for example, reviews by Adler,[15] Austin and Mott,[16] and Van Zandt and Honig.[17,18]

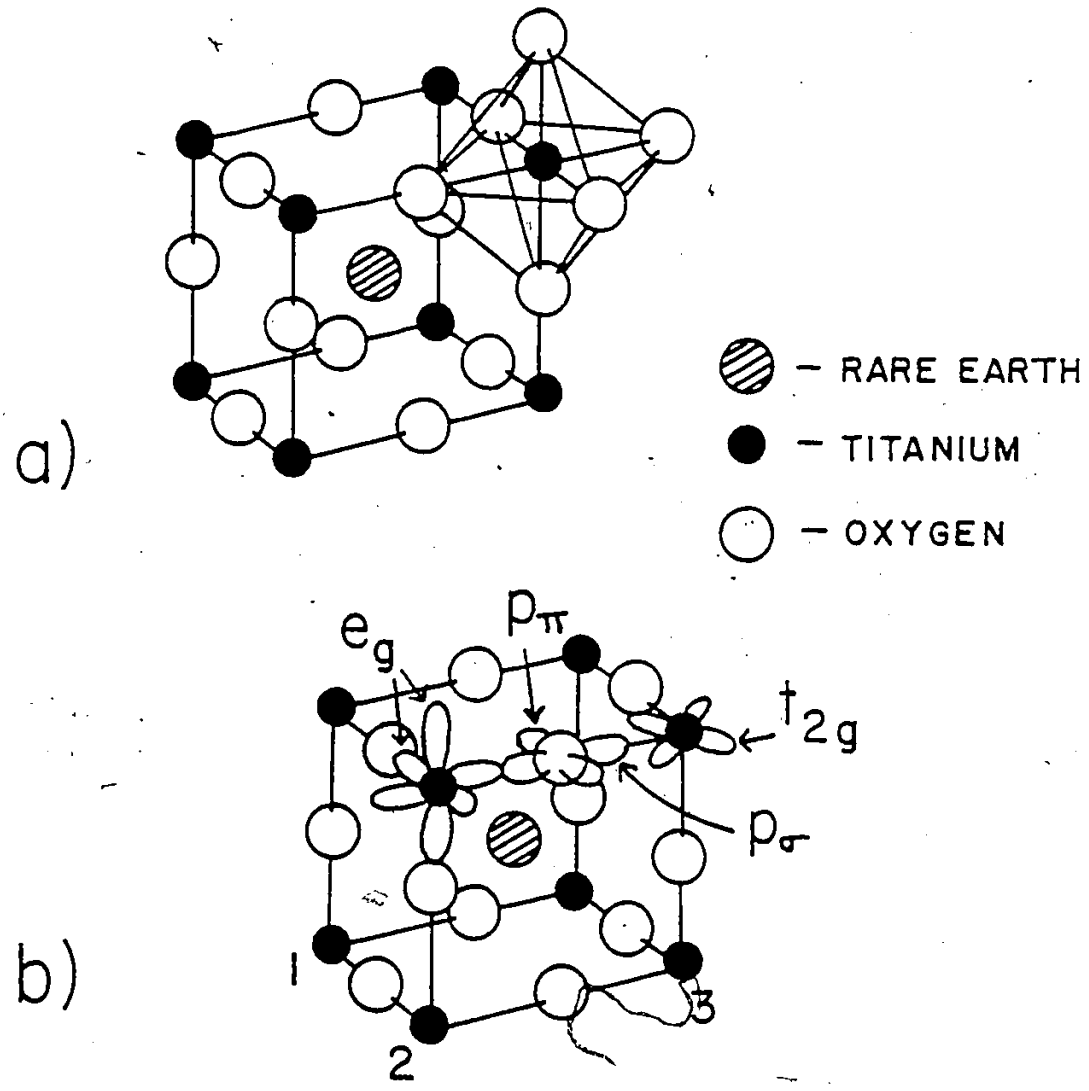

Figure 1-2. (a) The ideal cubic perovskite structure.
(b) The directionality of some relevant orbitals in the perovskite structure. (Shown are the d_{z^2}, $d_{x^2-y^2}$ (e_g symmetry), d_{xy} (t_{2g} symmetry), and a p_π and p_σ orbital on oxygen.)

transition metal is octahedrally coordinated by oxygen atoms and is located at the cube corners, while the rare earth atom is located in the centre of the cube. The rare earth atom donates three valence electrons to the energy bands formed by the transition metal-oxygen subarray, and is assumed to have only a minor effect on the results of the arguments that follow. Our attention will now be focused on the transition metal-oxygen subarray and the orbitals therein.

According to ligand field theory, if the transition metal ion is octahedrally coordinated by anions, the five d orbitals are split into a fourfold degenerate set (including spin degeneracy) of e_g symmetry and a sixfold degenerate set of t_{2g} symmetry. The orbitals of e_g symmetry are directed along the principal axes of the octahedron while those of t_{2g} symmetry are directed between them. Figure 1-2(b) (after reference 5) indicates the orientation of some relevant transition metal and oxygen orbitals.

The e_g orbitals of the transition metal are orthogonal to the oxygen p_π orbitals and can therefore be modified only by covalent mixing with the oxygen s and p_σ orbitals. The orbitals of t_{2g} symmetry are orthogonal to the oxygen s and p_σ orbitals and are modified only by mixing with the oxygen p_π orbitals. The wave functions

for the e_g and t_{2g} orbitals may now be written

$$\Psi_e = N_\sigma(f_e + \lambda_\sigma \psi_\sigma) \qquad (1\text{-}6)$$

$$\Psi_t = N_\pi(f_t + \lambda_\pi \psi_\pi) \qquad (1\text{-}7)$$

where λ_σ and λ_π are the covalent mixing parameters, f_e and f_t are the atomic orbitals of e_g and t_{2g} symmetry, respectively; ψ_σ and ψ_π contain the six near neighbour oxygen orbitals that are mixed through covalence, and N_σ and N_π are the normalization constants.

There are three important overlap integrals that enter the theory now,[5] since whether the d-electrons are localized or collective depends upon the magnitude of the overlap integrals of d-orbitals on neighbouring cations. There are two types of integrals that can occur. There can be cation-cation overlap of t_{2g} orbitals directly across the cube face (i.e., from site 1 to site 3 in Figure 1-2(b))

$$\Delta_{cc} \equiv (\Psi_{t_2}, \Psi_{t_3}) \qquad (1\text{-}8)$$

and there can be cation-anion-cation overlap occurring between transition metal ions that are nearest neighbours on the cube edge (i.e., from site 1 to site 2 in Figure 1-2(b)). There are two cases of cation-anion-cation overlap, one when the e_g orbitals on opposite sides of an anion overlap

$$\Delta^{\sigma}_{cac} \equiv (\Psi_{e_1}, \Psi_{e_2}) = N_{\sigma}^2 \lambda_{\sigma}^2 \qquad (1\text{-}9)$$

and one when the t_{2g} orbitals on opposite sides of an anion overlap

$$\Delta^{\pi}_{cac} \equiv (\Psi_{t_1}, \Psi_{t_2}) = N_{\pi}^2[\lambda_{\pi}^2 + 2\lambda_{\pi} \times (f_t, \psi_{\pi})] \qquad (1\text{-}10)$$

Of the cation-anion-cation overlap integrals, always $\Delta^{\pi}_{cac} < \Delta^{\sigma}_{cac}$. However, the important overlap integral for the $RETiO_3$ is Δ^{π}_{cac} since the Ti^{+3} d-electron is associated with orbitals of t_{2g} symmetry.

Goodenough now defines a theoretical criterion for localized versus collective electrons. Since it is known that when the overlap integrals are large enough, it is necessary to use a collective electron description, and that when they are small, the localized electron theory applies, he introduces the idea of a critical overlap integral, Δ_c. Localized electron theory applies when $\Delta < \Delta_c$ and collective electron theory is used when $\Delta > \Delta_c$.

In the cubic perovskite structure, the separation of two cations across a cube face is ~ 5.5 Å. Goodenough has been able to estimate empirically the separation at which significant cation-cation overlap occurs. This distance is estimated to be 3.0 Å for Ti^{+3}.[4] Thus, the cation-cation interactions across a cube face can be assumed small (i.e., Δ_{cc} will have little effect on d-electron behaviour). Materials with the perovskite structure, then, provide an opportunity to study the character of the overlap integrals, Δ_{cac}. It should be emphasized

that cation-anion-cation overlaps will have a great influence on deciding whether the t_{2g} and e_g levels remain localized or become broadened into bands. If $\Delta^{\pi}_{cac} < \Delta^{\sigma}_{cac} < \Delta_c$, all the levels will be localized. If $\Delta^{\pi}_{cac} < \Delta_c < \Delta^{\sigma}_{cac}$, the t_{2g} levels will remain localized but the e_g levels will be broadened into a band. Finally, if $\Delta_c < \Delta^{\pi}_{cac} < \Delta^{\sigma}_{cac}$, both t_{2g} levels and e_g levels will be broadened into bands.

Goodenough casts this argument into an equivalent form which emphasizes the breakdown of the ligand field theory as orbital overlap increases. The orbitals Ψ_e and Ψ_t (equations (1-6) and (1-7)) satisfy the Hamiltonian of a localized electron model for the transition metal ion which is

$$H = H_o + V_{el} + V_{cf} + V_{LS} + V_{\lambda} + H_{ex} \qquad (1\text{-}11)$$

H_o is the free ion energy operator giving hydrogen-like zero-order wave functions. When there is more than one d-electron per cation, the Coulomb energy of H_o must be corrected by the intra-atomic exchange correlations, V_{el}. The perturbation $V_{cf} = V_o + V_c + V_t$ arises because the cation is in a crystal field. V_o shifts the zero of energy, V_c is the cubic component of the crystal field that splits the energies of the e_g and t_{2g} orbitals, and V_t is any non-cubic component of the crystal field that may further remove orbital degeneracies. V_{LS} arises from the spin-

orbit interaction that occurs within the ion, and the two remaining terms, V_λ and H_{ex}, arise from inter-ion interactions. V_λ is the elastic coupling energy associated with cooperative local distortions, and H_{ex} is the superexchange coupling between any spontaneous moments on neighbouring cations. H_{ex} has the form

$$H_{ex} = -2\sum_{ij} J_{ij} S_i \cdot S_j \qquad (1\text{-}12)$$

where

$$J_{ij} = b_{ij}^2/U \qquad (1\text{-}13)$$

b_{ij} is the one electron transfer integral and U is the electrostatic energy required to add an electron to an orbital that is already half-full.

In the ligand field approach, the H_{ex} term is small and is treated as a perturbation. The transfer integrals, b_{ij} (hereafter referred to as b), that enter into H_{ex} are proportional to the square of the overlap integral.[5] Corresponding to the overlap integrals, Δ_{cac}^{σ}, Δ_{cac}^{π} and Δ_c are b_σ, b_π and b_c. For the case when $b_\pi < b_\sigma < b_c$, the H_{ex} term is small, can be treated as a perturbation in equation (1-11), and the d-electrons are adequately described by the ligand field theory. However, when b_c is approximately equal to b_π and b_σ, the effect of the term H_{ex} is no longer small, and it cannot be treated as a perturbation in equation (1-11). The ligand field theory breaks down as bands form and the

d-electrons become collective.

Goodenough has gone on to construct phenomenological phase diagrams relating b to electrical and magnetic properties of oxide systems. The phase diagram considered appropriate for the $RETiO_3$ is shown in Figure 1-3. In the construction, the effect of the presence of the rare earth ion and any spontaneous moment it may have, have been ignored. When $b < b_c$, the system is in the localized electron regime and superexchange interactions are important. For $b_c < b < b_m$, the electrons are in strongly correlated narrow bands, while for $b > b_m$, they are in wider bands.

When the work being presented in this thesis was begun, it appeared as though the $RETiO_3$ series, RE = La, ..., Y, may be one in which the d-electrons were collective for RE = La and localized for RE = Y. The structures (discussed more fully in Chapter 3) are a distortion of the ideal perovskite structure shown in Figure 1-2(a), and the distortion was believed to increase in the series in going from $LaTiO_3$ to $YTiO_3$. It seemed possible that within the $RETiO_3$ series, the value of b, the transfer integral, was scanning the phase diagram shown in Figure 1-3, causing the d-electron to be localized in some $RETiO_3$, delocalized in others. To investigate whether this is the case, it was decided to prepare and carefully characterize the $RETiO_3$ phases, RE = La, Ce, Pr, Nd, Gd, Y,

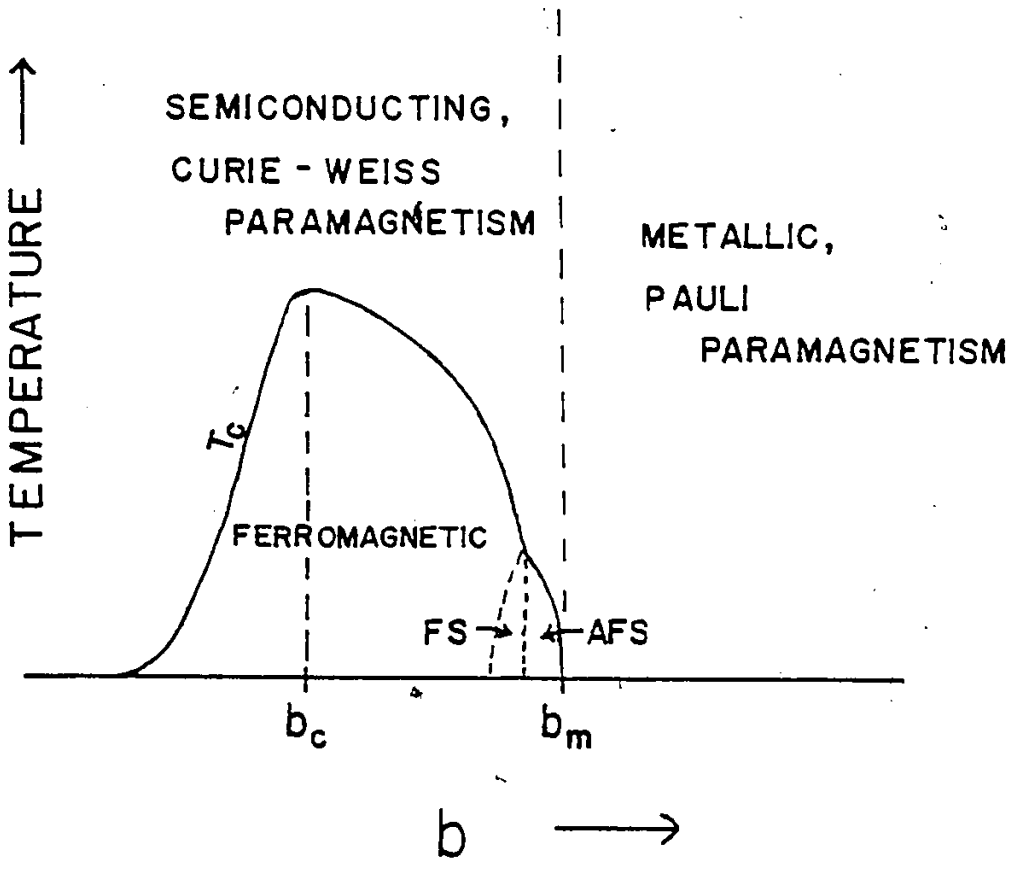

Figure 1-3. Schematic phase diagram relating the transfer integral, b, to the magnetic and transport properties for the $RETiO_3$ (after reference 20).
FS = ferromagnetic spiral
AFS = antiferromagnetic spiral

and the solid solution series $La_xY_{1-x}TiO_3$. The details of the preparative techniques and chemical analyses are given in Chapter 2. To ensure that these materials form an isostructural series and to determine whether the structures indicate that orbital overlap, and hence b, is changing across the series, the crystal structures of selected members of this series were solved and are reported in Chapter 3. Magnetic, transport and optical studies of the $RETiO_3$ were undertaken to establish for which $RETiO_3$ the Ti^{+3} d-electron is best described as localized, and for which it is best described as collective. The experimental details are reported in Chapter 4 and the results and some discussion in Chapter 5. In Chapter 6, the behaviour of the d-electron in this series is interpreted in terms of Goodenough's approach which has been given in this chapter. The appropriateness of applying Goodenough's ideas to the $RETiO_3$ is considered, and suggestions for further investigations are made.

Chapter 2

SAMPLE PREPARATION AND ANALYSIS

2.1 Introduction

Although $RETiO_3$ phases have been prepared by several groups over the past 25 years,[20-26] the remarkable differences in physical properties, unit cell parameters and even in symmetry classification reported for, presumably, the same material indicate that there are certain difficulties in sample preparation and characterization.

One known problem is that two of these materials (RE = La,Ce) exist at all compositions $RE_{(2/3)+x}TiO_3$, where $0 < x < 1/3$.[27,28] As x decreases from 1/3 in this formula, charge compensation requires that Ti^{+3} be converted to Ti^{+4}, so that many properties, including lattice parameter, may be affected by a rare earth deficiency.

Figure 2-1 shows the variation of the pseudo-cubic lattice parameter, a_o, over the range $x = 0$ to $x = 1/3$ for $La_{(2/3)+x}TiO_3$ and $Ce_{(2/3)+x}TiO_3$. It is clear that great care must be taken to ensure that the RE:Ti ratio in a $RETiO_3$ preparation is, in fact, 1:1.

Another problem in the preparation of these materials is control of the oxygen fugacity. At the

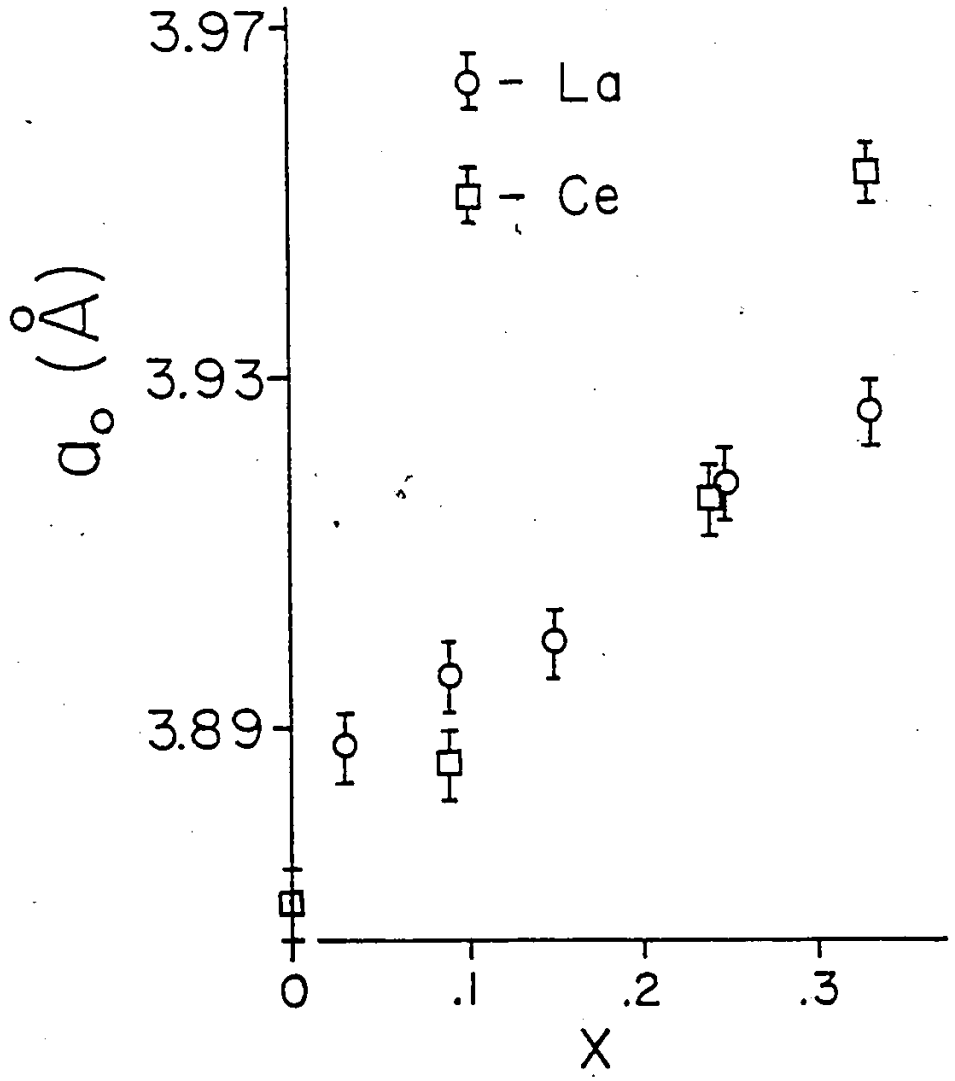

Figure 2-1. Variation of the pseudo-cubic lattice parameter, a_o, over the range x = 0 to x = 1/3 for $La_{(2/3)+x}TiO_3$ and $Ce_{(2/3)+x}TiO_3$.

elevated temperatures required for their synthesis, the $RETiO_3$ phases will oxidize rapidly in the presence of air to the well-known rare earth pyrochlores, $RE_2Ti_2O_7$.[29] During the synthesis, precautions must be taken to ensure that no source of oxygen, other than that in the starting materials, is present. The unit cell parameter varies dramatically as a function of oxygen nonstoichiometry. In the case of $LaTiO_{3+x}$, the pseudo-cubic lattice parameter decreases from 3.963 Å for x = 0.029 to 3.940 Å for x = 0.20.[27]

Analysis of these materials is further complicated by the fact that they are very difficult to dissolve. Treatment with hot aqua regia, HF/H_2SO_4 at elevated pressure, and bisulfite fusions have proved unsuccessful. This makes wet chemical analysis for the RE and Ti impossible.

For those materials for which neutron activation analysis is feasible, RE:Ti ratios have been determined. For all $RETiO_3$ phases, oxygen content has been determined by gravimetric oxidation in air at 1000°C to the $RE_2Ti_2O_7$ pyrochlores. An additional check for excess RE or Ti in the $RETiO_3$ phase is the presence of any reflections other than those of $RE_2Ti_2O_7$ in the oxidized product, as excess RE would produce diffraction peaks from RE_2O_3 or excess Ti would produce TiO_2 reflections.

No attempt has been made in previous preparations of the $RETiO_3$ phases to produce single crystal samples. Presumably the reason for this is the difficulty involved in attaining and controlling the temperatures required to grow a crystal from the melt ($\sim$ 2000°C). This work represents the first preparation of crystals of many of the $RETiO_3$ phases studied here. Also, in many of the previously reported preparations, little or no chemical analysis has been performed on the products. The variability in stoichiometries that can exist in these materials necessitates good analysis.

The preparation techniques and the results of chemical analyses performed on the products will now be described for the $RETiO_3$ phases RE = La, Ce, Pr, Nd, Sm, Gd, Y, and the solid solutions La_xY_{1-x}.

2.2 Sample Preparations

The basic reaction used to prepare all phases (except $CeTiO_3$) was

$$RE_2O_3 + Ti_2O_3 \rightarrow 2RETiO_3 \qquad (2\text{-}1)$$

Ti_2O_3 was prepared by arc melting pellets of Ti sponge (99.99%, Hruden Scientific) and TiO_2 (99.95%, Atomergic Chemetals) in the appropriate proportions on a water-cooled copper hearth under 400 torr of prepurified argon. A sample of the product ($\sim$ 0.5 g) was checked for oxygen

stoichiometry by thermal gravimetric oxidation to TiO_2, and the bulk was adjusted to stoichiometry by the addition of Ti or TiO_2 and arc melting again. This procedure was repeated until the product was prepared within the limits $Ti_2O_{3.000\pm0.005}$. Emission spectrographic analysis of a sample of Ti_2O_3 prepared in this way revealed no impurities at a concentration greater than 100 ppm.

$CeTiO_3$ was prepared by the reaction

$$CeO_2 + TiO \rightarrow CeTiO_3 \qquad (2\text{-}2)$$

TiO was prepared from Ti and TiO_2 by the same technique as Ti_2O_3.

Rare earth oxides used in the preparations (Research Chemicals, 99.95% or better) were prefired in air at 1000°C before use to remove hydroxides or carbonates, except for Pr_6O_{11}, which was heated in hydrogen gas at 900°C for eight hours to produce Pr_2O_3.

Carefully weighed proportions of the rare earth oxide and titanium oxide were intimately mixed in acetone using a mortar and pestal. (For the preparations of $La_xY_{1-x}TiO_3$, appropriate quantities of La_2O_3, Y_2O_3 and Ti_2O_3 were weighed and mixed.) When the acetone evaporated, the mixture was pressed into pellets before reaction. If the preparation was to be performed in a closed molybdenum crucible, the pellets were sealed in the crucible under 400 torr of prepurified argon gas.

$RETiO_3$ phases have been successfully prepared in our laboratory by a variety of techniques, some of which have resulted in the production of single crystals. Figure 2-2 shows some of the best crystals that have been obtained, ranging in size from 30 mg ($YTiO_3$) to 180 mg ($PrTiO_3$).

Polycrystalline samples have been prepared by melting the reactants in open molybdenum crucibles under 1.7 atmospheres of prepurified argon or in closed molybdenum crucibles under vacuum ($\sim 10^{-5}$ torr) followed by rapid cooling (> 100°/hr).

Single crystals have been obtained using the Stockbarger technique[30,31] in open or closed molybdenum crucibles, or by the Czochralski technique.[31,32]

Closed crucible Stockbarger growths were effected under 1.7 atmospheres of prepurified argon gas using the experimental setup shown in Figure 2-3. Radiofrequency heating power was increased until the tungsten rod was seen to drop as the expendable pellet of $RETiO_3$ melted. This was taken to mean that the contents of the closed crucible were molten. The power was increased slightly from this level to ensure melting and then decreased at the desired rate in an attempt to produce crystals.

Open crucible Stockbarger growths were performed under 1.7 atmospheres of prepurified argon using an apparatus similar to that in Figure 2-3. However, no

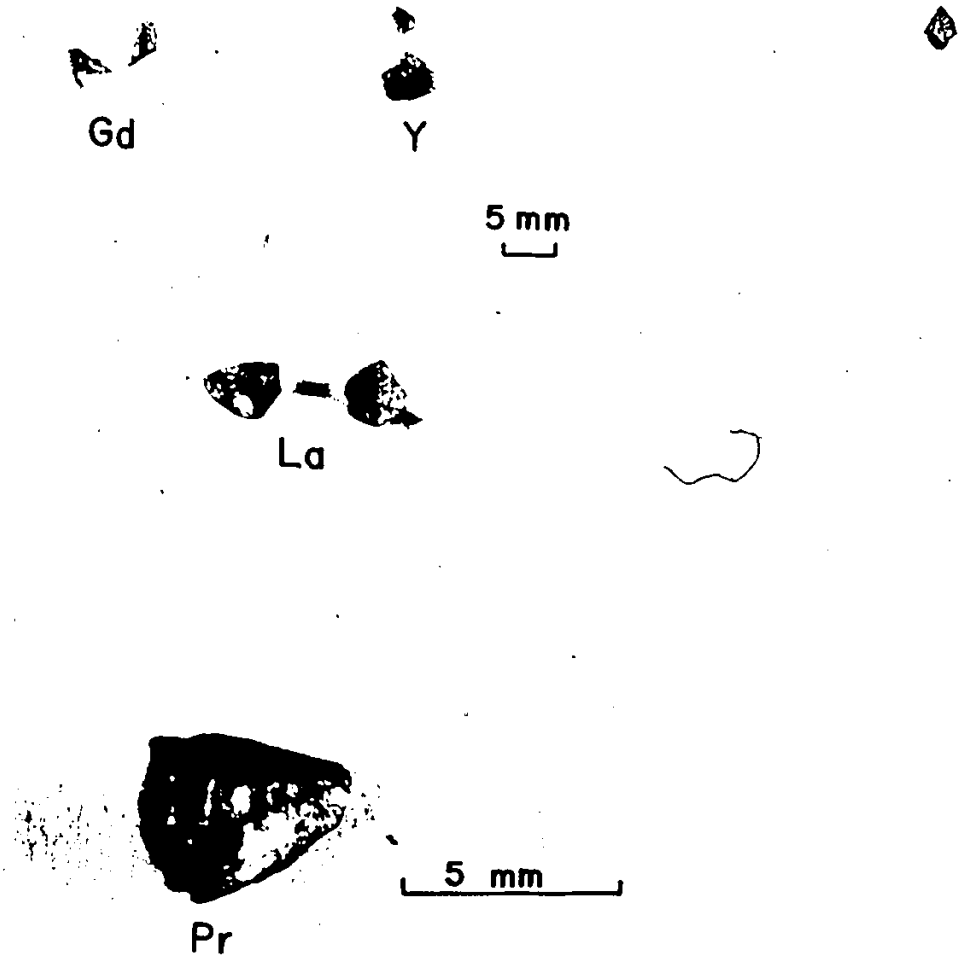

Figure 2-2. Photographs of some $RETiO_3$ crystals.

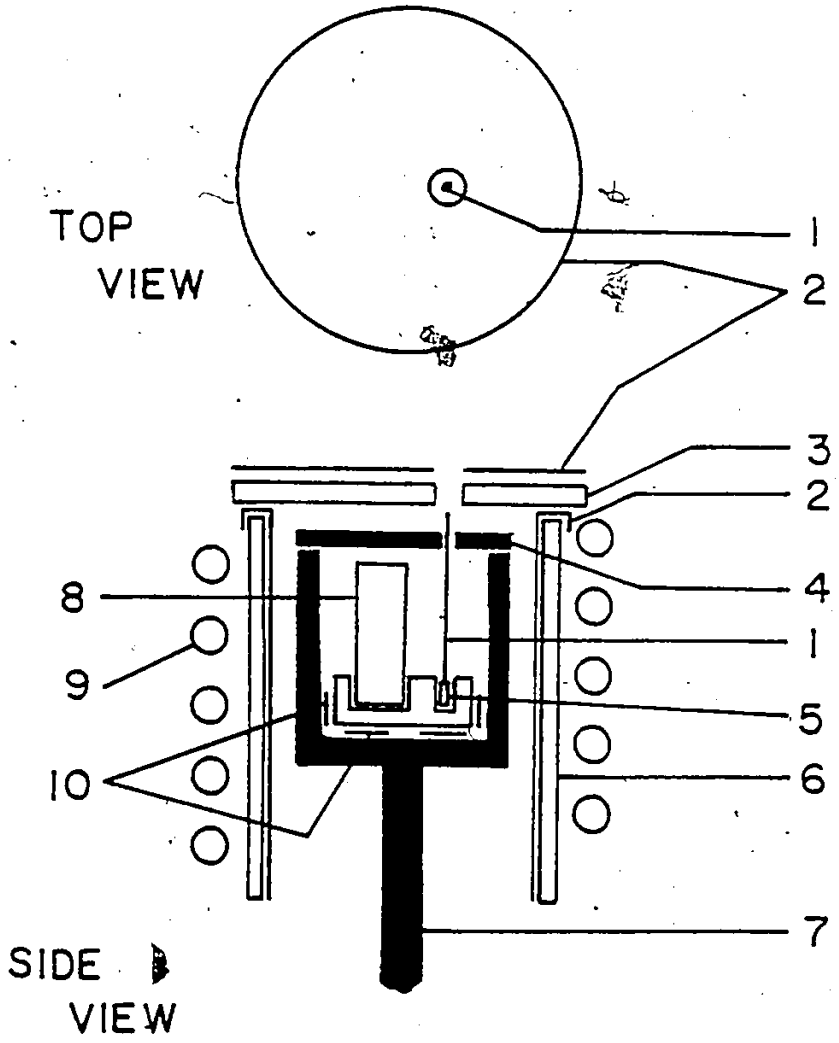

Figure 2-3. Experimental setup used for closed crucible Stockbarger preparations. Items indicated in the figure are 1) tungsten rod; 2) molybdenum foil; 3) Zircar insulation; 4) susceptor cover (graphite); 5) expendable pellet of material being prepared; 6) Mullite tube; 7) graphite susceptor; 8) sealed molybdenum tube containing pellets of material being prepared; 9) water-cooled copper work coil; 10) tungsten rod used as a stand-off.

second pellet and tungsten rod were used to determine the melting temperature, rather a hole was present in the susceptor cover allowing direct observation of the reactants.

$YTiO_3$ crystals were grown by the Czochralski technique from a one-inch molybdenum crucible using radio-frequency heating. All other Czochralski growths were performed in a modified Centorr tri-arc crystal growing apparatus.[33] A tungsten seed rod with good thermal contact to a heat pipe was used to pull the crystal. The graphite hearth was modified with a molybdenum insert. A shallow cone was machined onto the surface of the molybdenum to better support the molten charge.

Table 2-1 summarizes the details of the individual preparations. When samples from more than one preparation were used in different experiments, details for each are included.

2.3 Sample Analysis

The first analysis performed on every preparation was an X-ray diffraction powder pattern. This would immediately indicate the presence of any oxidized product such as the pyrochlore phase. The powder pattern for $GdTiO_3$, typical of the $RETiO_3$, is described in Table 2-2.

Thermal gravimetric analysis was performed on all samples to check the oxygen stoichiometry. Results of

TABLE 2-1. $RETiO_3$ Preparation Details

RE in $RETiO_3$	Preparation Technique	Growth Details	Crystal Size (mg)
La	Stockbarger	open ½" Moly. crucible, 8 gram charge, cooled at 50°/hr for 12 hours.	90
Ce	Czockralski	4 gram charge, pulled at 4 mm/hr for 3 hours	20
Pr	Czockralski	4 gram charge, pulled at 4 mm/hr for 3 hours	180
Nd I	Stockbarger	open ½" Moly. crucible, 5 gram charge, cooled at > 100°/hr, (used for magnetic studies)	
Nd II	Stockbarger	closed ½" Moly. crucible, 5 gram charge, cooled for 12 hr. at 6°/hr (used for crystallographic transport and optical work)	20
Sm	Stockbarger	open ½" Moly. crucible, 5 gram charge, cooled at 50°/hr for 12 hr.	
Gd	Stockbarger	open ½" Moly. crucible, 5 gram charge, cooled at 50°/hr for 12 hr.	35
Y*	Czochralski	1" Moly. crucible, 20 gram charge, pulled at 2.5 mm/hr.	30
La_xY_{1-x}	Stockbarger	open ½" Moly. crucibles, 3 gram charges, cooled at > 100°/hr.	

* Sample prepared by J.D. Garrett.

TABLE 2-2

Powder Pattern for $GdTiO_3$ (with CuK_α radiation to $2\theta = 70°$)

h k l	100 I/I_1	$d_{obs.}$	$d_{calc.}$
1 1 0	25	3.911	3.915
0 0 2	20	3.831	3.832
1 1 1	30	3.482	3.486
0 2 0	25	2.848	2.846
1 1 2	100	2.736	2.738
2 0 0	40	2.696	2.697
0 2 1	25	2.669	2.668
2 1 1	10	2.316	2.322
1 0 3			2.309
0 2 2	10	2.288	2.285
2 0 2	15	2.203	2.205
1 1 3	10	2.136	2.139
2 2 0	25	1.956	1.957
0 0 4	40	1.917	1.916
2 2 1	40	1.895	1.896
3 0 1	25	1.742	1.750
2 2 2			1.743
1 3 1			1.743
1 1 4	5	1.722	1.721
3 1 1	5	1.673	1.673
1 3 2	10	1.618	1.621
0 2 4	5	1.591	1.589
3 1 2	35	1.563	1.565
2 0 4			1.562
3 0 3	10	1.466	1.470
1 3 3			1.466
2 2 4	10	1.369	1.369

these analyses are given in Table 2-3. The mechanism of nonstoichiometry has not been determined. Many perovskites, however, do exhibit nonstoichiometry on one or more sublattices.[19,34]

Among the possible mechanisms for nonstoichiometry of the type ABO_{3+x}, as is observed for the $RETiO_3$, are the following. a) Interstitial oxygen may be present in the lattice. This behaviour is not common in perovskite structure oxides, but is found, for example, in fluorite structure oxides such as UO_{2+x}.[35] b) Vacancies may exist on both the A and B cation sites, leaving a perfect oxygen sublattice. c) The nonstoichiometry may result from A site vacancy only. A cation deficiency has been widely investigated. The case of ReO_3, for example, may be viewed as a perovskite structure with all of the A sites vacant. It is because of the stability of the corner-shared BO_6 octahedra that it is possible in this case to remove all of the A cations without collapsing the sub-array. As previously mentioned, nonstoichiometry of the A cation vacancy type is known to exist over the entire range $0 < x < 1/3$ for $La_{2/3+x}TiO_3$ and $Ce_{2/3+x}TiO_3$, the vacancy being compensated by oxidation of Ti^{+3} to Ti^{+4} on the B site.

As is apparent from the analysis reported in Table 2-3 for the $RETiO_3$, the extent of the nonstoi-

Table 2-3

Stoichiometry Analysis

RE in $RETiO_3$	Theoretical Weight Gain (mg.)	Observed Weight Gain (mg.)	Y in $RETiO_y$ (± .005)	RE:Ti ratio (± 2%)
La	.727	.710	3.011	
Ce	1.022	.994	3.013	
Pr	1.336	1.303	3.012	
Nd	.822	.809	3.008	.98
Sm	.714	.689	3.011	.98
Gd	.747	.734	3.009	
Y	1.104	1.085	3.009	
La_xY_{1-x}				(La:Ti)
x = .05	.827	.791	3.021	.049
.10	.955	.915	3.020	.11
.20	.883	.844	3.021	.19
.25	.811	.771	3.024	.24
.30	.791	.751	3.025	.29
.40	.806	.776	3.018	.38
.50	.719	.698	3.014	.47
.60	.738	.705	3.021	.57
.70	.774	.743	3.019	.65

chiometry is small. It may be due to one or a combination of the discussed mechanisms. The small extent to which it exists would make it extremely difficult to determine exactly how it occurs.

RE:Ti ratios determined by neutron activation analysis where possible are also reported in Table 2-3. X-ray diffraction patterns of the oxidized titanite phases showed no diffraction peaks other than those of the pyrochlore, also indicating that the products were neither rare earth nor titanium deficient to within the limits of detection of the X-ray technique (2-5%). Emission spectrographic analysis on several $RETiO_3$ preparations showed no evidence for impurities at levels greater than 100 ppm.

Laue photographs of different areas of larger crystals used for optical and transport studies revealed no change of crystal orientation throughout the sample. Precession photographs on smaller crystals used to determine structures indicated the presence of twinning in $SmTiO_3$, $NdTiO_3$ and $LaTiO_3$. The nature and extent of this twinning is discussed further in Chapter 3. The approximately equal volumes of the twin components in all samples of the same material examined suggest that multiple twinning occurs. Thus, all samples used for crystallographic, optical and transport studies were single crystals or single crystals containing a small volume of twinned component.

In order to determine conclusively whether or not the $La_xY_{1-x}TiO_3$ series constitutes a series of solid solutions, a detailed study of lattice parameters was done. The results of this study are presented in Figure 2-4. The smooth variation of lattice parameters and cell volume across the series indicates that the $La_xY_{1-x}TiO_3$ system does, in fact, form solid solutions.

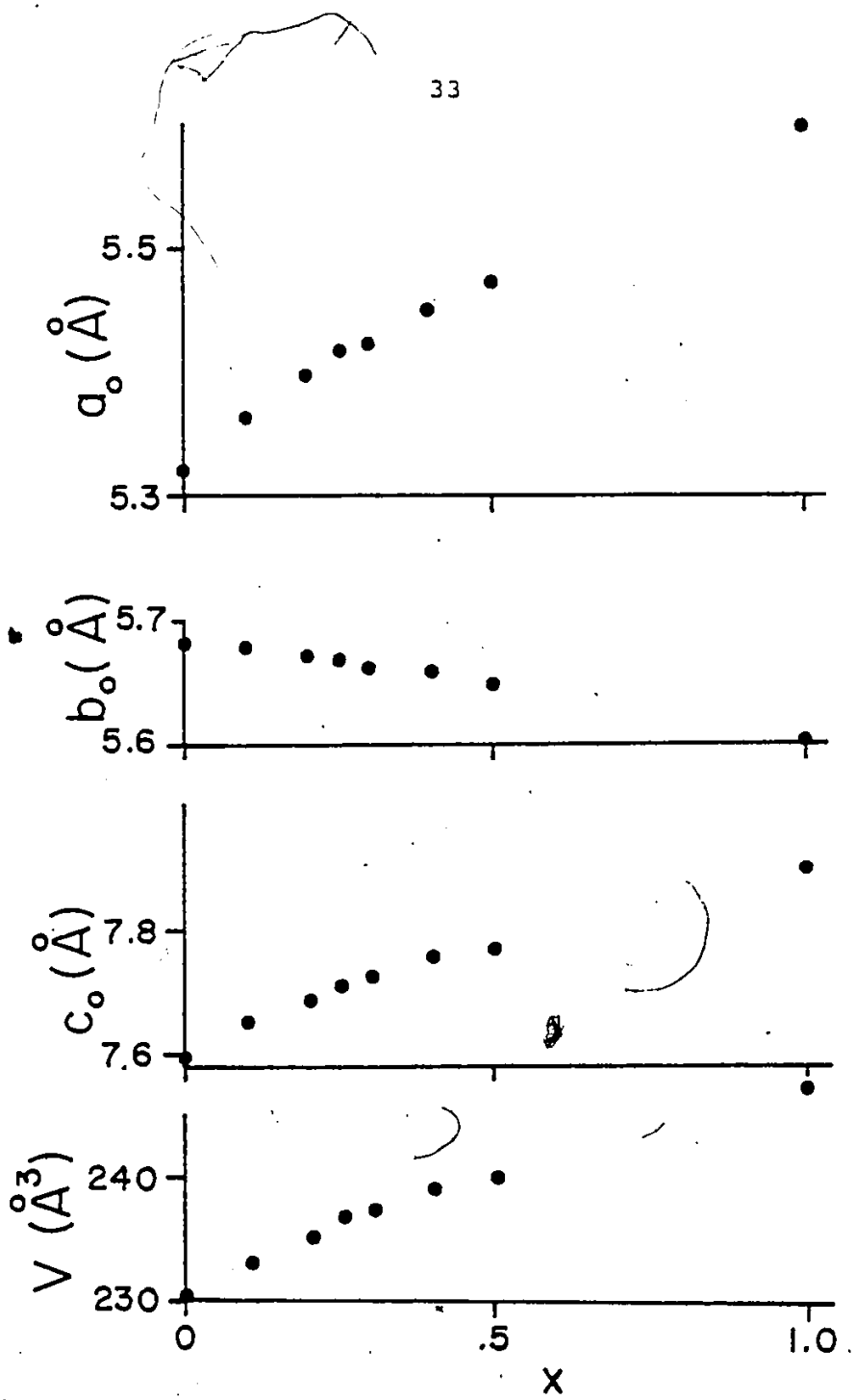

Figure 2-4. Variation of unit cell parameters and cell volume across the series $La_xY_{1-x}TiO_3$. Data for x = 0 and x = 1 were obtained from single crystal samples, the other data from polycrystalline samples. The error associated with a data point is approximated by its size.

Chapter 3

CRYSTALLOGRAPHIC STUDIES

3.1 Introduction

Of all the ABO_3 phases, compounds of the perovskite family are probably the most commonly encountered. The ideal perovskite structure is shown in Figure 1-2(a), and is typified by $SrTiO_3$, with $a_o = 3.905$ Å, Z = 1 and space group O_h^1 - Pm3m.[36] Sr is in position 1b (1/2, 1/2,1/2), Ti is at the origin, position 1a (0,0,0) and the oxygen atoms are in position 3d (1/2,0,0). This results in a network of corner-shared TiO_6 octahedra extending in three dimensions. In the ideal structure, the TiO_6 octahedra are perfect with six equal Ti-O bonds and each Sr atom is surrounded by twelve equidistant oxygen atoms.

It is interesting to note that $CaTiO_3$, the mineral perovskite itself, is not cubic, but orthorhombic (space group D_{2h}^{16} - Pbnm) with Z = 4.[37] Deviations from the ideal cubic structure occur often, and details have only recently been determined as single crystals became available. Even in distorted perovskites there is often a strong pseudocubic character. This makes it difficult to determine the true symmetry and unit cell especially when only

powder data are available.

This work demonstrates that the five $RETiO_3$ phases studied here have the distorted perovskite structure, commonly referred to as the $GdFeO_3$ structure, shown in Figure 3-1. $GdFeO_3$ is orthorhombic, Z = 4 and space group D_{2h}^{16} - Pbnm, as in $CaTiO_3$.[38,39] The relationship between the orthorhombic cell constants and that of the cubic perovskite pseudocell a' is

$$a_o \approx b_o \approx \sqrt{2}\, a', \quad c_o = 2a'$$

As in the ideal perovskite structure, the $GdFeO_3$ structure is made up of an array of corner shared FeO_6 octahedra extending in three dimensions. However, the FeO_6 octahedra undergo a cooperative buckling and are tilted, as can be seen in Figure 3-1. In $GdFeO_3$, the distortion of the FeO_6 octahedron is small, however the GdO_{12} polyhedron is severely distorted, and is more commonly considered to be a GdO_8 polyhedron.

The $RETiO_3$ phases provide an example of the difficulty of determining the true symmetry and unit cell in distorted perovskite systems when only powder samples are available. Table 3-1 gives an historical account of the crystal chemistry of polycrystalline $RETiO_3$, RE = La, Nd, Sm, Gd and Y. Confusion has persisted regarding even the true crystal system of those compounds for which

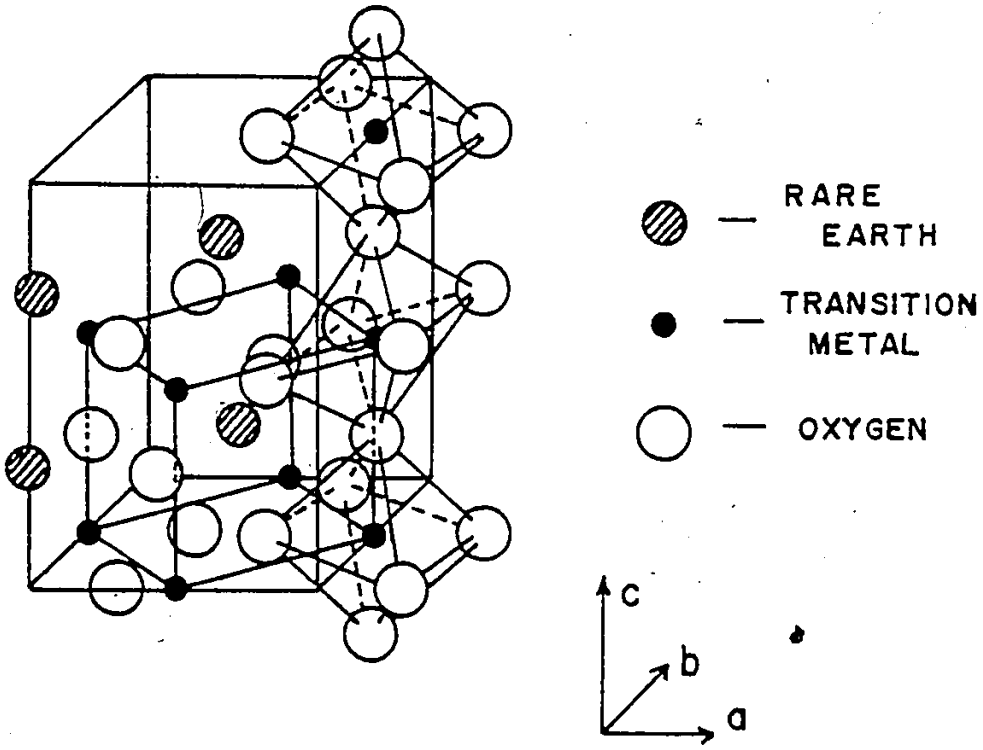

Figure 3-1. The $GdFeO_3$ structure type. A pseudo-cubic perovskite cell is outlined in the lower half of this cell. See Figure 1-2(a) for comparison.

TABLE 3-1

Crystal Data for $RETiO_3$ - A History
RE = La, Nd, Sm, Gd, Y

RE	Symmetry	Cell Constants (A°)	Year	Reference
La	Cubic	a = 3.92	1954	21
	Pseudocubic	a ≈ 3.89	1956	40
	Orthorhombic	a = b = 5.596 c = 7.914	1961	22
	Orthorhombic	a = 5.54 b = 5.75 c = 7.83	1966	23
	Cubic	a = 3.92	1976	20
Nd	Pseudocubic	a = 3.90	1956	40
	Orthorhombic	a = 5.48 b = 5.70 c = 7.76	1966	23
	Cubic	a = 3.87	1976	20
Sm	Pseudocubic	a ≈ 3.88	1956	40
	Orthorhombic	a = 5.398 b = 5.568 c = 7.651	1969	24
	Cubic	a = 3.86	1976	20
Gd	Orthorhombic	a = 5.44 b = 5.56 c = 7.43	1966	23
	Orthorhombic	a = 5.353 b = 5.655 c = 7.616	1969	24
Y	Orthorhombic	a = 5.340 b = 5.665 c = 7.624	1969	24
	Orthorhombic	a = 5.327 b = 5.618 c = 7.591	1973	41

RE = La to Sm, for which various authors, working with powder data, have reported cubic, pseudocubic or orthorhombic cells. Also, there is generally poor agreement between cell constants reported by different authors presumably for the same materials.

The structures of selected members of the $RETiO_3$ series (RE = La, Nd, Sm, Gd, Y) were determined from automated diffractometer data using crystals obtained by the techniques described in the previous chapter. Single crystals were obtained only for the materials $GdTiO_3$ and $YTiO_3$. For RE = La, Nd and Sm, the crystals obtained were twinned, but were successfully used in the structural refinement. It is probable that the existence of twinning in these phases is due to their highly pseudocubic nature.

3.2 Crystal Data

Precession photographs of untwinned crystals in the $RETiO_3$ series showed that the conditions of systematic absences were $h + l \neq 2n$ for h0l, $k \neq 2n$ for 0kl, $h \neq 2n$ for h00, $k \neq 2n$ for 0k0 and $l \neq 2n$ for 00l. The centric orthorhombic space group D_{2h}^{16} - Pbnm was chosen for initial refinement over the acentric $Pbn2_1$ both from a consideration of the statistical distribution of intensities obtained for $GdTiO_3$, and from the expectation that the $RETiO_3$ would be isostructural with the $REFeO_3$, which are known to be best described in Pbnm.[38] There are four formula

units per cell. The four rare earth atoms are in the special position 4(c) (x,y,1/4); the four iron atoms are in the special positions 4(b) (0,1/2,0); four of the twelve oxygen atoms are in the special position 4(c) (x,y,1/4); and, eight are in general positions. Accurate unit cell parameters, reported in Table 3-2, were obtained by a least squares refinement of 2θ values ($20° < 2\theta < 35°$) of 15 reflections carefully measured on the diffractometer.

3.3 Intensity Measurements

For collection of intensity data, all crystals were ground to spherical shape. Data were collected on two Syntex automatic diffractometers, Models $P\bar{1}$ and $P2_1$ in the θ/2θ scan mode using graphite monochromatized MoK_α radiation ($\lambda = 0.71069$ Å) and a scintillation detector. Reflections were scanned at variable rates from 4.0 to 24.0°/min. in 2θ to minimize counting errors for the weak reflections. Reflections for each crystal were collected within a sphere defined by 2θ given in Table 3-3. Reflections whose intensity, corrected for background, were less than three times the standard deviation were considered unobserved. Equivalent reflections (after any correction or omission for twinning, if necessary) were averaged, and the data were corrected for Lorentz and polarization effects. Absorption corrections were also applied in each case assuming spherical shape (radii and linear

TABLE 3-2

$RETiO_3$ Crystal Data[a]

	La	Nd	Sm	Gd	Y
a (Å)	5.601(2)	5.495(3)	5.454(2)	5.393(2)	5.316(2)
b (Å)	5.590(2)	5.589(3)	5.660(2)	5.691(2)	5.679(2)
c (Å)	7.906(4)	7.779(4)	7.722(4)	7.664(3)	7.611(3)
V ($Å^3$)	247.5(2)	238.9(2)	238.4(2)	235.2(2)	229.8(2)
μ^* (cm^{-1})	203.5	246.6	279.6	320.5	292.3
ρ_{calcd} (g/cm^3)	6.30	6.68	6.86	7.15	5.34
ρ_{exptl} (g/cm^3)	6.25	6.65	6.83	7.13	5.31

*linear absorption coefficient

[a]Standard deviations given in brackets.

TABLE 3-3

DATA COLLECTION AND REFINEMENT INFORMATION

	Crystal Radius (mm)	μR	Data collected to 2θ of (deg.)	Weighting Scheme Coefficients*			N(1)	N(2)	N	R	ωR**
				A	B	C					
La	.142	2.90	70.0	3.608	-.029	.0001	293	231	273	.050	.044
Nd	.149	3.68	65.0	.759	-.012	.0003	463	424	435	.024	.032
Sm	.100	2.79	65.0	3.018	-.008	.0007	458	398	414	.032	.042
Gd	.088	2.80	55.0	2.500	-.063	.0005	294	282	284	.015	.016
Y	.099	2.8[redacted]	55.0	6.119	-.192	.0017	278	250	264	.029	.026

*Coefficients are those in the weighting function $\omega = (A + B F_o + C F_o^2)^{-1}$

**$\omega R = \left[\frac{\Sigma\omega(|F_o| - |F_c|)^2}{\Sigma\omega F_o^2}\right]^{\frac{1}{2}}$

absorption coefficients are given in Tables 3-3 and 3-2, respectively).

3.4 Twinning

Precession photographs showed that the crystals of $SmTiO_3$ and $NdTiO_3$ used for data collection were twinned. The twinning was found to correspond to a reflection across the $(1\bar{1}0)$ plane. Figure 3-2 illustrates the effect of the twinning on the hk0 net with axes a* and b*. Twinned reflections (indicated by crosses) are related to reflections of the major component which are mirrored across the $(1\bar{1}0)$ plane, as is indicated for two reflections by arrows. The result is the appearance of a second hk0 net (with orthogonal axes a*' and b*') sharing hh0 reflections with the major component. For $SmTiO_3$, intensity data were collected separately for the two twin components. A plot of the intensities of the reflections assumed to be related by this twin law is shown in Figure 3-3. The strong linear correlation confirms the twinning model, with the slope equal to the volume ratio of the major component to the twinned component, 4.4:1 for $SmTiO_3$. Only the data for the major component were used in the refinement. The hhl ($h \neq 0$) reflections were not used since they lie on the twin plane and thus contain the twin component. Instead, the equivalent $h\bar{h}l$ reflections were used as they are nonsuperimposed. The 00l reflections were reduced

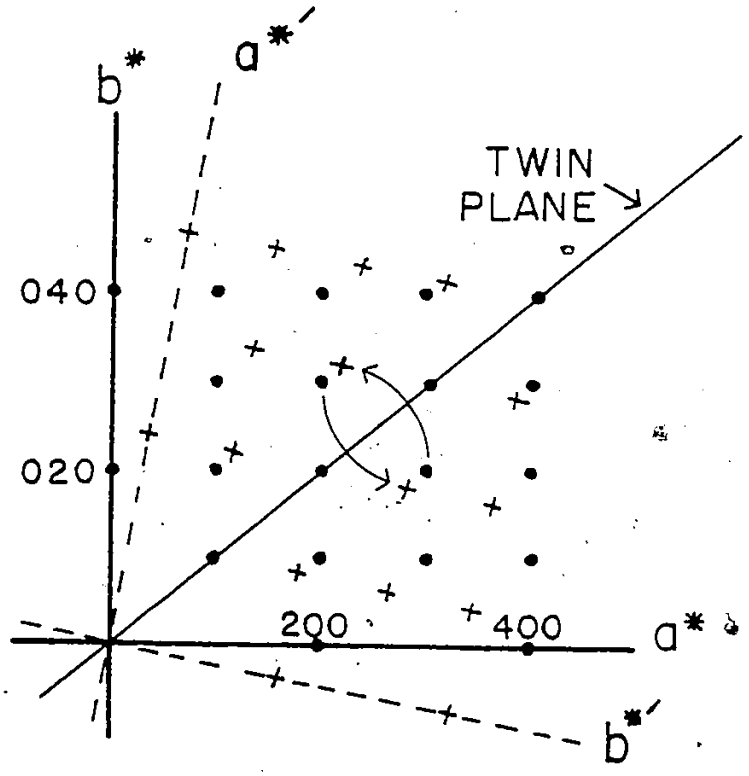

Figure 3-2. The appearance of the hk0 net under the twinning found in $SmTiO_3$ and $NdTiO_3$. Twinned reflections (indicated by x) are related to reflections of the major component by a mirror reflection across the twin plane.

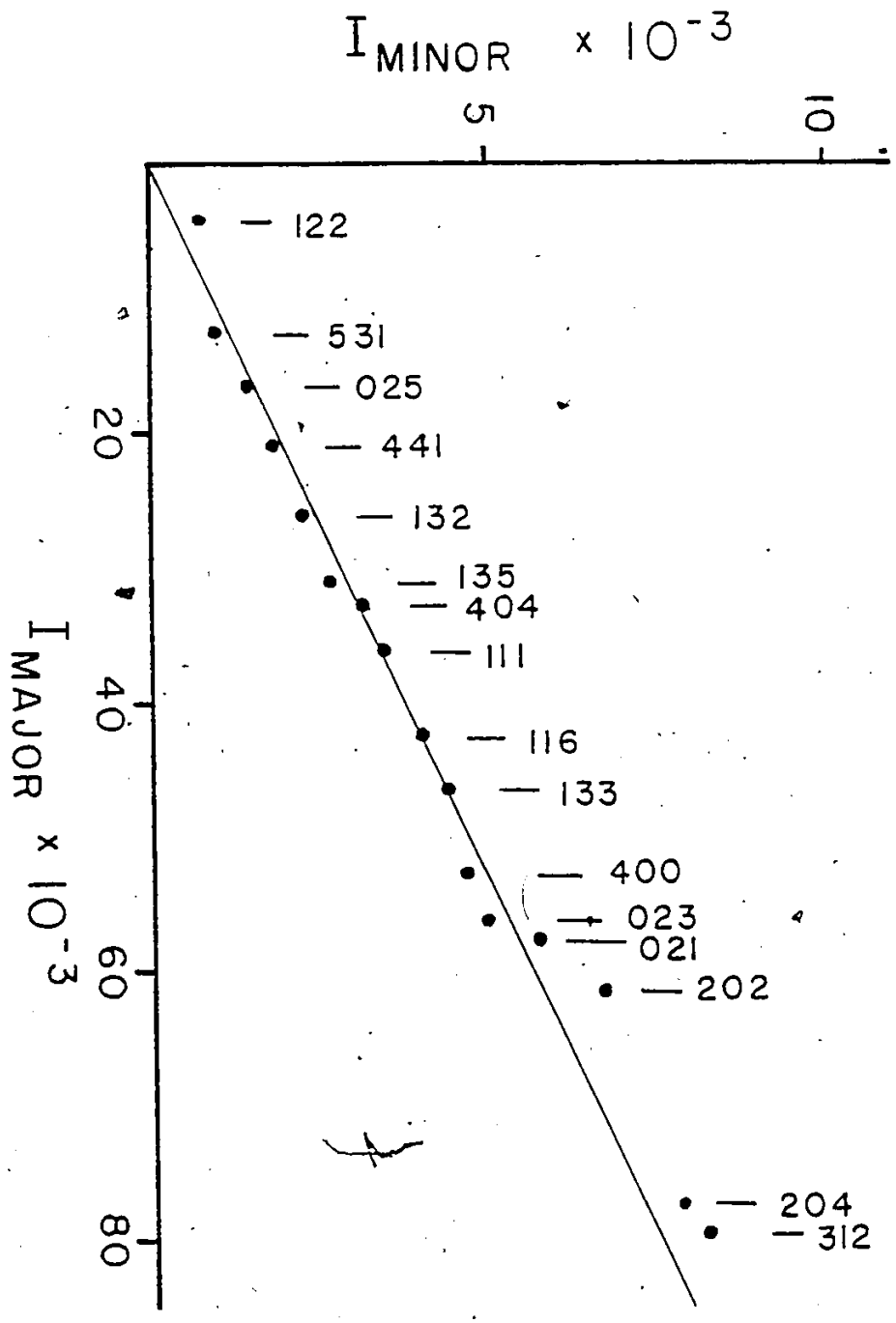

Figure 3-3. Relationship of the intensities of twinned reflections to the intensities of the reflections of the major component for $SmTiO_3$. Reflection indices (hkl) are shown above the data points.

by a factor of (4.4/5.4) before being used in the refinement since for these there are no equivalent nonsuperimposed reflections. For $NdTiO_3$, the volume ratio was found to be 10.8:1, and the data were handled in a manner identical to that of $SmTiO_3$.

The case of $LaTiO_3$ was quite different. Precession photographs were misleading in that they revealed a nearly cubic cell, $a \approx 7.91$ Å. Figure 3-4 is a diagram of the hk0 net for $LaTiO_3$ showing the 7.91 Å axes and their relationship to what are, in fact, the true orthorhombic axes, $a \approx 5.60$ Å, $b \approx 5.60$ Å. Indexed on an orthorhombic basis, the h0l and 0kl projections show obvious violations of the n and b glide plane symmetry of Pbnm, and still other reflections appear at half-integral coordinates with respect to the orthorhombic cell. The data for $LaTiO_3$ can be analyzed in terms of Pbnm, however, by postulating and proving the existence of a complex twinning. This twinning can be viewed as a combination of two basic operations.

The first and most predominant twin in $LaTiO_3$ corresponds to a 3-fold rotation about the body diagonal of the 7.91 Å pseudo-cube. This twinning results in three twin components, whose reflections (indexed in the orthorhombic cell) are related by the following transformation matrices:

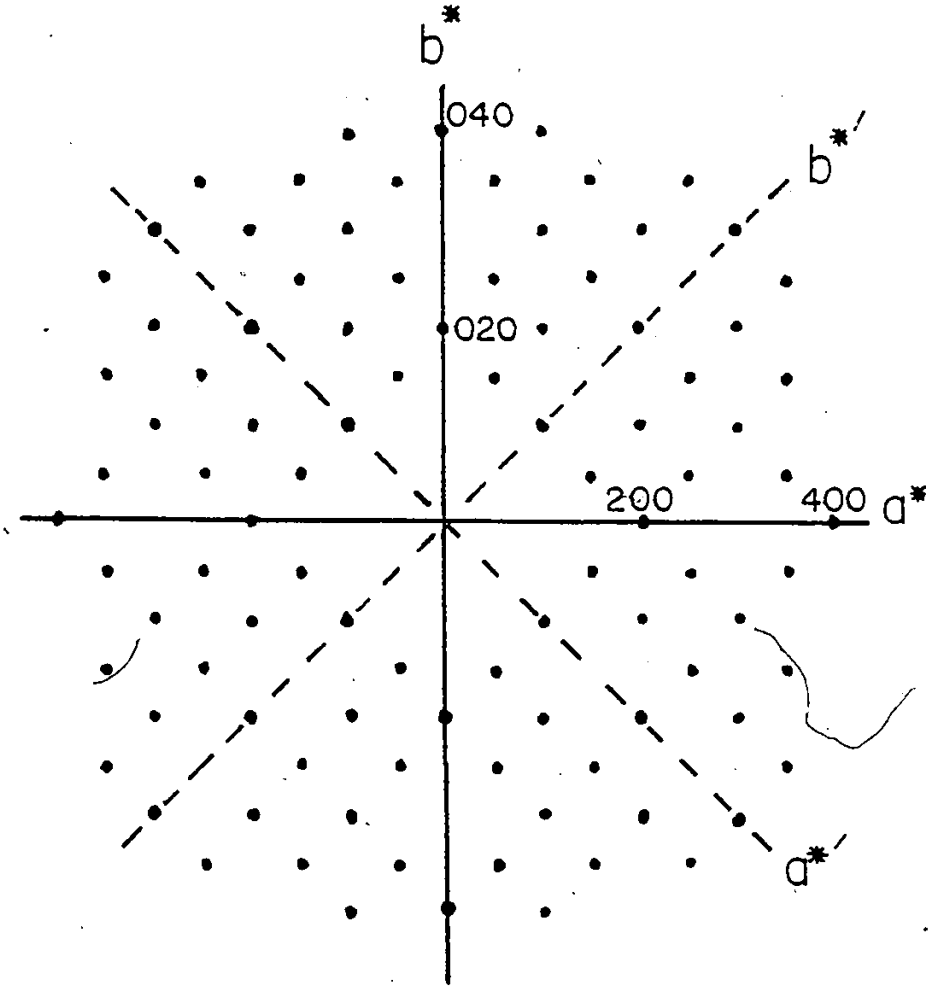

Figure 3-4. Appearance of the hk0 net of $LaTiO_3$ showing the relationship of the true orthorhombic axes (a*,b*) to the cubic axes (a*',b*'). Reflections at half-integral values with respect to the orthorhombic axes result from twinning in the crystal.

$$\begin{pmatrix} -1/2 & -1/2 & -1/2 \\ 1/2 & 1/2 & -1/2 \\ -1 & 1 & 0 \end{pmatrix} \begin{pmatrix} h \\ k \\ l \end{pmatrix} = \begin{pmatrix} h' \\ k' \\ l' \end{pmatrix}$$

$$\begin{pmatrix} 1/2 & -1/2 & 1/2 \\ 1/2 & -1/2 & -1/2 \\ 1 & 1 & 0 \end{pmatrix} \begin{pmatrix} h \\ k \\ l \end{pmatrix} = \begin{pmatrix} h'' \\ k'' \\ l'' \end{pmatrix}$$

It can be seen that reflections will be superimposed by this twinning only when $h + k + l = 2n$. When $h + k + l \neq 2n$, the twinning causes reciprocal lattice points to appear at half integral coordinates with respect to the orthorhombic lattice giving rise to the appearance of a 7.91 Å cubic cell. Thus, one can use those reflections for which $h + k + l \neq 2n$ in the structural refinement as they will be nonsuperimposed by this twinning.

From a data collection on the 7.91 Å cell, plots were made of the intensities of twin-related reflections, revealing volume ratios of 0.089:0.14:1. Data were then collected on the orthorhombic cell of the major twin component. Of the data collected, two types of reflections were used in the refinement. Firstly, as described above, were included those reflections for which $h + k + l \neq 2n$. Also used in the refinement were 29 reflections which contained intensities from the major twin component and the smallest twin component only. These reflections were reduced by a factor of 1/1.089 before being used.

The second twin operation present in $LaTiO_3$ is reflection across the $(1\bar{1}0)$ plane, as in $SmTiO_3$ and $NdTiO_3$. In the cases of $SmTiO_3$ and $NdTiO_3$, the a* and b* axes were of significantly different lengths so that this twinning did not cause superposition of reflections (other than hhl). However, in $LaTiO_3$, the a* and b* axes are essentially identical in length, and twinning across the $(1\bar{1}0)$ plane causes direct superposition of hkl and khl reflections. This results in the apparent violation of the n and b glide extinctions of Pbnm. This aspect of the twinning in $LaTiO_3$ is the same as that found in $LaFeO_3$.[42] Intensities were corrected using the formula:

$$I_{corr}(hkl) = \frac{1}{1-V} I_{meas}(hkl) - \frac{V}{1-V} I_{meas}(khl)$$

where V is the volume ratio determined by measuring the intensities of the forbidden reflections on the zone h0l and comparing them with the corresponding allowed 0kl reflections. For this crystal, the volume ratio was found to be 0.090.

It is interesting to compare the twinning found in $LaTiO_3$ with that for the isostructural $LaFeO_3$. Both crystals show evidence for the $(1\bar{1}0)$ reflection twin but $LaTiO_3$, which was grown from the melt, (2000°C) shows a three-fold rotational twin while the flux grown $LaFeO_3$ (1200°C) does not. This suggests that $LaTiO_3$ undergoes a high temperature phase transition from a rhombohedral or

cubic cell to the orthorhombic cell upon cooling.

3.5 Refinements

A full matrix least squares program that minimizes the function $\Sigma\omega(|F_o| - |F_c|)^2$ was used in the refinements. The weighting function used has the form $\omega = [A + B|F_o| + C|F_o|^2]^{-1}$ with the coefficients chosen in such a way that averages of $\omega(\Delta F)^2$ were approximately constant when the data were analyzed into regions of F_o. Atomic scattering curves for free ions were taken from Cromer and Waber,[43] and the real and imaginary anomalous dispersion coefficients were taken from Cromer.[44] The starting values used for the positional parameters were those of the corresponding $REFeO_3$. During the final stages of refinement, a secondary extinction parameter following Larson[77] was also refined in all cases except $LaTiO_3$. The final positional and thermal parameters are listed in Table 3-4. Tables of structure amplitudes are included in the Appendix.

3.6 Discussion

The results of this study of the $RETiO_3$ phases may be compared with the very careful work of Marezio *et al.*[45] on the isostructural $REFeO_3$ phases.

Figure 3-5 shows a projection of the $LaTiO_3$ structure on the xy plane. An oxygen-titanium octahedron and an oxygen-rare earth polyhedron are outlined. The

TABLE 3-4

FINAL POSITIONAL PARAMETERS AND THERMAL PARAMETERS ($x10^4$)[a]

		La	Nd	Sm	Gd	Y
RE	X	.9949(4)	.98892(5)	.98433(9)	.98103(5)	.97925(14)
	Y	.0323(19)	.05412(6)	.06444(9)	.06958(5)	.07294(12)
	Z	(.25)	(.25)	(.25)	(.25)	(.25)
	U_{11} †	139(4)	113(2)	105(3)	60(2)	63(4)
	U_{22}	186(16)	131(2)	86(3)	67(2)	37(4)
	U_{33}	124(4)	101(2)	103(3)	64(2)	64(4)
	U_{12}	-15(4)	-8(1)	-5(2)	-6(1)	-6(3)
	U_{13} *	(0)	(0)	(0)	(0)	(0)
	U_{23}	(0)	(0)	(0)	(0)	(0)
Ti	X	(0.0)	(0.0)	(0.0)	(0.0)	(0.0)
	Y	(0.5)	(0.5)	(0.5)	(0.5)	(0.5)
	Z	(0.0)	(0.0)	(0.0)	(0.0)	(0.0)
	U_{11}		80(4)	91(7)	51(4)	58(6)
	U_{22}		99(4)	91(7)	64(5)	37(6)
	U_{33}		69(5)	79(7)	39(5)	30(6)
	U_{12}	(U_{ISO}** = 86)	0(3)	1(5)	-1(3)	1(5)
	U_{13}		0(2)	0(5)	-5(3)	-10(6)
	U_{23}		-5(4)	0(6)	7(3)	-1(3)
O1	X	.0696(48)	.0902(8)	.1019(13)	.1095(8)	.1213(10)
	Y	.4912(13)	.4801(8)	.4735(13)	.4668(8)	.4580(9)
	Z	(.25)	(.25)	(.25)	(.25)	(.25)
	U_{11}	225(109)	108(17)	109(29)	123(18)	65(24)
	U_{22}	71(65)	154(17)	96(29)	77(19)	43(26)
	U_{33}	295(152)	74(16)	115(32)	62(19)	80(26)
	U_{12}	-41(25)	2(14)	12(23)	0(16)	12(21)
	U_{13}	(0)	(0)	(0)	(0)	(0)
	U_{23}	(0)	(0)	(0)	(0)	(0)
O2	X	.7150(22)	.7024(5)	.6958(8)	.6942(5)	.6909(6)
	Y	.2861(22)	.2979(5)	.3022(8)	.3063(5)	.3095(7)
	Z	.0368(15)	.0465(4)	.0524(7)	.0541(4)	.0579(5)
	U_{11}	199(33)	112(11)	115(18)	63(12)	72(18)
	U_{22}	182(30)	118(11)	66(18)	86(14)	54(19)
	U_{33}	195(36)	124(12)	104(20)	82(14)	78(18)
	U_{12}	-58(31)	-13(9)	-7(15)	-24(10)	-22(14)
	U_{13}	-36(35)	7(9)	25(16)	4(9)	-8(14)
	U_{23}	34(35)	-14(10)	-5(16)	-21(11)	-8(15)

*By symmetry, $U_{13} = U_{23} = 0$ for RE and O1.

**Temperature parameters for Ti in $LaTiO_3$ were not refined as no reflections containing information about Ti were included in the refinement.

†Calculated from $\beta_{ij} = 2\pi^2 b_i b_j U_{ij}$ where $T = \exp[-(\beta_{11} h^2 + 2\beta_{12} hk + \ldots)]$ is the thermal factor appearing in the structure factor expression and b_i's are reciprocal lattice vectors.

[a]Standard deviations given in brackets.

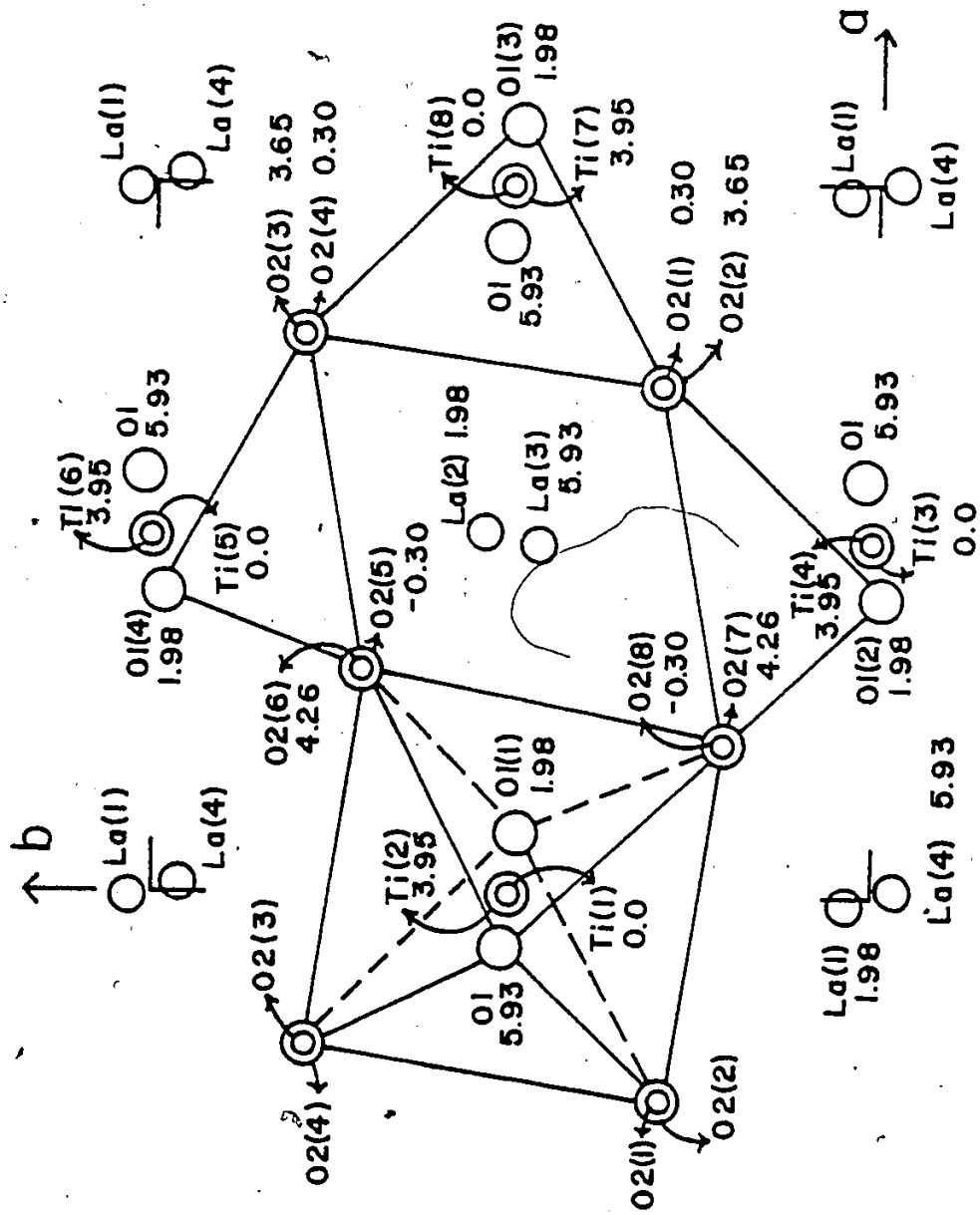

Figure 3-5. Projection of the $LaTiO_3$ structure on the a-b plane. The distances above or below the plane are given in angstroms. The numbering of the atoms refers to the data in Tables 3-5 to 3-7.

interatomic distances and angles are given in Tables 3-5, 3-6 and 3-7.

As in the $REFeO_3$, the oxygen polyhedron around the rare earth ions is very distorted. The twelve O-RE-O angles, which in the ideal cubic perovskite are 90°, vary from 121.7 to 60.7° in $YTiO_3$ and from 111.8 to 75.2° in $LaTiO_3$, which has the least distortion of the $RETiO_3$.

The RE-O distances are plotted in Figure 3-6 against the crystal radii[46] of the rare earths. Over this range of rare-earth radii, the first eight RE-O distances increase linearly from Y to La. This indicates that these oxygen atoms are nearest neighbours to the rare earth. The last four RE-O distances are significantly greater and all decrease as a function of rare earth ionic radius. This indicates that these four atoms are second nearest neighbours. Thus, over this range of rare earth radius, the $RETiO_3$ have an eight-coordinated rare earth ion. These results are similar in every respect to those for $REFeO_3$.

A different situation arises when one examines the transition metal-oxygen octahedron. In the study of the $REFeO_3$, it was found that the distortion of the Fe-O octahedron was small and increased only slightly in going from $LaFeO_3$ to $LuFeO_3$, the average Fe-O and O-O distances being nearly the same. In the $RETiO_3$, however, a significant distortion of the Ti-O octahedron occurs as a function of the rare earth ion. In Figure 3-7, the standard

TABLE 3-5

INTERATOMIC DISTANCES (Å) AND ANGLES (°) IN THE RARE EARTH POLYHEDRON[a]

	La	Nd	Sm	Gd	Y
RE(2) - 01(1)	2.450(27)	2.349(4)	2.315(7)	2.284(4)	2.221(5)
- 01(2)	3.054(14)	3.256(4)	3.405(7)	3.499(4)	3.573(5)
- 01(3)	3.170(27)	3.209(4)	3.238(7)	3.238(4)	3.259(5)
- 01(4)	2.599(14)	2.445(4)	2.403(7)	2.365(4)	2.314(5)
- 02(1),02(2)	2.474(14)	2.379(3)	2.345(5)	2.322(3)	2.279(4)
- 02(3),02(4)	2.704(14)	2.615(3)	2.572(5)	2.542(3)	2.508(4)
- 02(5),02(6)	2.773(13)	2.717(3)	2.712(5)	2.693(3)	2.684(4)
- 02(7),02(8)	3.309(13)	3.474(3)	3.578(5)	3.616(3)	3.645(4)
01(1)-RE(2)-01(2)	76.8(6)	70.0(1)	66.3(2)	63.8(1)	60.7(2)
01(2)-RE(2)-01(3)	93.7(6)	92.4(1)	91.7(2)	91.0(1)	90.7(1)
01(3)-RE(2)-01(4)	103.4(7)	110.6(1)	114.6(2)	117.4(1)	120.6(1)
01(4)-RE(2)-01(1)	86.1(7)	87.0(2)	87.4(3)	87.8(2)	88.0(1)
02(1)-RE(2)-02(2)	85.9(5)	83.4(1)	81.2(2)	80.6(1)	79.8(1)
02(1)-RE(2)-02(5)	81.8(4)	79.0(1)	78.1(2)	77.5(1)	76.7(1)
02(2)-RE(2)-02(3)	65.9(4)	69.2(1)	71.9(2)	73.3(1)	74.6(1)
02(2)-RE(2)-02(7)	57.8(4)	55.5(1)	54.0(1)	53.0(1)	52.2(1)
02(3)-RE(2)-02(4)	77.1(4)	74.5(1)	72.8(2)	72.4(1)	71.3(1)
02(3)-RE(2)-02(6)	63.6(4)	65.6(1)	66.7(2)	67.0(1)	67.3(1)
02(3)-RE(2)-02(7)	98.0(4)	100.8(1)	102.4(1)	103.2(1)	103.8(1)
02(5)-RE(2)-02(6)	109.7(4)	116.2(1)	118.9(1)	119.9(1)	121.7(1)
02(6)-RE(2)-02(7)	54.4(4)	53.0(1)	52.6(1)	52.5(1)	52.1(1)
02(7)-RE(2)-02(8)	86.5(4)	83.2(1)	81.5(1)	80.3(1)	80.0(2)
01(1)-RE(2)-02(6)	65.9(3)	68.2(1)	69.3(1)	69.8(1)	70.9(1)
01(1)-RE(2)-02(7)	57.4(4)	54.5(1)	52.8(1)	51.7(1)	50.6(1)
01(2)-RE(2)-02(2)	60.9(5)	58.8(1)	57.1(1)	56.5(1)	56.1(1)
01(2)-RE(2)-02(7)	53.1(4)	50.1(1)	48.6(1)	47.5(1)	46.8(1)
01(3)-RE(2)-02(2)	59.0(3)	59.0(1)	59.1(1)	58.9(1)	58.7(1)
01(3)-RE(2)-02(3)	57.3(3)	58.0(1)	58.6(1)	59.8(1)	60.6(1)
01(4)-RE(2)-02(3)	64.9(6)	68.3(1)	70.1(2)	70.8(1)	72.1(1)
01(4)-RE(2)-02(6)	64.4(4)	66.8(1)	67.6(1)	67.9(1)	68.2(1)

[a]Standard deviations given in brackets.

TABLE 3-6

RARE EARTH-TITANIUM DISTANCES (Å) AND Ti-O-Ti AND RE-O-Ti BOND ANGLES (°).[a]

	La	Nd	Sm	Gd	Y
RE(2)-Ti(1), Ti(2)	3.456(2)	3.429(1)	3.431(1)	3.415(1)	3.385(1)
RE(2)-Ti(3), Ti(4)	3.572(9)	3.657(1)	3.734(1)	3.767(1)	3.771(1)
RE(2)-Ti(5), Ti(6)	3.277(9)	3.162(1)	3.132(1)	3.112(1)	3.085(1)
RE(2)-Ti(7), Ti(8)	3.409(2)	3.330(1)	3.292(1)	3.249(1)	3.207(1)
Ti(2)-O1(1)-Ti(1)	157.5(1.5)	150.7(2)	146.8(4)	144.1(2)	140.3(3)
Ti(2)-O2(7)-Ti(4)	156.9(7)	150.3(2)	147.0(3)	145.7(2)	143.7(4)
Ti(1)-O1(1)-RE(2)	101.0(8)	103.5(1)	104.6(2)	105.1(1)	105.7(2)
Ti(1)-O1(1)-RE(1)	88.6(3)	89.9(1)	89.9(2)	90.2(1)	90.4(2)
Ti(4)-O2(2)-RE(1)	91.2(5)	90.6(1)	90.0(2)	88.9(1)	88.2(1)
Ti(1)-O2(5)-RE(2)	91.0(4)	91.6(1)	91.3(2)	91.6(1)	91.0(1)
Ti(5)-O2(5)-RE(2)	84.7(4)	82.1(1)	80.9(2)	80.3(1)	79.7(1)
Ti(7)-O2(1)-RE(1)	86.7(5)	85.0(1)	84.7(2)	85.1(1)	85.2(1)
Ti(8)-O2(1)-RE(2)	98.3(5)	98.1(1)	97.0(2)	96.5(1)	96.4(3)
Ti(3)-O2(1)-RE(2)	104.8(5)	111.7(1)	115.9(2)	117.8(1)	119.9(2)

[a]Standard deviations given in brackets.

TABLE 3-7

INTERATOMIC DISTANCES (Å) AND ANGLES (°) IN THE TITANIUM OCTAHEDRON[a]

	La	Nd	Sm	Gd	Y
Ti-01(1)	2.015(5)	2.010(1)	2.014(2)	2.014(1)	2.023(2)
Ti-02(6)	2.016(12)	2.020(3)	2.042(5)	2.027(3)	2.016(4)
Ti-02(7)	2.023(12)	2.035(3)	2.056(5)	2.076(3)	2.077(4)
01(1)-02(6)	2.854(17)	2.856(4)	2.878(7)	2.867(4)	2.869(5)
01(1)-02(7)	2.865(15)	2.849(4)	2.855(7)	2.839(4)	2.817(5)
01(1)-02(2)	2.846(23)	2.843(5)	2.859(8)	2.847(5)	2.843(6)
01(1)-02(3)	2.846(17)	2.872(5)	2.902(8)	2.944(5)	2.979(6)
02(6)-02(7)	2.822(17)	2.843(4)	2.891(6)	2.908(4)	2.908(5)
02(6)-02(3)	2.889(17)	2.891(4)	2.905(7)	2.893(4)	2.881(5)
01(1)-Ti(2)-02(7)	90.4(6)	89.5(2)	89.1(3)	87.9(2)	86.8(2)
01(1)-Ti(2)-02(1)	90.2(7)	90.3(2)	90.4(3)	90.4(2)	90.5(2)
02(7)-Ti(2)-02(6)	88.7(5)	89.0(1)	89.7(2)	90.3(1)	90.5(1)
Average Ti-0	2.018(10)	2.022(3)	2.037(4)	2.039(3)	2.039(4)
Std. Deviation of Ti-0	.0043	.0126	.0214	.0327	.0334

[a]Standard deviations given in brackets.

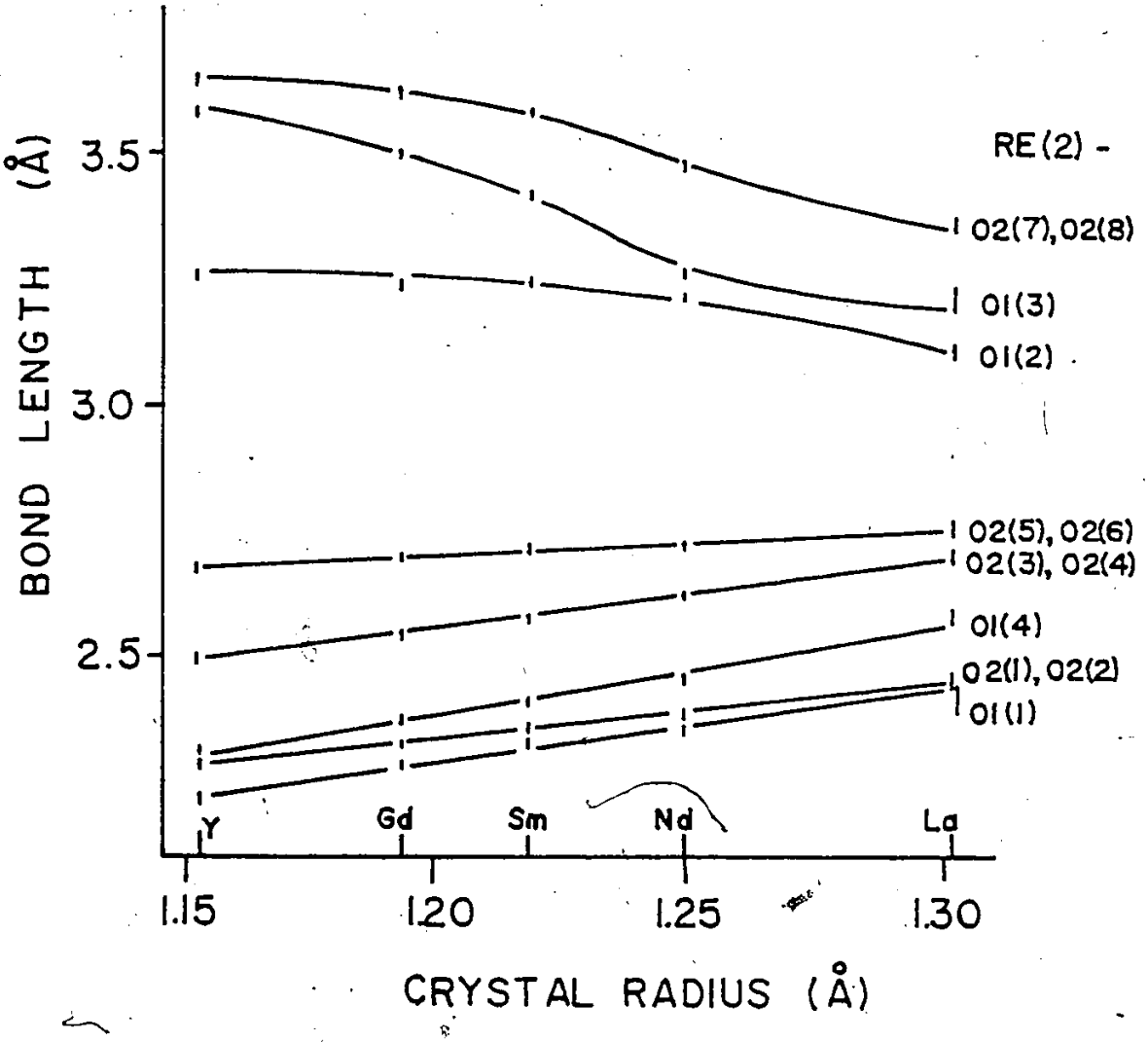

Figure 3-6. RE-O distances in the $RETiO_3$. The uncertainty in the distances is approximated by the length of the data points.

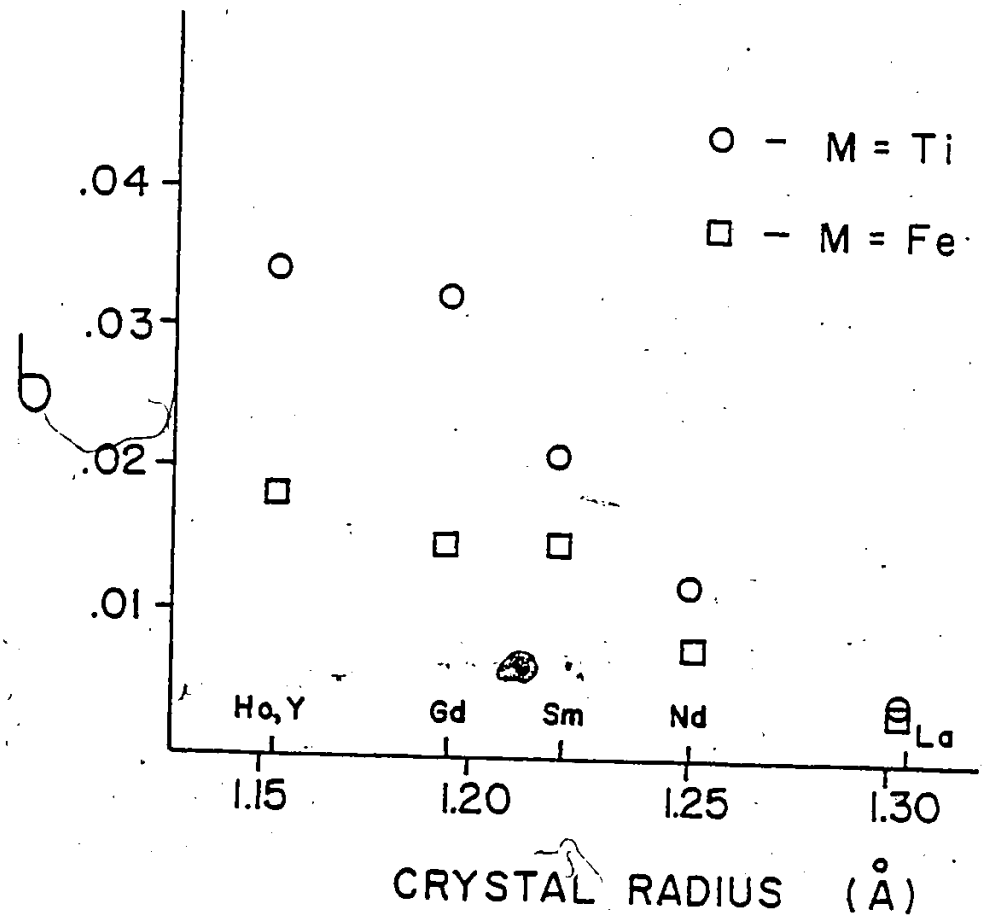

Figure 3-7. The standard deviation (σ) from the mean for the three inequivalent M-O bond lengths in $REMO_3$, M = Ti and Fe.

deviation from the mean for the three inequivalent Ti-O bond lengths is plotted versus the RE radius in $RETiO_3$ along with those for Fe-O in $REFeO_3$ for comparison. In contrast to the relatively smooth variation for σ(Fe-O), σ(Ti-O) shows a sharp increase between RE = Nd and RE = Gd. The data of Table 3-7 show that for RE = Gd and Y, a pronounced tetragonal-like distortion exists with two trans Ti-O bonds being much longer than the other four. For RE = La, the octahedron is undistorted while a very minor, possibly insignificant, distortion occurs for RE = Nd. The case for RE = Sm is intermediate in character. As will be argued in later chapters, there appears to be a strong correlation between this pseudo-tetragonal distortion and the magnetic, optical and electrical properties of these materials.

Another structural parameter which may be important in the determination of the properties of the $RETiO_3$ phases is the Ti-O-Ti bond angle.[2] These data are listed in Table 3-6 and plotted in Figure 3-8 for $REFeO_3$ and $RETiO_3$. Note the relatively smooth increase in average bond angle from RE = Y,Ho to RE = La for both series, there being no discontinuous changes between RE = Y,Gd and RE = La,Nd as was found in the Ti-O coordination polyhedron.

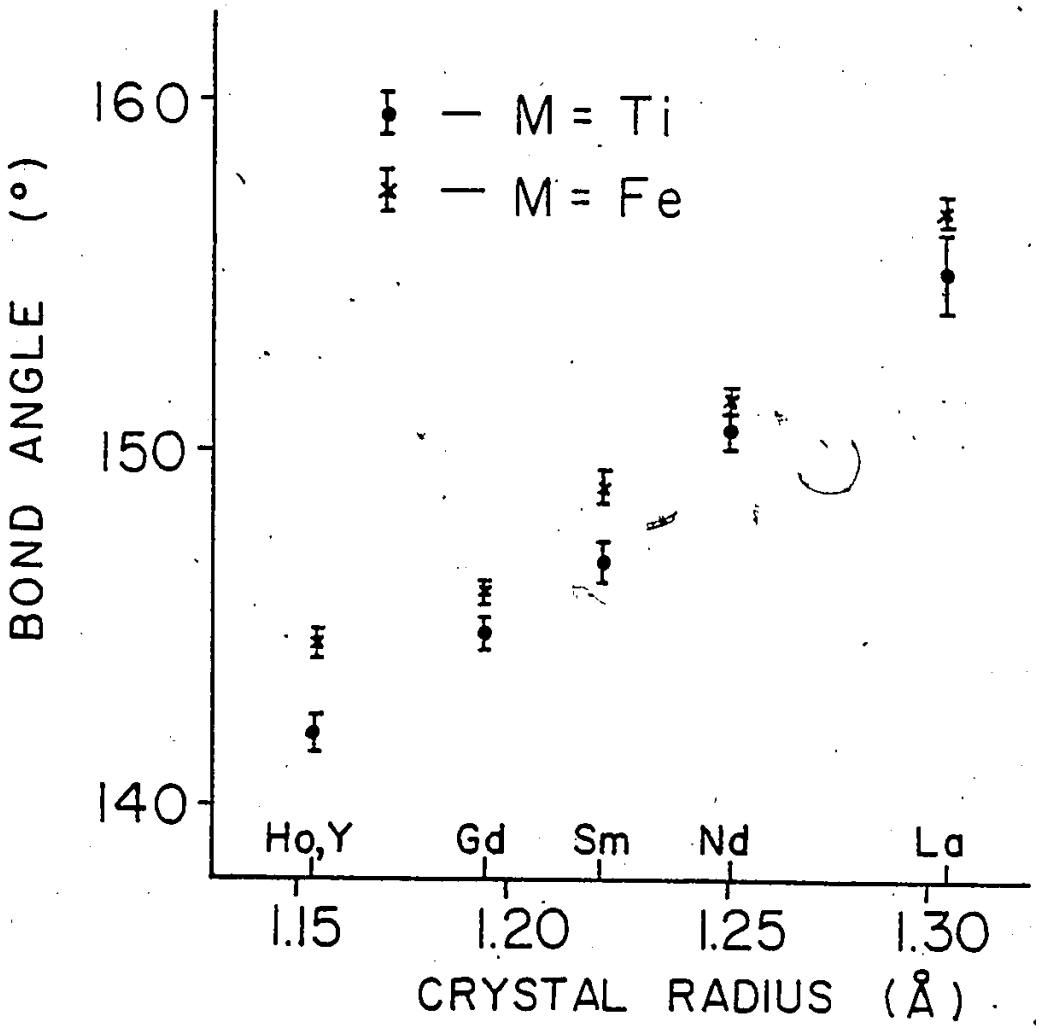

Figure 3-8. Average M-O-M bond angle in the $REMO_3$, M = Ti , Fe.

Chapter 4

EXPERIMENTAL PROCEDURES

As discussed in Chapter 1, it is of interest to determine for which $RETiO_3$ the d-electrons behave in a localized manner and for which they are best described as collective. To this end, magnetic, transport and optical experiments have been performed on various $RETiO_3$. The results of these experiments with comparison to results found by other workers are presented in Chapter 5. This chapter provides details of the experimental procedures used.

4.1 Magnetic Measurements

a) Sample Preparation

Except for single crystal measurements on $YTiO_3$, samples of the $RETiO_3$ were ground into fine powders and pressed into pellets for magnetic measurements. Mass of the samples varied from 100-300 mg. For samples with low moments, a diamagnetic correction after Selwood[47] was applied. For measurements of type (b) and (c) below, the pellets were attached to the end of four millimeter quartz tubes with ceramic cement (Sauereisen Cements Company, Pittsburgh). Single crystal $YTiO_3$ was attached to the end of the quartz tube using G.E. 7031 varnish which

could be dissolved away from the sample in toluene-methanol (50:50) allowing remounting of the sample for study at different orientations.

(b) Magnetization Data as a Function of Field (0-1.5 T) or Temperature (4.2°-300°K)

These data were collected using a Princeton Applied Research vibrating sample magnetometer with a Magnion water-cooled electromagnet. A temperature of 4.2°K was obtained using an Andonian Associates liquid helium dewar, and was monitored using a calibrated cromel vs. gold-0.07 atomic percent iron thermocouple. The sample temperature could be varied from 4.2°K to 300°K using a heater, and the electromagnet could be ramped up or down in field at a constant rate.

Voltages proportional to magnetization and applied field or temperature were monitored by a Texas Instruments on-line mini-computer which produced a histogram of magnetization vs. field or temperature. The magnetometer was calibrated using a pure nickel sphere of 0.07507 grams, and a calibration constant was determined using the accepted value of 55.11 ± 0.06 emu-g^{-1} at 4.2°K for the magnetic moment of nickel.[43]

This system was also used to perform orientational studies of a single crystal of $YTiO_3$. The crystal could

be rotated around one axis while the response of the magnetization was monitored.

(c) Magnetization Data as a Function of Field (0-6.0 T) at 1.2°K.

These data were obtained using a superconducting solenoid in a Sulfrian Cryogenics liquid helium dewar. A temperature of 1.2°K was obtained by pumping on liquid ^{4}He and field sweeps were done at that temperature. For some experiments, the field was held constant and the temperature was varied using a heater wound around the sample. This apparatus was calibrated as in (a) and the same data collection apparatus was used.

(d) Data for Samples with Weak Signals

For some samples, magnetic data were collected in the temperature range 80°K-300°K using the Faraday method. These data were supplied through the courtesy of Dr. A.P.B. Lever at York University.

4.2 Transport Measurements

Samples used for transport measurements were crystals which were grown as described in Chapter 2.

The transport studies of $NdTiO_3$ and $GdTiO_3$ were kindly performed by Dr. R.D. Shannon at the Dupont Laboratories in Wilmington, Delaware. The crystals were cut into bars 2.25 x 1.50 x 0.58 mm ($GdTiO_3$) and

2.20 x 1.00 x 0.43 mm ($NdTiO_3$) and the resistivity was measured as a function of temperature using the four probe technique with indium contacts on the samples.

Studies of $LaTiO_3$, $CeTiO_3$ and $PrTiO_3$ were done by the author. Crystals of these materials were cut into discs of arbitrary shape and polished on both sides. Disc thicknesses ranged from 0.18 mm ($LaTiO_3$) to 0.26 mm ($PrTiO_3$) and the maximum disc diameter was always less than 3 mm. Indium contacts were placed on samples by masking the entire disc with paraffin and cutting four holes through the coating around the circumference. The metal was then evaporated onto the masked disc, leaving four contacts on the circumference when the wax was removed. The sample was then mounted on an I.C. header as shown in Figure 4-1, and silver paste was used to make contact between the indium and four I.C. pins. The header was placed in a holder which was then used in the transport experiments. The technique used to determine the resistivity was that developed by L.J. van der Pauw.[49]

A schematic of the apparatus used to measure the d.c. resistivity of $LaTiO_3$, $CeTiO_3$ and $PrTiO_3$ is shown in Figure 4-2. The current direction was reversed at ten second intervals and the voltage signal was rectified and filtered to eliminate thermocouple effects at the sample voltage contacts. Sample temperature was varied slowly between 4.2° and 300°K in a Sulfrian Cryogenics

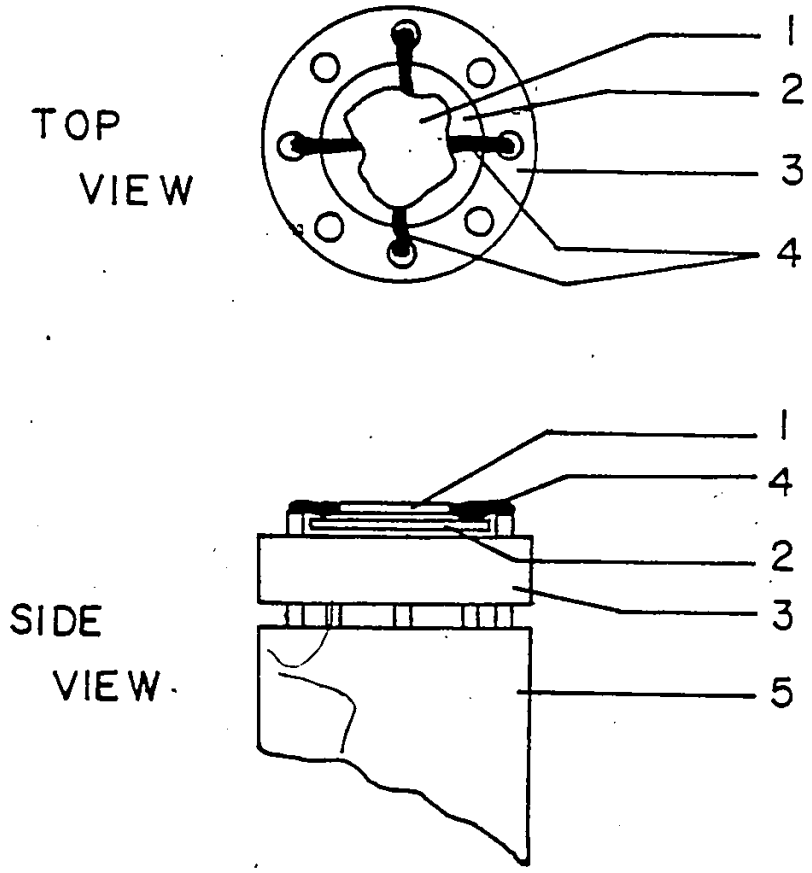

Figure 4-1. Technique of mounting crystals for transport studies. Items indicated in the diagrams are 1) the crystal; 2) mica; 3) I.C. header; 4) silver leads; 5) holder.

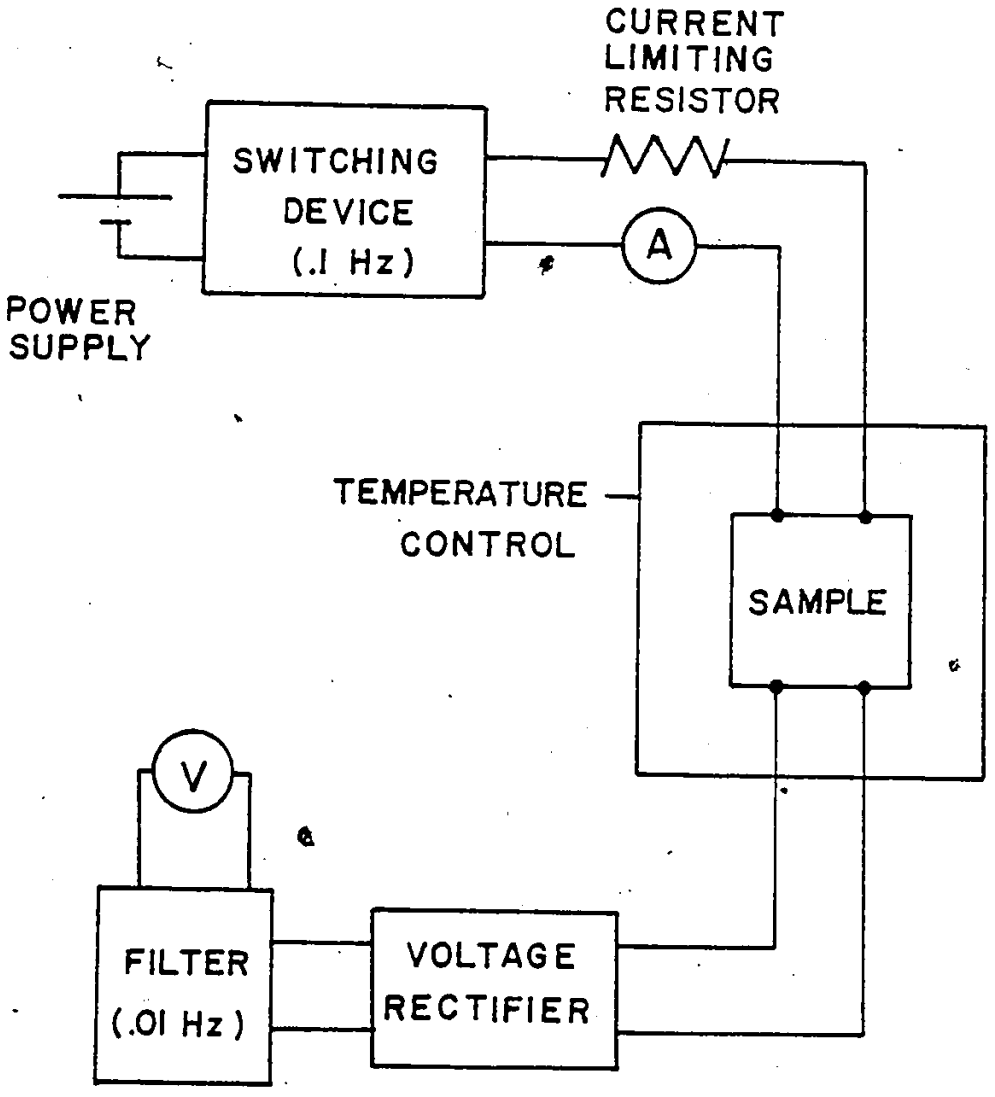

Figure 4-2. Schematic of the apparatus used to measure transport properties.

Inc. liquid helium dewar while the temperature was monitored with a calibrated cromel-gold-0.07 atomic percent iron thermocouple. Current and voltage leads could be rotated for alternate configuration measurements without removing the sample from the dewar.

4.3 Optical Measurements

Samples used for optical studies were single crystals which were obtained as described in Chapter 2. They were cut into thin samples, which were then polished until they were as thin as possible and could still be handled. The final crystal thicknesses are given in Table 4-1.

TABLE 4-1

$RETiO_3$ Crystal Thicknesses

RE	Thickness (μm)
La	83
Nd	309
Gd	109
Y	70

Masks were made for the samples by etching their images on 25 μm brass foil. The samples were then mounted in the foil and silver paste was used to fill in any discrepancies between the sample and mask shapes.

Two distinct types of optical experiments were

performed. On $LaTiO_3$ and $NdTiO_3$, where the expected activation energies, based upon transport work, were 0.008 eV and 0.03 eV, respectively, low temperature (1.2°K) experiments were performed using Fourier transform spectroscopy in the spectral range 0.005 eV to 0.087 eV. These experiments[50] were done using a Michelson interferometer (RIIC FS 720), a SM35 (American Ultraviolet Co.) mercury arc lamp, and a doped germanium bolometer maintained at 0.3°K in a ^3He system as a detector. Black polyethylene was used to filter out radiation of frequency over 0.087 eV. Approximately five square millimeters of sample were exposed to the radiation.

For the materials $GdTiO_3$ and $YTiO_3$, the estimated activation energies based upon transport studies were $\sim$ 0.17 eV so that infrared experiments could be performed at room temperature (where $kT \sim 0.025$ eV). These samples, after mounting in brass foil, were centered in the beam of a Nicolet Fourier transform infrared spectrometer. Approximately five square millimeters of sample were exposed to radiation. Transmission spectra in the frequency range 4000-400 cm^{-1} were obtained using a Globar source and a TGS detector at room temperature. Each spectrum was an average of 500 scans. Transmission spectra were also obtained in the far infrared at low temperatures using the Michelson apparatus described above.

Chapter 5

MAGNETIC, TRANSPORT AND OPTICAL STUDIES

In this chapter, the results of magnetic, transport and optical studies of various $RETiO_3$ phases are presented. In the first section, the findings of previous workers are presented. Sections 2 to 5 contain the experimental results obtained from this work. Those $RETiO_3$ which show roughly similar behavior are grouped together in sections 2 to 4, and section 5 presents the experimental behavior of the $La_xY_{1-x}TiO_3$ series.

5.1 Previous Work

i) Magnetic Studies

Table 5-1 summarizes the previous magnetic results for the $RETiO_3$, RE = La, Ce, Pr, Nd, Gd and Y. While some workers have investigated magnetic properties of these materials at high temperatures (300 K), few magnetic measurements have been made below 80 K. Inferences of magnetic structure and low temperature behavior have often been made from high temperature data.

It is apparent from Table 5-1 that agreement between

Table 5-1

Previous Magnetic Results for RE TiO_3, RE = La,Ce,Pr,Nd,Gd,Y

RE	Temperature Range Investigated(K)	Paramagnetic Data: Curie-Weiss Behaviour?	C_M(cm^3-K-$mole^{-1}$)	θ_C(K)	Long Range Order?	T_C(T_N)(K)
La	?	No	-	-	No	-
	80 - 300	No	-	-	No	-
	80 - 350	No	-	-	Yes	130
Ce	90 - 300	Yes	.98	+ 8	No	-
	80 - 350	Yes	1.02	-72	Yes	124
Pr	90 - 300	Yes	1.58	+19	No	-
	80 - 350	Yes	1.92	-65	Yes	90
Nd	1.2- 20	Yes	.80	- 2	No	-
	90 - 300	Yes	1.60	0	No	-
	80 - 300	Yes	1.60	0	No	-
	80 - 300	Yes	1.59	- 7	No	-
Gd	1.3- 70	Yes	7.90	0	Yes	21
	90 - 300	Yes	7.51	0	No	-
Y	80 - 650	Yes	.31	38	No	-
	4.2- 300	Yes	.36	33.1	Yes	29

continued .....

Table 5.1 (continued)

RE	$\mu_{Saturation}(\mu_B)$/ Temp(K)	Comments	Reference
La	-	Claim Pauli paramagnetism, no magnitude given, reference made to unpublished work by S. Kern and D. B. Rogers	3,8,51
	-	χ_{M_3} varies from 2500 to 1250x10^{-6} cm^3 -$mole^{-1}$ from 80K to 300K, claim exchange enhanced Pauli paramagnetism	20
	.003/80	Report Pauli paramagnetism, χ_{Pauli} = 560 x 10^{-6} cm^3-$mole^{-1}$	26
Ce	-	-	53
	.22/80	Claim canted antiferromagnetic ordering of Ti^{+3} sublattice.	54
Pr	-	-	53
	.17/80	Claim canted antiferromagnetic ordering of Ti^{+3} sublattice	54
Nd	-	-	55
	-	-	53
	-	-	20
	-	-	26
Gd	.54/1.3	Suggests ferromagnetic ordering of Ti^{+3} sublattice	55
	-	-	53
Y	-	Predicts ferromagnetism at lower temperatures	25
	.8/4.2	-	56

workers is not good in most cases for presumably the same materials. The reason for this is not clear, but is most likely due to differing quality and composition of samples used in these studies. Clearly, there is a need for investigations with samples of known purity and composition, and to temperatures below the lower limit of 80 K achieved by most workers. The magnetic studies reported in this chapter fulfill these needs by employing samples of known quality and by extending the investigated temperature range down to 4.2 K and in some cases, 1.2 K.

ii) Transport Studies

The results of previous transport studies of the $RETiO_3$, RE = La, Ce, Pr, Nd, Gd and Y are given in Table 5-2.

Again, the agreement between different groups working on the same materials is not good in many cases. In fact, the last two reports on $YTiO_3$, which differ remarkably in the observed activation energy, are from the same group of workers using polycrystalline samples that were prepared on different occasions. Differences such as these are not uncommon when transport measurements are performed on polycrystalline samples. In a controlled study by Shannon et al.,[57,58,59] it was found that resistivity measurements on polycrystalline sintered pellets of $Li_{15}Si_3PO_{16}$ were two to five times higher than measurements

Table 5-2. Previous Transport Results for Re TiO_3, RE = La,Ce,Pr,Nd,Gd and Y

RE	Temperature Range Investigated (K)	$\frac{d\rho}{dT}$*	E_a** (eV)	ρ at 300K (Ω-cm)	Polycrystalline sample?	Comments	Ref.
La	?	> 0	-	?	yes	No details of sample preparation or characterization	51
	150-450	> 0	-	1.6×10^{-2}	yes	ρ falls to 1.3×10^{-2} Ω-cm	20
	300-1100	> 0	-	1×10^{-3}	yes	ρ rises to 8×10^{-3} Ω-cm at 1100K	26
Ce	300-1100	= 0	0	1×10^{-2}	yes	-	26
Pr	300-1100	= 0	0	2×10^{-2}	yes	-	26
Nd	150-450	< 0	.02	3×10^{-2}	yes	-	20
	300-1100	< 0	.06	1.5×10^{-1}	yes	-	26
Gd	300-1100	< 0	.19	28	yes	-	26
Y	150-450	< 0	.02	10	yes	-	20
	300-1100	< 0	.42	120	yes	-	25
	300-1100	< 0	.23	120	yes	-	26

* $\frac{d\rho}{dT} > 0$ suggests metallic resistivity, $\frac{d\rho}{dT} < 0$ suggests activated resistivity.

** Calculation based upon an activated resistivity of the form $\rho = \rho_o \exp [E_a/k_B T]$

performed on a single crystal. Presumably the higher resistivity comes about because of the resistances which occur at grain boundaries in the sample.

What is also remarkable about the data in Table 5-2 is that while it is generally accepted that $LaTiO_3$ is metallic, the heavier $RETiO_3$ are claimed to have activated resistivities. Such a change in the electronic behavior of the d-electrons of a transition element is unprecedented in $REMO_3$ series, where M is a transition element, as the rare earth ion varies across the lanthanide series.

Certainly, the definitive transport experiments are those done on single crystal samples, and it is those experiments which are reported in this chapter for the $RETiO_3$, RE = La, Ce, Pr, Nd and Gd*. These experiments also extend to lower temperatures the range over which most of these materials have been studied (down to 4.2 K in some cases).

iii) Optical Studies

The optical properties of materials structurally similar to the $RETiO_3$ have been extensively investigated. The electronic and infrared spectra of the rare earth perovskite orthochromites, manganites and ferrites in general are characteristic of the parent transition metal

* twinned crystals in the case of RE = La, Ce, Pr, Nd.

oxides slightly modified by the presence of the rare earth ion.[6,8] Detailed studies of the infrared absorption of $BaTiO_3$ [60] and the $REMO_3$, M = Al, Cr, Fe and Co,[61] show that the infrared-active M-O and RE-O vibrations occur in the energy region 800 cm^{-1} and below.

The only optical studies that have been reported for the $RETiO_3$ phases have been by Bazuev and Shveikin.[62] From room temperature measurements on $RETiO_3$ powders, RE = Nd, Gd and Y, they report no absorption peaks in the range 800 cm^{-1} to 2000 cm^{-1}. In the region 400 cm^{-1} to 700 cm^{-1}, they report the presence of two intense broad bands, the lower one being split into two or three components. As in the $REMO_3$, M = Al, Cr, Fe and Co, these absorptions are assigned to Ti-O and RE-O vibrations. A group theoretical analysis of the space group Pbnm to which these materials belong predicts six infrared-active vibrations.[61] Some of these, however, may occur below 400 cm^{-1}.

Bazuev and Shveikin report that $LaTiO_3$ is opaque over the frequency range studied, and conclude that this material is a metal. For such a case, the presence of empty states at the Fermi level would cause intense absorption of radiation over a wide frequency range, including the infrared. They go on to conclude that in the $RETiO_3$ which were not opaque and for which infrared absorption peaks could be observed, the d-electrons are localized

in the t_{2g} levels of the Ti^{+3} ion.

The optical work being reported in this chapter is the result of an infrared investigation of single crystal $RETiO_3$, RE = La, Nd, Gd and Y. The aim was not to study the Ti-O and RE-O vibrations at energies 800 cm^{-1} and below, but rather to investigate regions where evidence for electronic transitions would be expected.

5.2 $LaTiO_3$ and $CeTiO_3$

The temperature dependence of the molar susceptibility of $LaTiO_3$ is shown in Figure 5-1. In the temperature range 300 K to 130 K, the molar susceptibility, corrected for diamagnetism, is essentially temperature independent at a value $\chi_M = 800 \pm 20 \times 10^{-6}$ cm^3 $mole^{-1}$. This magnetic behaviour is characteristic of Pauli paramagnets, although the magnitude of the susceptibility is higher than that found for most metals which exhibit Pauli paramagnetism[9] (i.e., $\chi_{Pauli}(Nb) = 190 \times 10^{-6}$ cm^3 $mole^{-1}$, $\chi_{Pauli}(W) = 590 \times 10^{-6}$ cm^3 $mole^{-1}$, $\chi_{Pauli}(V) = 250 \times 10^{-6}$ cm^3 $mole^{-1}$). However, the cubic perovskite, $SrCrO_3$, which has a metallic conductivity exhibits Pauli paramagnetism with a susceptibility of 750×10^{-6} cm^3 $mole^{-1}$.[63] As the Pauli susceptibility is of the form

$$\chi_{Pauli} \cong \mu_B^2 \, g(E_F) \qquad (5\text{-}1)$$

where μ_B is the Bohr magneton and $g(E_F)$ is the density of

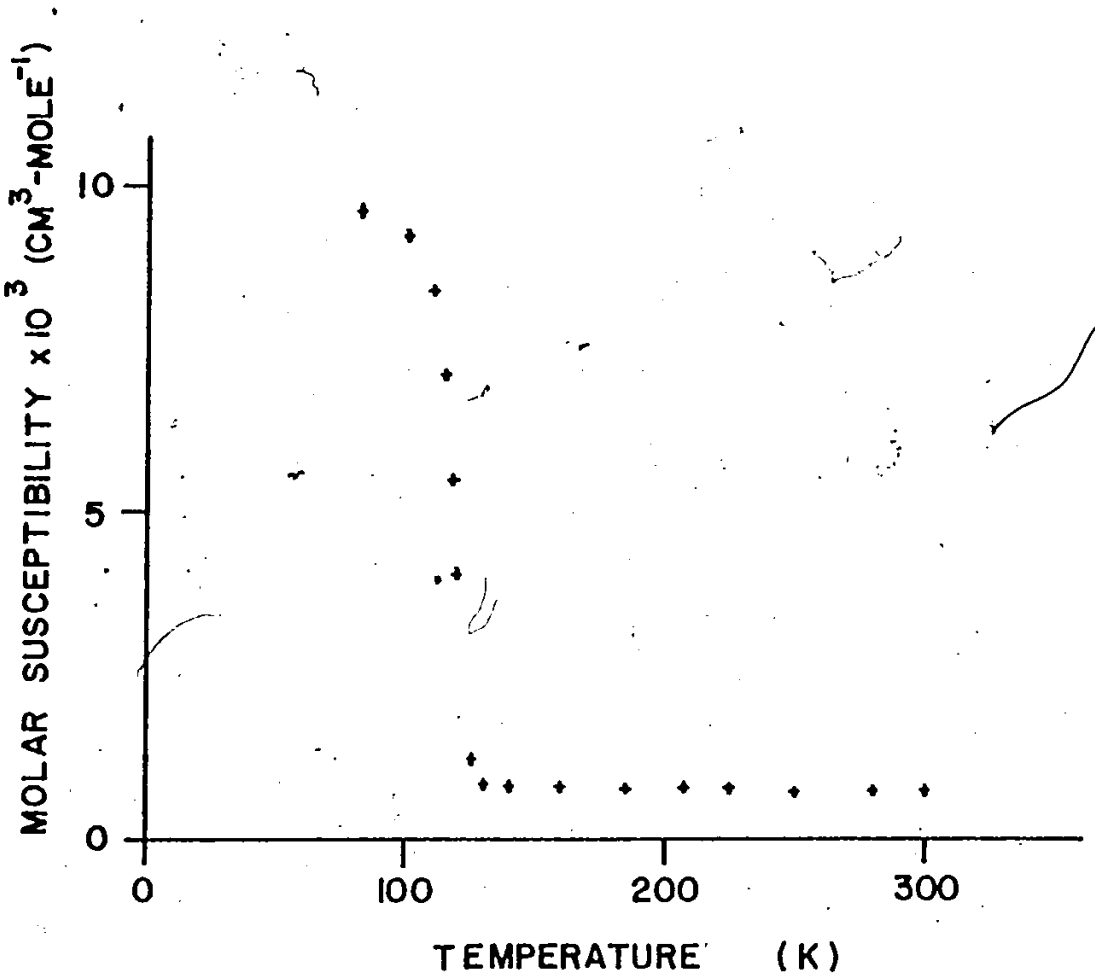

Figure 5-1 Response of the molar susceptibility of $LaTiO_3$ to temperature.

states at the Fermi level, the high value of χ_M for $LaTiO_3$ may suggest that the density of states at the Fermi level is higher in this case than in most Pauli paramagnets. When transition metal-oxide systems like the $RETiO_3$ do behave as metals, the bands are generally narrow and a high density of states would be expected at the Fermi level.[7]

Below 130 K, the susceptibility rises rapidly, indicating the onset of magnetic ordering. Figure 5-2 shows the field dependence of the magnetization at 4.2 K. These data show a hysteresis, suggesting ferromagnetism. Note the low saturation moment observed, $\sim .007\ \mu_B$- $mole^{-1}$.

The transport behaviour of $LaTiO_3$ is shown in Figure 5-3. The resistivity decreases gradually from 300 K to 130 K. This behaviour is characteristic of metals, and is at least qualitatively consistent with that reported by Bazuev et al.[26] and Ganguly et al.[20] Below 130 K, the resistivity increases as the temperature is lowered, creating a resistivity minimum.

Clearly the magnetic and transport data for $LaTiO_3$ indicate that the d-electrons are delocalized above 130 K. Both the temperature-independent Pauli susceptibility and the increasing resistivity with increasing temperature call for this conclusion. The low temperature data are not so easily interpreted, however.

Consider the minimum in the resistivity curve. Some materials which show resistivity minima do so because

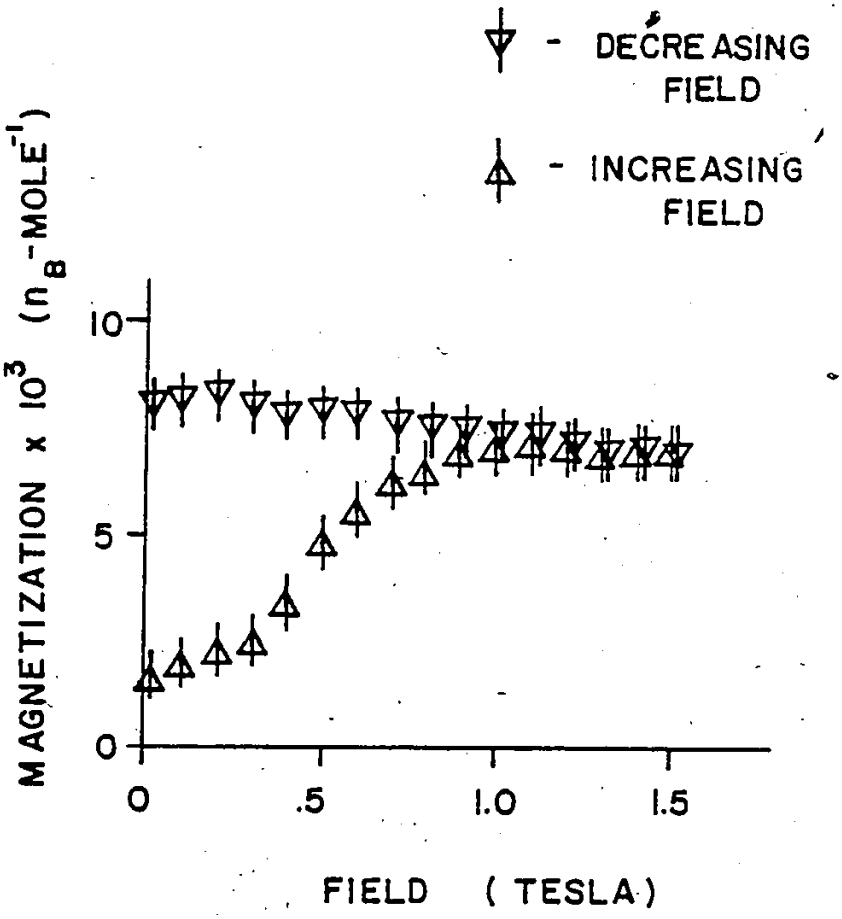

Figure 5-2. Magnetization versus field data for $LaTiO_3$ at 4.2°K. Data was collected for field increasing from 0 T. to 1.5 T., and then for field decreasing to 0 T.

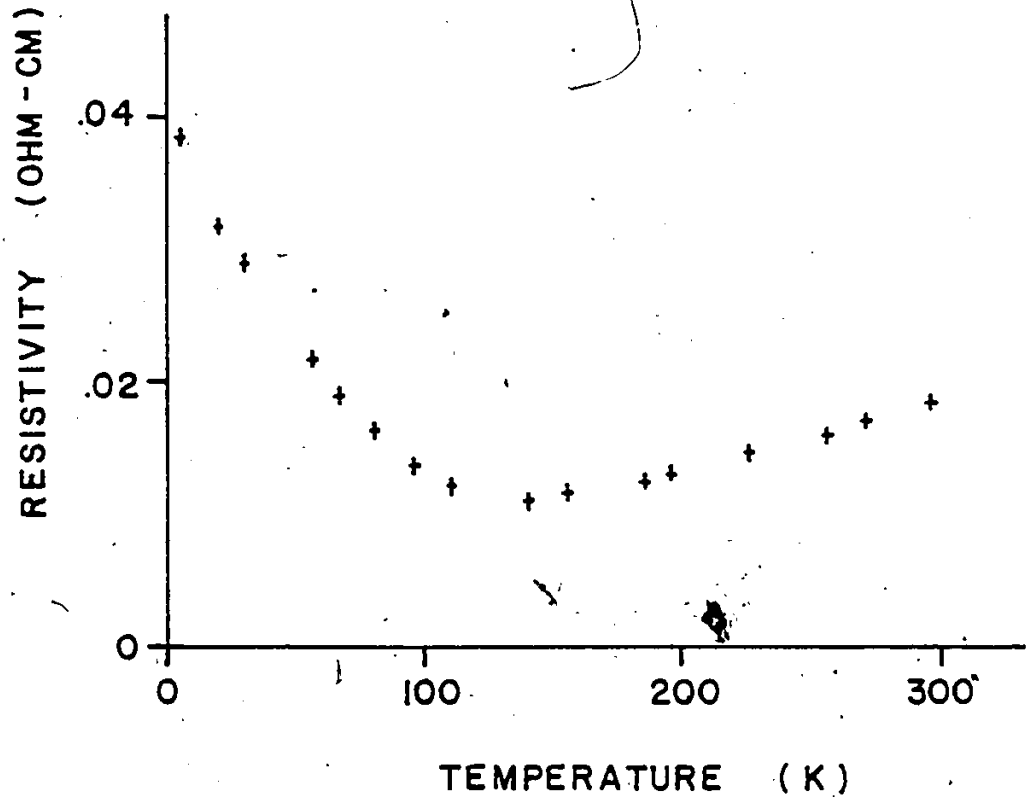

Figure 5-3. Resistivity as a function of temperature for $LaTiO_3$.

of the Kondo effect. This effect exists in some materials as a result of the scattering of conduction electrons at low temperatures by impurities with localized magnetic moments. This gives rise to an increase in the resistivity at low temperatures and creates a resistivity minimum. However, the Kondo effect can be ruled out as a possibility for $LaTiO_3$ for several reasons. Materials which show the Kondo effect typically have minima below 10 K,[64,65] but in some cases as high as 30 K.[66] At temperatures higher than this, the phonon contribution to the resistivity of metals dominates[67] and Kondo minima are not observed. More important than the position of the minimum for the $LaTiO_3$, however, is the experimental observation that there is some magnetic order in the sample below 130 K. This eliminates the possibility of a Kondo effect, as magnetic ordering and the Kondo effect cannot simultaneously exist in a material.[64,67]

The transport data for $LaTiO_3$ can be successfully analyzed in terms of a semiconductor which has a narrow bandgap. For such a material, at low temperatures where k_BT is less than the bandgap (k_B = Boltzmann's constant), the resistivity should increase with decreasing temperature in the manner of a "normal" semiconductor, as it appears to do for $LaTiO_3$. As the temperature increases and k_BT becomes comparable to or greater than the bandgap, the concentration of electrons in the conduction band becomes greater. A semiconductor is said to become degenerate at

temperatures where the Fermi level lies above the bottom of the conduction band.[68] The carrier concentration then becomes essentially independent of temperature, and conduction is much like that of a metal.[69] This behaviour is observed in $LaTiO_3$ for temperatures above 130 K. Resistivity versus temperature curves for degenerate semiconductors look remarkably similar to that for $LaTiO_3$. The undoped Bi-Sb alloy containing 18% Sb, for example, is a very narrow bandgap semiconductor (E_g = 0.005 eV) with a resistivity curve which can be nearly super-imposed on that of $LaTiO_3$.[70] The magnitude of the bandgap in such materials is best estimated by assuming that the resistivity in the low temperature region follows an exponential law:

$$\rho = \rho_o \exp[E_g/2k_BT] \qquad (5\text{-}2)$$

where ρ_o is a constant and E_g is the bandgap. Figure 5-4 shows a graph of the logarithm of the resistivity versus reciprocal temperature for the $LaTiO_3$ data below 130 K. The linear relationship over much of the temperature range strongly suggests that $LaTiO_3$ is a semiconductor. The linear data, analyzed after equation (5-2), reveal that Eg = .008 eV. Notice that the data points at low temperatures fall away from the linear extrapolation. This may result from impurity band conduction,[10] which occurs at low temperatures when electrons tunnel from one impurity site to another. This can occur because the wave functions of electrons (or holes) bound to impurity sites have considerable spatial extent,

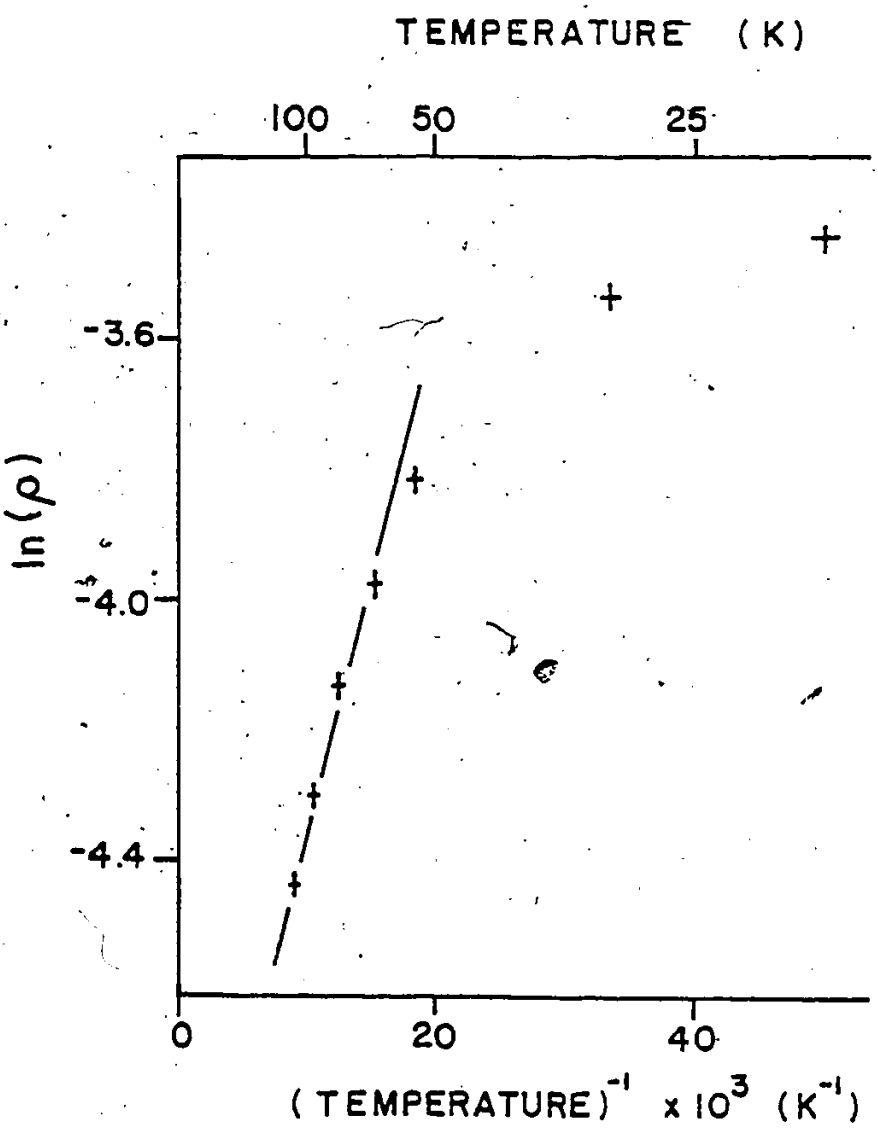

Figure 5-4. Natural logarithm of the resistivity (in ohm-cm) versus reciprocal temperature for $LaTiO_3$.

and the overlap of wave functions at different impurity sites is possible even at fairly low concentrations. Recall that the concentration of foreign impurities in these materials was found to be quite low by emission spectroscopy (< 100 ppm). However, other impurity sites may exist as defects introduced via non-stoichiometry. For example, to account for the thermal gravimetric analysis data, it was postulated that Ti^{+4} ions may exist in the samples. These can act as electron acceptors, and may be present at the level of $\sim$ 1%.

One can well ask the question at this point, "How can $LaTiO_3$ be a semiconductor?" This material has only one Ti^{+3} d-electron per formula unit, while, according to band theory, an <u>even</u> number of electrons are required in order to have a semiconductor. The reason why $LaTiO_3$ could be a semiconductor is that one must consider not just the number of electrons per formula unit, rather the number of electrons per unit cell. Recall from Chapter 3 that $LaTiO_3$ belongs to space group Pbnm, for which there are four formula units per unit cell. This means that for the band structure of $LaTiO_3$, there are four Ti^{+3} d-electrons to be considered, and it is possible that a filled band (semiconductor) situation could result.

This model, then, successfully accounts for the low temperature semiconducting behaviour of $LaTiO_3$ and the presence of a resistivity minimum as the material

assumes a metallic conductivity for $k_BT > E_g$. It also predicts Pauli paramagnetic behaviour at those temperatures where the material shows a metallic conductivity. It is more difficult, though, to account for the onset of ferromagnetism at 130 K.

The low moment observed for the weak ferromagnetism in $LaTiO_3$ may lead one to suspect impurities in the sample. Recall, however, that the starting materials were of high purity (La_2O_3, 99.99%; TiO_2, 99.95%) and that emission spectrographic analysis revealed no foreign impurities at concentrations greater than one hundred parts per million. As well, the possibility of heavy rare earth impurities being responsible for this magnetic ordering at 130 K is excluded as recent studies[71] have shown that they order at temperatures below 65 K. Also recall that Bazeuv et al. report the onset of weak ferromagnetism at approximately the same temperature for a sample of $LaTiO_3$ prepared in the Ural Mountains of Russia. It is also not uncommon to observe weak ferromagnetism in compounds very similar to $LaTiO_3$. For example, the cubic perovskite $SrVO_3$, which is a d^1 system, shows a weak ferromagnetism (T_c = 85 K) giving a saturation moment of .007 μ_B- molecule^{-1} at 4.2 K.[72] The perovskite $CaCrO_3$, isostructural with $LaTiO_3$, shows a transition from Pauli paramagnetism to weak ferromagnetism (T_c = 90 K) which gives rise to a saturation moment of .007 μ_B- molecule^{-1}.[73] The latter case is reported to be

an example of an itinerent electron antiferromagnet in which the weak ferromagnetism results from antisymmetric exchange interactions. In the former case, the ferromagnetism is ascribed to a ferromagnetic spin density wave.

If $LaTiO_3$ is a narrow bandgap semiconductor, then the fact that the onset of magnet ordering occurs at about the same temperature as the minimum in the resistivity curve is accidental. An alternate possibility that should be considered is that at $\sim$ 130 K, a metal-semiconductor transition takes place as a consequence of antiferromagnetic ordering of the itinerant Ti^{+3} d-electrons.

How this can occur is most easily understood in one dimension. If antiferromagnetism occurs in a one dimensional chain, the periodicity of the overall potential is now doubled. This results in any given band being split in half, with the intervening gap being proportional to the strength of the magnetic interaction.[74] This is shown schematically in Figure 5-5, where the effect of antiferromagnetic ordering on a band which is originally half-filled is shown. In such a case, a transition from a metal to a semiconductor would result. $LaTiO_3$ may be considered in this model if one assumes that the distortions from the cubic perovskite are not large enough to alter significantly the energy level structure from that of the cubic analogue. Under this assumption, the single delocalized d-electron per Ti^{+3} may half-fill a band, since the minimum number of electrons

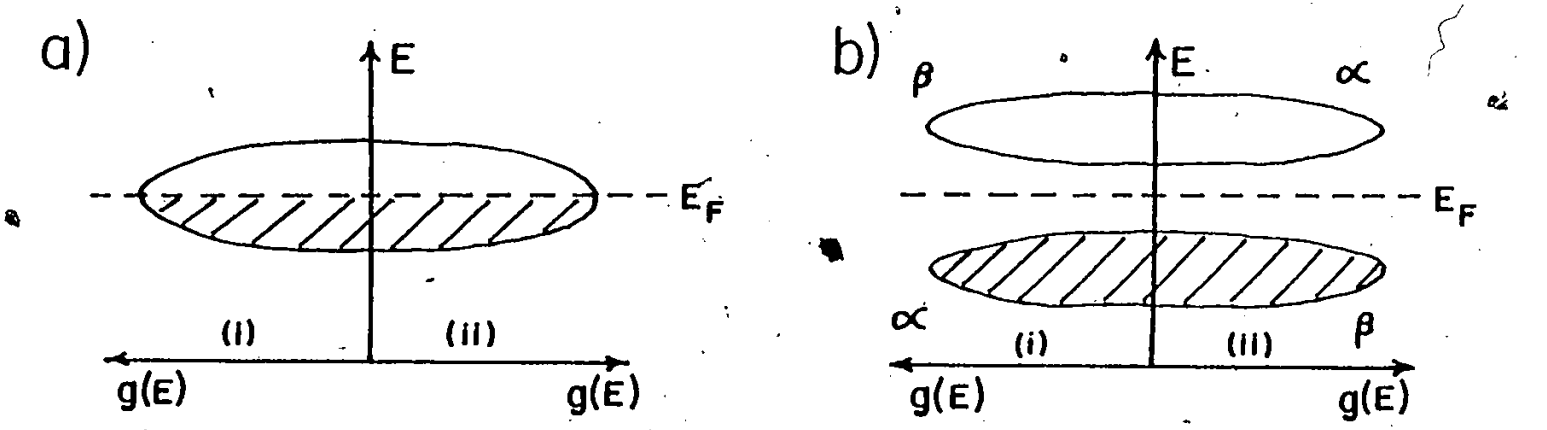

Figure 5-5 Metal-semiconductor transition as a result of antiferromagnetic ordering. Figure 5-5(a) schematically shows a density of states curve as a function of energy above the Néel temperature for a half-filled band situation. The curve is divided into two parts, (i) and (ii), each corresponding to one sublattice of the antiferromagnetic state. Within each sublattice, the energies of states of α and β spin are degenerate. States are filled to the Fermi energy, and the presence of empty states at E_F results in a metal. Upon antiferromagnetic ordering, the energies of α and β states split in each sublattice, and may create a bandgap as shown in Figure 5-5(b). Filling states to the Fermi energy now results in a semiconductor.

required to fill a band is two. At high temperatures (> 130 K), $LaTiO_3$ would be a metal. Antiferromagnetic ordering at ∿ 130 K could then split that half-filled band, as in Figure 5-5, causing the material to become a semiconductor at lower temperatures. Such a model for $LaTiO_3$ accounts for the fact that the appearance of magnetic ordering and semiconducting resistivity occur at the same temperature. The weak ferromagnetism would have to result from a mechanism such as antisymmetric exchange in the itinerant antiferromagnetism, as is postulated in $CaCrO_3$.[73]

The results of the infrared investigation of single crystal $LaTiO_3$ are consistent with the observation of semiconducting behaviour for $LaTiO_3$ below 130 K. For that experiment (done at 1.2 K), no radiation was transmitted to the detector. The minimum energy of the incident radiation (∿ .005 eV) is quite close to the estimated semiconductor bandgap (∿ .008 eV), so that transmitted radiation, if any, would have to come from only the lowest energy fraction of the incident beam. The presence of any impurity levels in the bandgap region can then absorb even these low energy photons.

The magnetic and transport properties of $CeTiO_3$ are in many ways similar to those of $LaTiO_3$. Figure 5-6 shows the transport behaviour of $CeTiO_3$ as a function of temperature. For temperatures above ∿ 60 K, the resistivity increases with increasing temperature, indicating

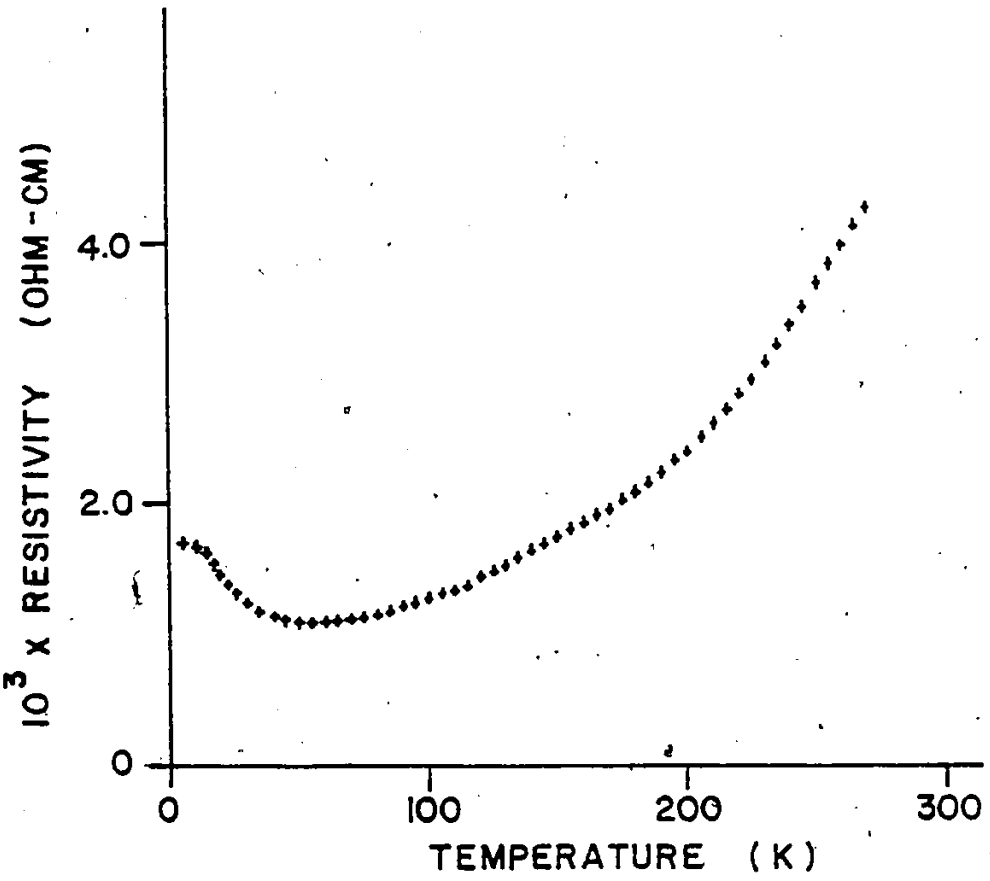

Figure 5-6. Resistivity versus temperature for $CeTiO_3$.

metallic behaviour. For temperatures below ~ 60 K, the resistivity increases with decreasing temperature, creating a resistivity minimum. The data below 60 K may be analyzed in terms of a semiconductor model as was done for $LaTiO_3$. Figure 5-7 shows a plot of the logarithm of the resistivity versus reciprocal temperature for these data. The linear portion of this curve is analyzed according to equation (5-2) and gives an activation energy of .001 eV. The very low temperature data falling away from the linear extrapolation may be accounted for by impurity band conduction, as in $LaTiO_3$. Thus, the behaviour of the resistivity over the entire temperature range investigated may be described by a degenerate semiconductor model, as was the case for $LaTiO_3$. These transport data, then, suggest delocalized d-electron behaviour for $CeTiO_3$.

The magnetic behaviour of $CeTiO_3$ is equally fascinating as that for $LaTiO_3$. Figure 5-8 includes both raw and analyzed susceptibility data for $CeTiO_3$, for temperatures above 115 K, plotted as reciprocal susceptibility versus temperature. Notice that the raw data (Figure 5-8(a)) are not linear, that is, they do not show a Curie-Weiss law dependence:

$$\chi_M = C_M/(T-\theta_c). \qquad (5\text{-}3)$$

However, the data do show a susceptibility-temperature dependence of the form

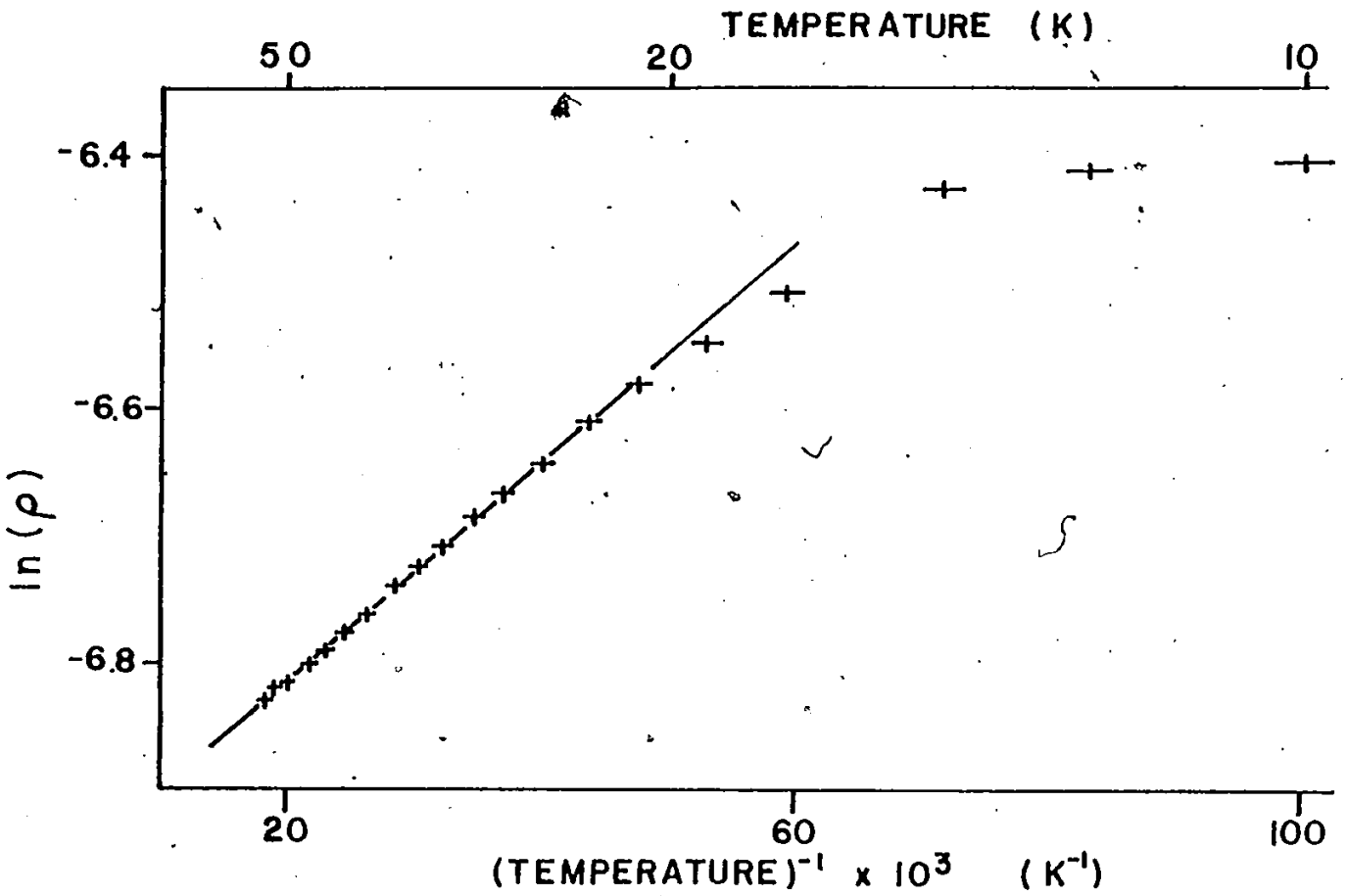

Figure 5-7 Natural logarithm of the resistivity (in ohm-cm) versus reciprocal temperature for $CeTiO_3$.

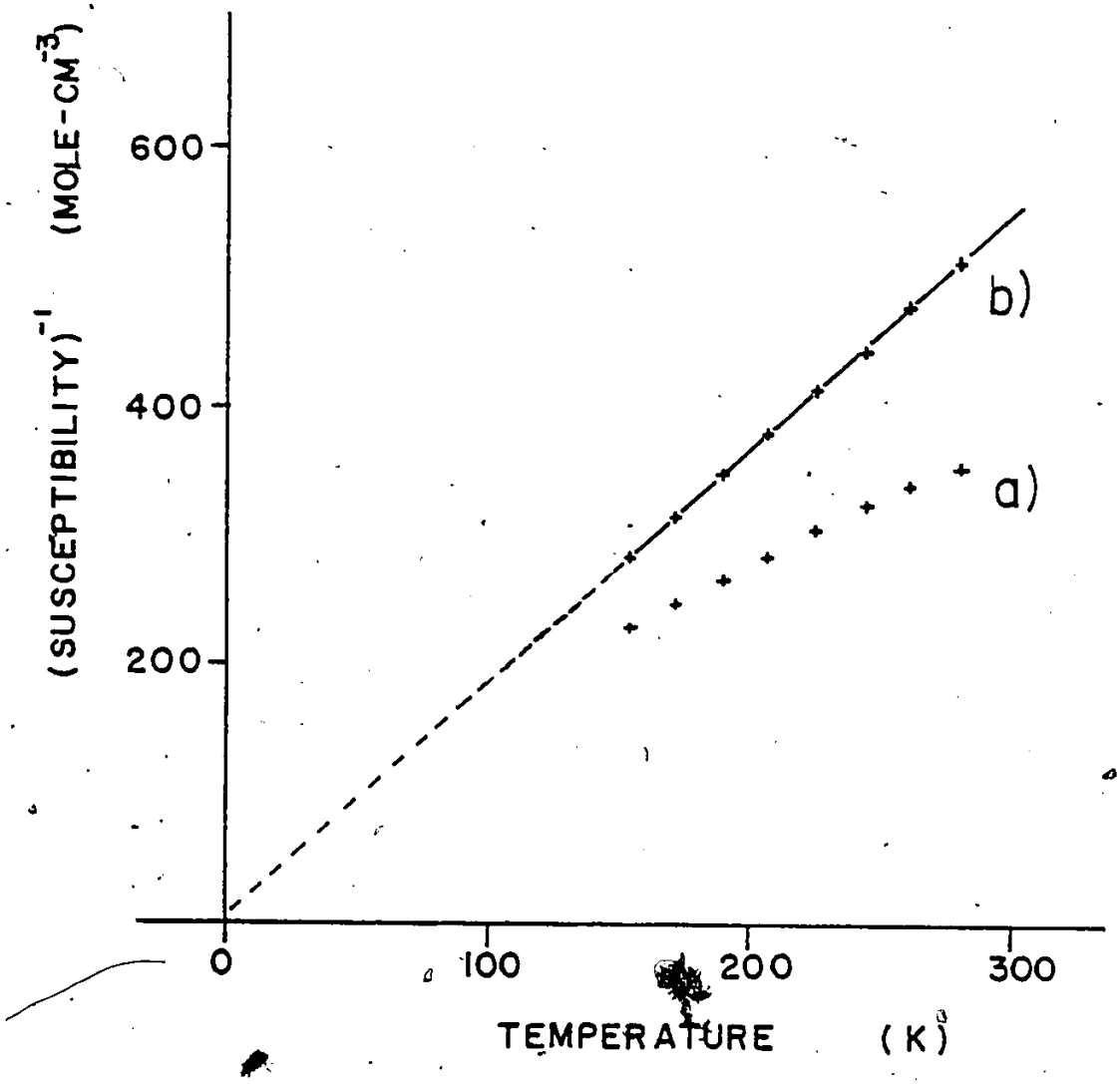

Figure 5-8. Raw (a) and analyzed (b) reciprocal molar susceptibility versus temperature for $CeTiO_3$.

$$\chi_M = C_M/(T-\theta_c) + \chi_{T.I.P.} \qquad (5-4)$$

where $\chi_{T.I.P.}$ is a temperature independent term. The best linear fit of $(\chi_M')^{-1}$ vs T where $\chi_M' = \chi_M - \chi_{T.I.P.}$ is shown in Figure 5-8(b) for which $\chi_{T.I.P.} = (860 \pm 10)\times10^{-6}$ cm^3 mole^{-1}, $C_M = 0.55 \pm 0.03$ cm^3-K-mole^{-1}, and $\theta_c = -5 \pm 3$ K (yielding a correlation coefficient of 0.99994). These findings differ from the work of Bazuev et al.,[54] who report a linear χ^{-1}-T dependence and a larger C_M.

The magnitude of the temperature independent term is quite close to that found for the Pauli susceptibility of $LaTiO_3$ ($(800 \pm 20)\times10^{-6}$ cm^3 mole^{-1}), and together with the resistivity data in this temperature range, the temperature independent term may be attributed to a Pauli susceptibility for delocalized d-electrons in $CeTiO_3$. The remaining Curie-Weiss susceptibility then is due to the localized f-electrons of Ce^{+3}. The observed molar Curie constant, C_M, is reduced from the free ion Curie constant of 0.80 cm^3 mole^{-1} K^{-1}, as is observed in other perovskite-type cerium oxides.[75,76]

The magnetic behaviour of $CeTiO_3$ at lower temperatures is shown in Figures 5-9 and 5-10. In Figure 5-9, the response of the magnetization to applied field is shown at various temperatures. The data for T = 4.2 K to T = 90 K indicate that the material is magnetically ordered at those temperatures, while the data for T = 130 K show paramagnetic

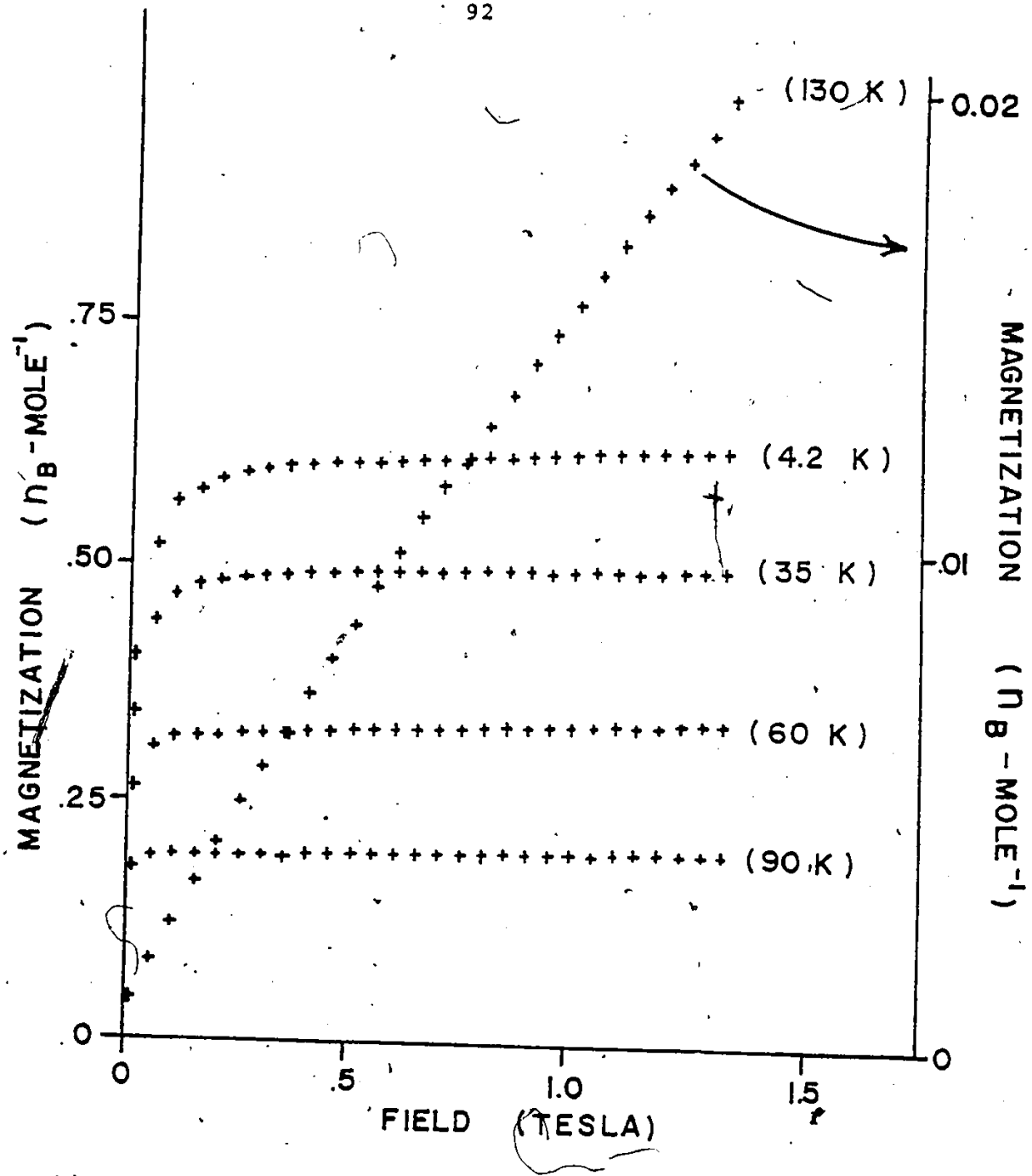

Figure 5-9. Magnetization versus field for $CeTiO_3$. The temperatures at which the field runs were taken are shown in brackets.

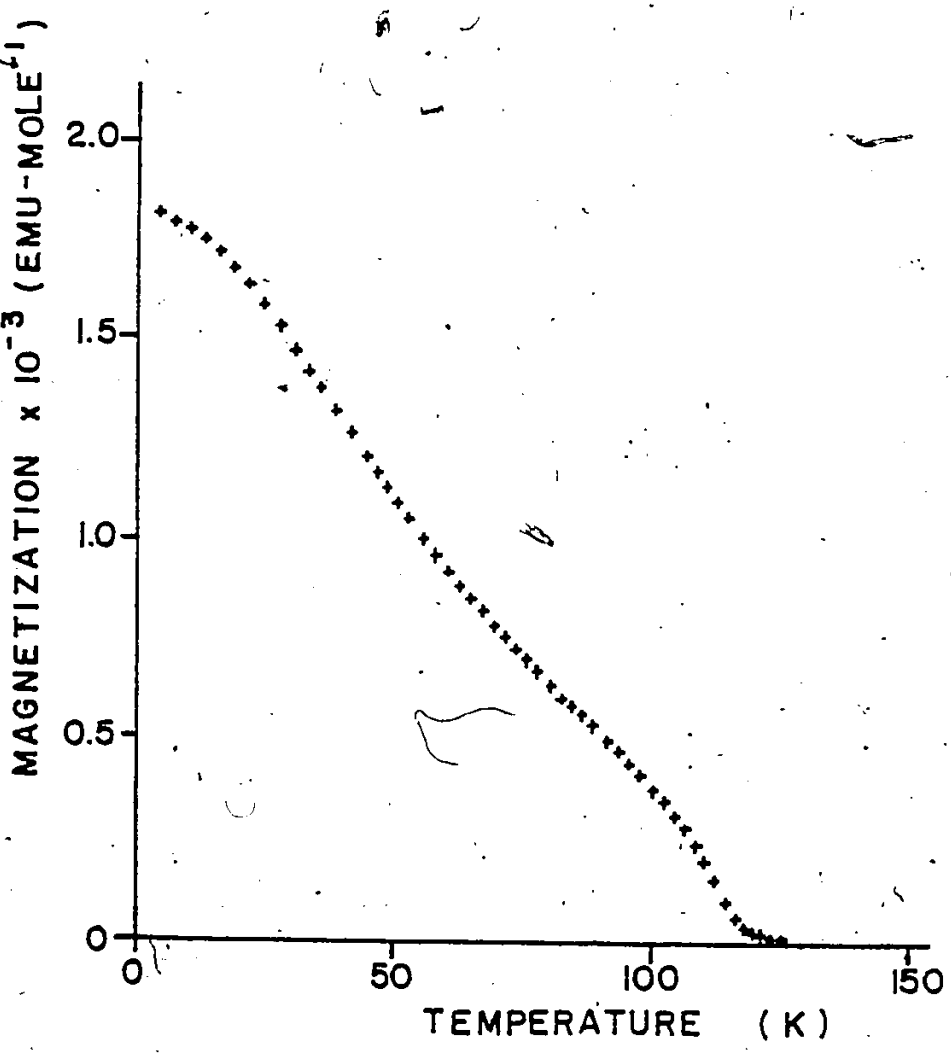

Figure 5-10. Magnetization versus temperature for $CeTiO_3$ at an applied field of 0.0045 Tesla.

behaviour. Figure 5-10 shows the response of the magnetization to temperature at an applied field of 0.0045 T. The slope of this curve is complicated, certainly not Brillouin-like. The undulations may indicate changes in magnetic structure with temperature in the range 50 K to 100 K. There is clearly an ordering temperature at 116 ± 2 K. Note that the temperature at which the minimum in the resistivity occurs (60 K) does not coincide with the temperature of the high temperature magnetic transition in $CeTiO_3$, unlike the case for $LaTiO_3$. It is of interest to note that a close examination of the susceptibility data for $CeTiO_3$ in Figure 5-10 does suggest that there may be an inflection around 60 K.

The nature of the magnetic ordering in $CeTiO_3$ is unclear. The Ce^{+3} f-electrons may be ordering by an indirect exchange mechanism, that is, involving the itinerant Ti^{+3} d-electrons. There may also be spontaneous magnetism in the Ti^{+3} d-band. The saturation magnetization of ~ 0.6 μ_B- molecule^{-1} at 4.2 K suggests that the magnetic structure may be complicated, as the ferromagnetic saturation moment for the Ce^{+3} f-electron is 2.1 μ_B, while simple antiferromagnetic ordering of the Ce^{+3} ions would show no magnetization and one would expect to observe only a small moment from the Ti^{+3} d-electrons as in $LaTiO_3$. A saturation moment of 0.6 μ_B- mole^{-1} is thus not easily explained.

These magnetic data observed for $CeTiO_3$ are in reasonable agreement with those reported by Bazuev et al.[54] in their studies down to 80 K. Their explanation, based on canted antiferromagnetic ordering of localized d-electrons giving rise to the weak ferromagnetism, is not consistent with the transport behaviour reported herein, which indicates that the Ti^{+3} d-electrons are delocalized above 116 K. The transport data reported here for $CeTiO_3$ are not in agreement with those of Bazuev et al.,[26] who report that the resistivity is independent of temperature.

5.3 $PrTiO_3$ and $NdTiO_3$

Figure 5-11 shows the response of the molar susceptibility to temperature for $PrTiO_3$ at temperatures above 100 K. These data can be analyzed according to the Curie-Weiss law (equation (5-3)) with C_M = 1.73 cm^3-K-$mole^{-1}$ and θ = -49 K. There is no evidence for a temperature independent paramagnetic term in the susceptibility, as was found for $LaTiO_3$ and $CeTiO_3$. The observed Curie constant is greater than that expected for free ion Pr^{+3} only (1.60 cm^3-K-$mole^{-1}$) and suggests that there is a contribution from Ti^{+3}. This, in turn, suggests that the d-electrons of Ti^{+3} are localized on atomic sites giving rise to local moments and a contribution to the Curie constant (the spin-only Curie constant for Ti^{+3} is 0.37 cm^3-K-$mole^{-1}$). The Curie constant for Pr^{+3} in $PrTiTaO_6$, in which the

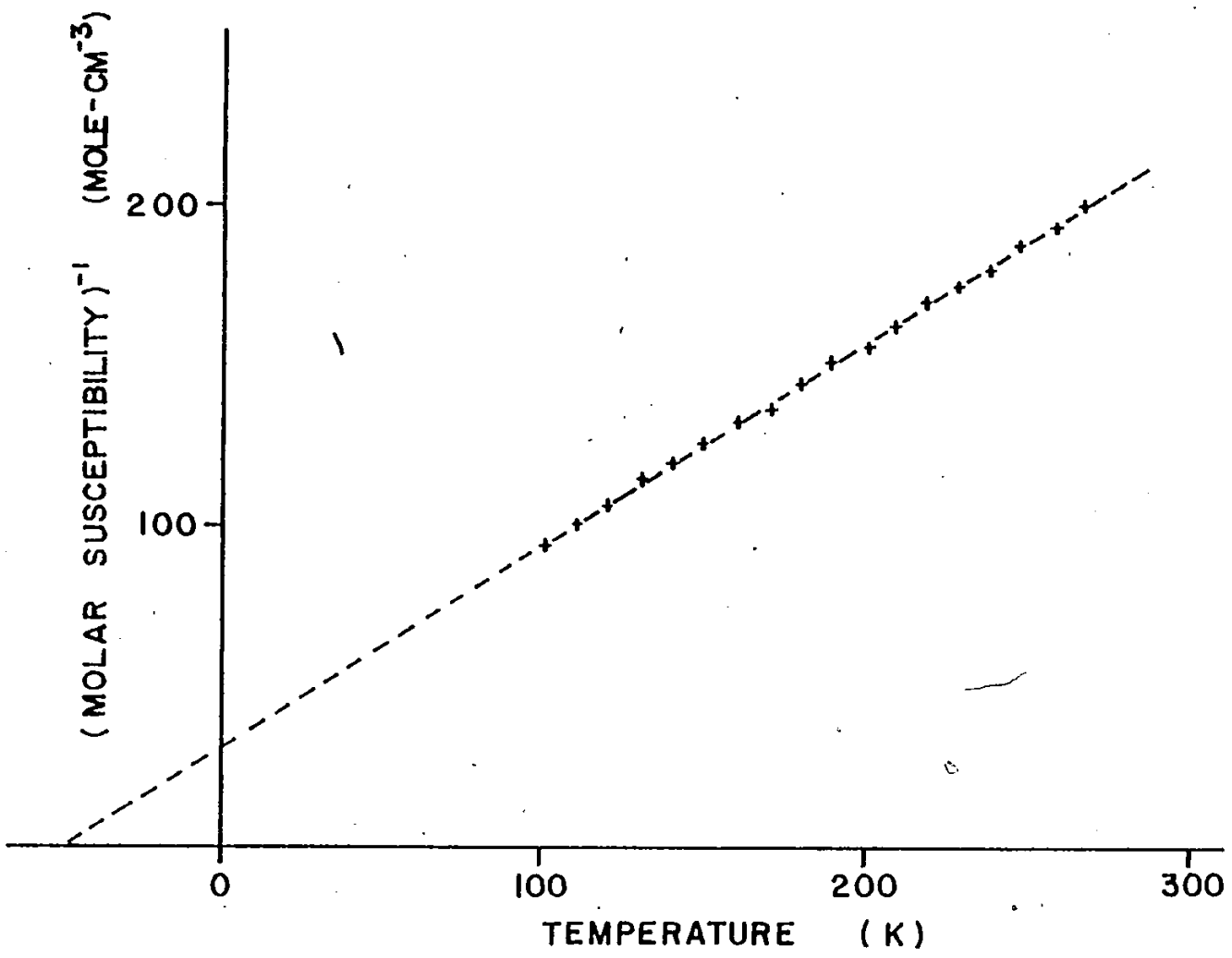

Figure 5-11 Inverse susceptibility versus temperature for $PrTiO_3$ at 1.08T.

environment around the rare earth is similar to that in the titanites, is 1.28 cm^3-K-$mole^{-1}$.[78] Assuming a similar reduction from the free ion Curie constant of Pr^{+3} in the titanites, there would have to be a significant contribution to the observed Curie constant from Ti^{+3}.

The lowest curve of Figure 5-12 shows the response of the magnetization to temperature for $PrTiO_3$ at an applied field of 0.0045 T. It is clear that magnetic ordering of some kind occurs at a critical temperature T_c = 96 ± 2 K. The nature of this magnetic ordering is unclear. Figure 5-13 shows the magnetization versus field data for $PrTiO_3$ at 4.2 K. The data indicate that the magnetization saturates to ~ 0.5 μ_B- molecule, but there appears to be some field dependence to the saturation moment, perhaps due to a paramagnetic contribution. The data in Figure 5-12 show the remarkable response of the magnetization to temperature at various applied fields. Notice that as the applied field increases, a "hump" appears in the data, its position shifting to lower temperatures. The cause of this effect is unclear. It may be that the application of a magnetic field is causing a change in the magnetic structure of $PrTiO_3$ and consequently, different responses of the magnetization to temperature.

The results of Bazuev et al.[54] are in reasonable agreement with this work, as they report a magnetic ordering at 90 K. Their interpretation in terms of canted anti-

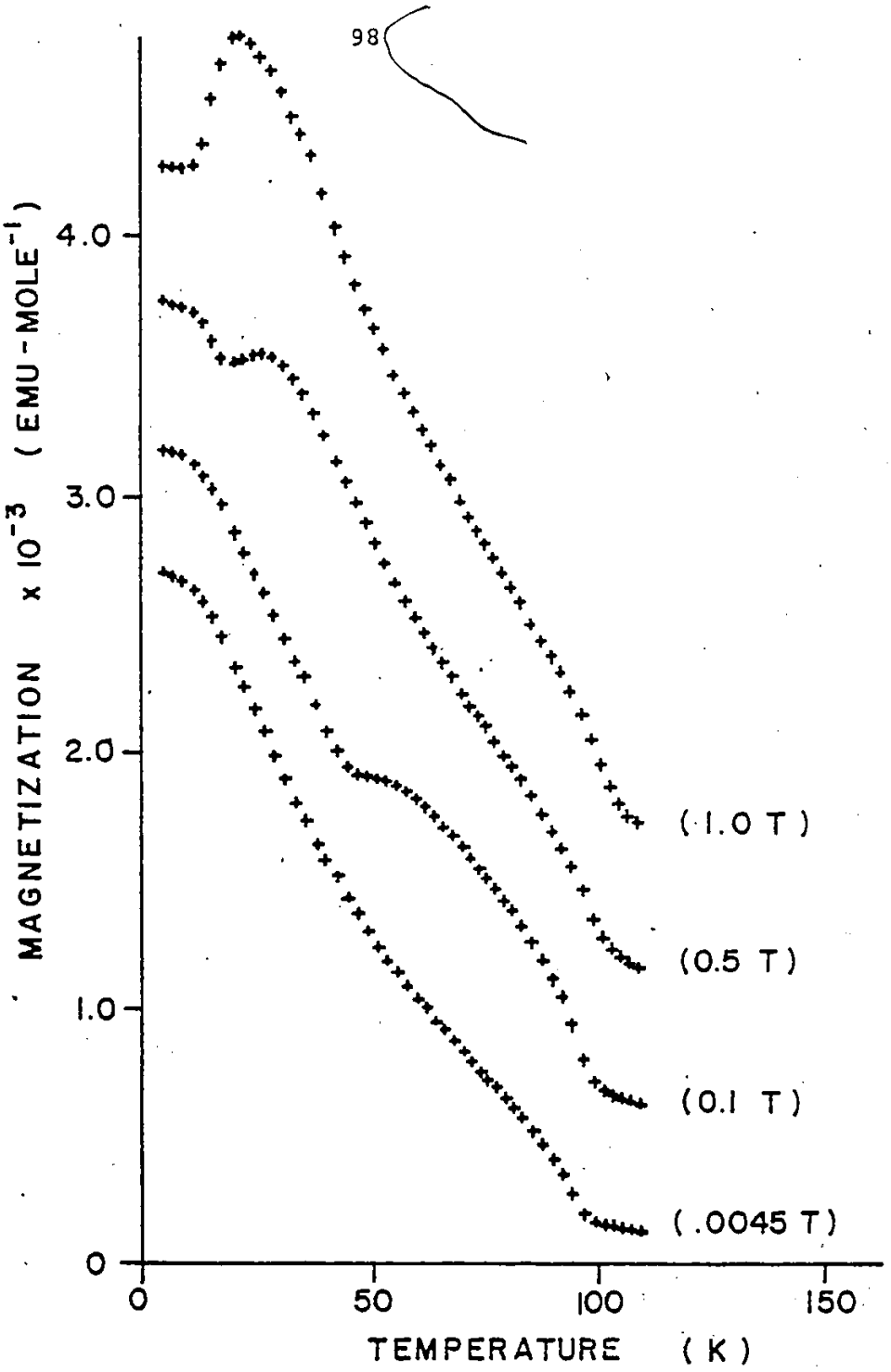

Figure 5-12. Magnetization versus temperature for $PrTiO_3$ at various fields (applied fields indicated in brackets beside the appropriate curve). With increasing field each successive curve has been displaced upwards by 0.5 x 10^{-3} emu-mole^{-1} for clarity.

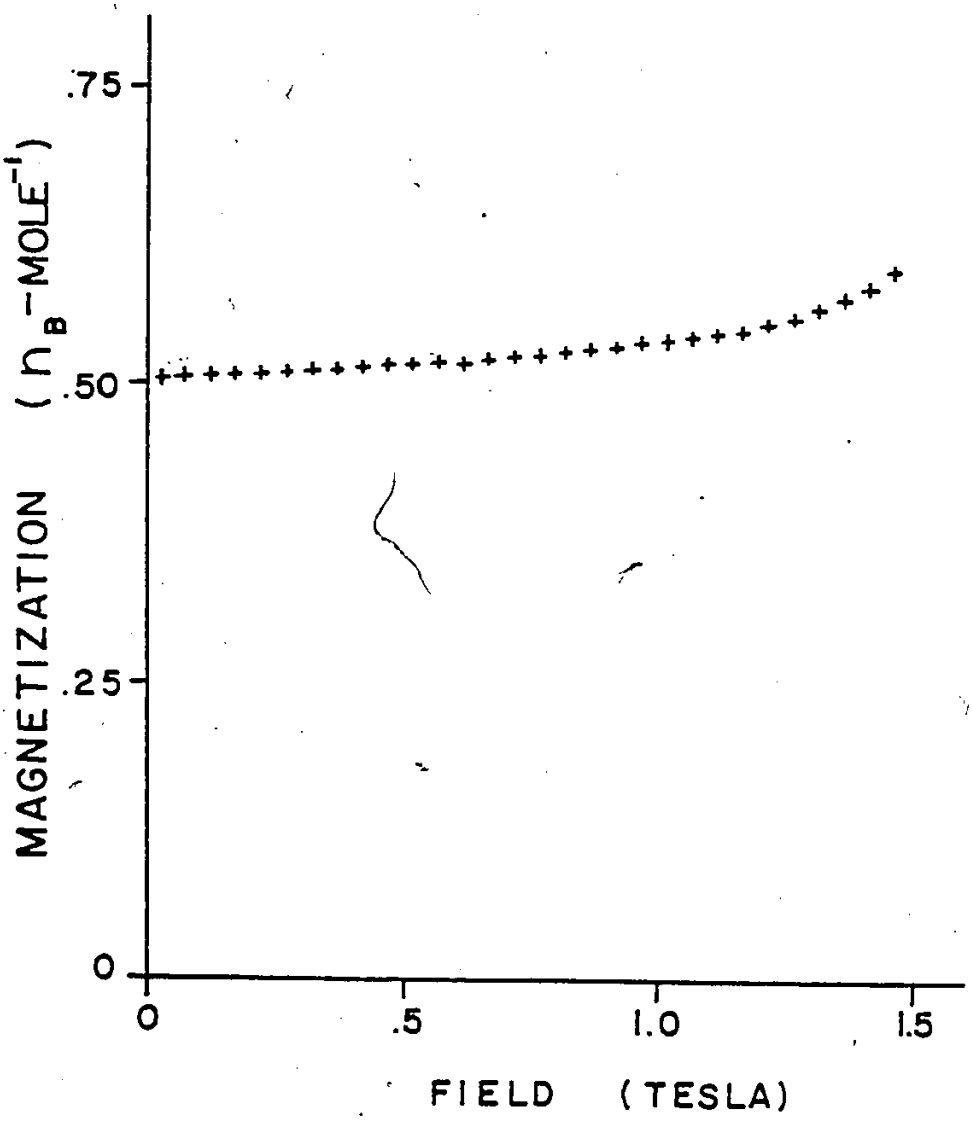

Figure 5-13. Magnetization versus field at 4.2 K for $PrTiO_3$.

ferromagnetic ordering of the Ti^{+3} sublattice is suspicious in light of the high saturation moment at 4.2 K reported in this work. Canted antiferromagnetic ordering of the transition metal sublattice, such as is found in the isostructural $REFeO_3$,[79,80] gives rise to a very weak ferromagnetism on the order of 0.05 μ_B- $mole^{-1}$.

The transport behaviour of $PrTiO_3$ is shown in Figure 5-14, presented as the natural logarithm of the resistivity versus reciprocal temperature. The linear sections of these data suggest that transport occurs via an activated mechanism. Assuming that the resistivity follows an exponential law of the form

$$\rho = \rho_o \exp[E_a/k_B T] \qquad (5\text{-}5)$$

the data for $PrTiO_3$ yield the activation energies E_a = .04 eV (high temperature) and .03 eV (low temperature). These findings differ from those of Bazuev et al.[26] who report a resistivity that is independent of temperature (i.e., E_a = 0 eV).

These transport data for $PrTiO_3$ can be explained by assuming that the material is a "normal" band semiconductor like silicon or germanium. However, in light of the preceding magnetic data, it is more probable that the Ti^{+3} d-electron is localized on atomic sites. If this is the case, a band picture should not be used to account for the activated transport behaviour. Rather, one should consider the

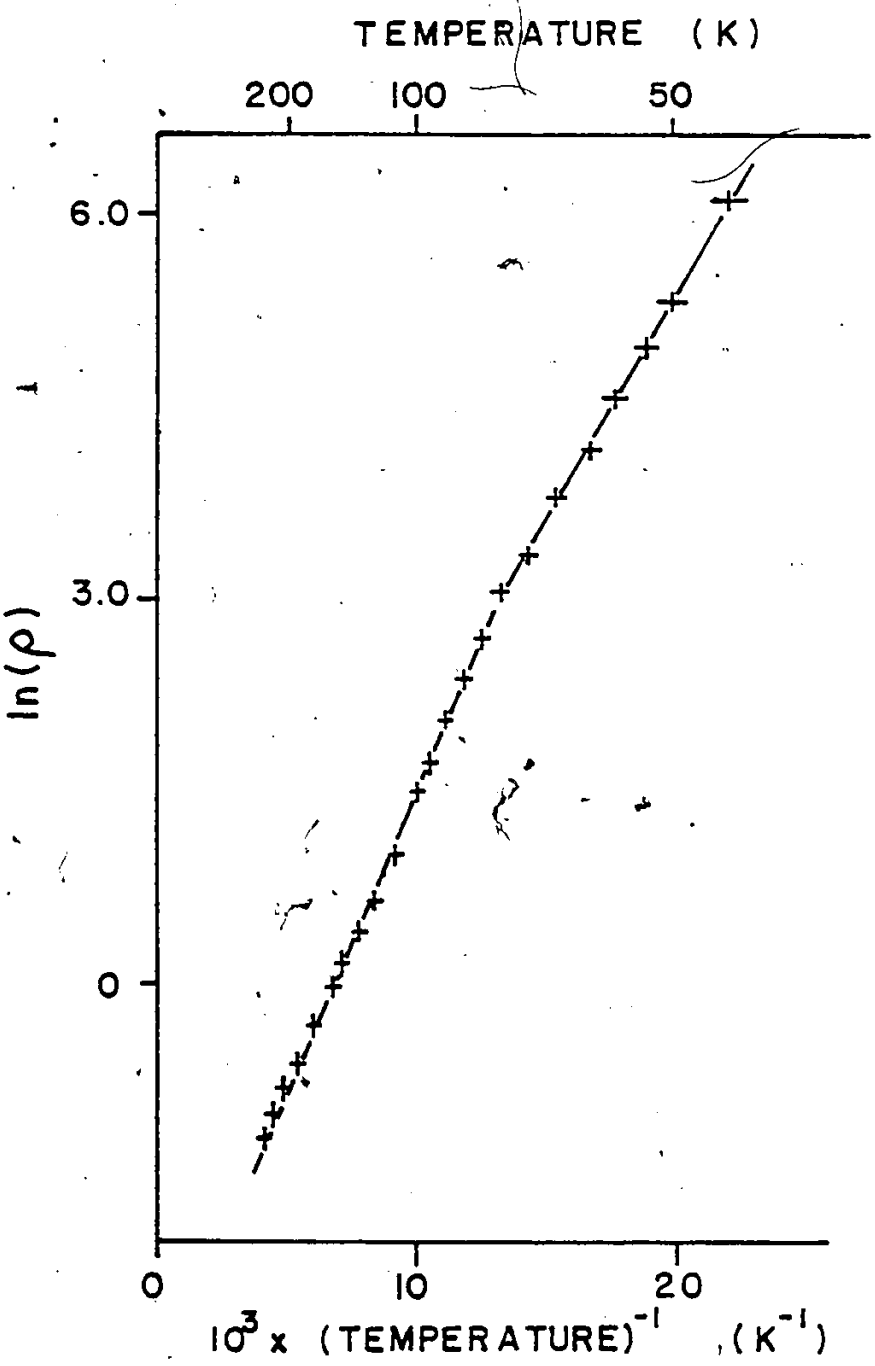

Figure 5-14. Natural logarithm of the resistivity (in ohm-cm) versus reciprocal temperature for $PrTiO_3$.

activated transport to be a consequence of small polaron conduction. Some aspects of this conduction process have been discussed in Chapter 1. Small polaron theory has been extensively applied to semiconducting transition metal oxides[13,81] where the d-electrons are thought to "hop" from one metal ion to another via the 2p orbitals of the oxygen ions. Examples are the movement of Ni^{+3} centres through NiO, Ti^{+3} through TiO_2 and Ce^{+3} through CeO_2.[82] As discussed in Chapter 1, the small polaron model predicts an activated resistivity. At very low temperatures, there is also the possibility of band conduction via quantum mechanical tunnelling through the potential wells between metal ions.[2] This should not be a significant problem over the temperature range studied for $PrTiO_3$. The activated transport observed for $PrTiO_3$, then, is consistent with localized d-electrons on Ti^{+3} and small polaron conduction.

$PrTiO_3$ shows a higher E_a at temperatures above 75 K than it does below that temperature. This behaviour is not uncommon in systems which undergo transport by a small polaron mechanism, and is seen, for example, in the reduced CeO_2 phases.[82] E_a's observed at low temperatures are often due to impurity levels in the sample.

The inverse molar susceptibility of $NdTiO_3$ as a function of temperature is shown in Figure 5-15. The data show a Curie-Weiss behaviour, and analysis after equation (5-3)

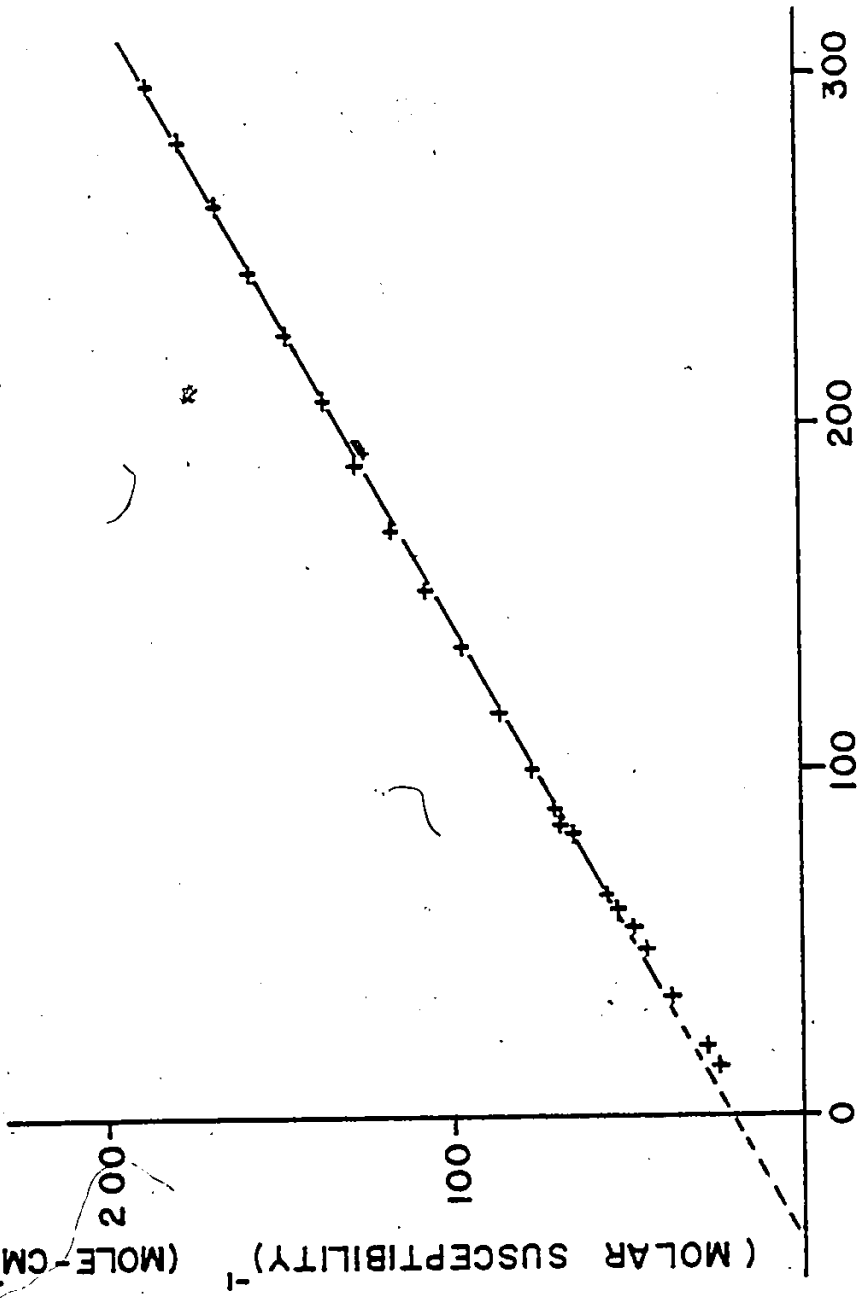

Figure 5-15 Reciprocal susceptibility versus temperature for $NdTiO_3$ at 1.08T.

yields a Curie constant, C_M = 1.77 cm^3-K-$mole^{-1}$ and θ = -35 K. Data collected down to 1.2 K showed no evidence for magnetic ordering. The negative value for θ presumably arises from crystal field effects, as θ's of a comparable value are found for paramagnetic Nd^{+3} ions in similar environments (i.e., $NdTiTaO_6$, θ = -30 K).[78]

The Curie constant observed for $NdTiO_3$ is higher than that expected for free ion Nd^{+3} only (1.62 cm^3-K-$mole^{-1}$). In fact, the value of C_M reported for Nd^{+3} in similar oxide systems is substantially reduced from the free ion value. For example, $C_M(Nd^{+3})$ in $NdTiTaO_6$ is 1.36 cm^3-K-$mole^{-1}$,[78] and $C_M(Nd^{+3})$ in $Nd_2Ti_2O_7$ is 1.22 cm^3-K-$mole^{-1}$.[83] So one might expect the contribution of Nd^{+3} in $NdTiO_3$ to the Curie constant to be less than the free ion value. This suggests that there may be a significant contribution from Ti^{+3} ions of the Curie-Weiss type, which in turn suggests localized d-electron behaviour in $NdTiO_3$. These magnetic data are in reasonable agreement with the findings of Bazuev et al.[26] and Ganguly et al.[20] in their studies down to 80 K.

There is a difficulty in the interpretation of the paramagnetic data of $PrTiO_3$ and $NdTiO_3$. That is that the measured Curie constant is contributed to by both Ti^{+3} and the rare earth, and both ions may deviate from the spin-only or free-ion value. It is, therefore, difficult to derive a value for the Ti^{+3} moment.

The transport behaviour of $NdTiO_3$ is shown in Figure 5-16 as the natural logarithm of the resistivity versus reciprocal temperature. The linear relationship may be analyzed in terms of an activated resistivity after equation (5-5) giving E_a = 0.030 eV. Bazuev et al.[26] and Ganguly et al.[20] report behavior similar to this, the former group finding E_a = 0.06 eV and the latter group finding E_a = 0.02 eV. As was the case for $PrTiO_3$, the magnetic evidence for localized electron behaviour suggests that E_a could be interpreted as an activation energy for small polaron conduction.

The result of the low temperature (1.2 K) infrared investigation of a single crystal of $NdTiO_3$ was that no radiation was detected as being transmitted through the sample. This result may at first appear to be a disappointment as one might expect to find some transparency in the infrared below 0.030 eV, the activation energy found from transport studies. However, the observed opacity is consistent with the hypothesis that transport in $NdTiO_3$ occurs via a small polaron mechanism. At low temperatures, where $k_BT << E_a$, transport in such systems is no longer activated but may occur via quantum mechanical tunnelling through the potential barriers between ions.[84,85,86] The existence of this tunnelling is coincident with band-like behaviour, and gives rise to a source of optical absorption.

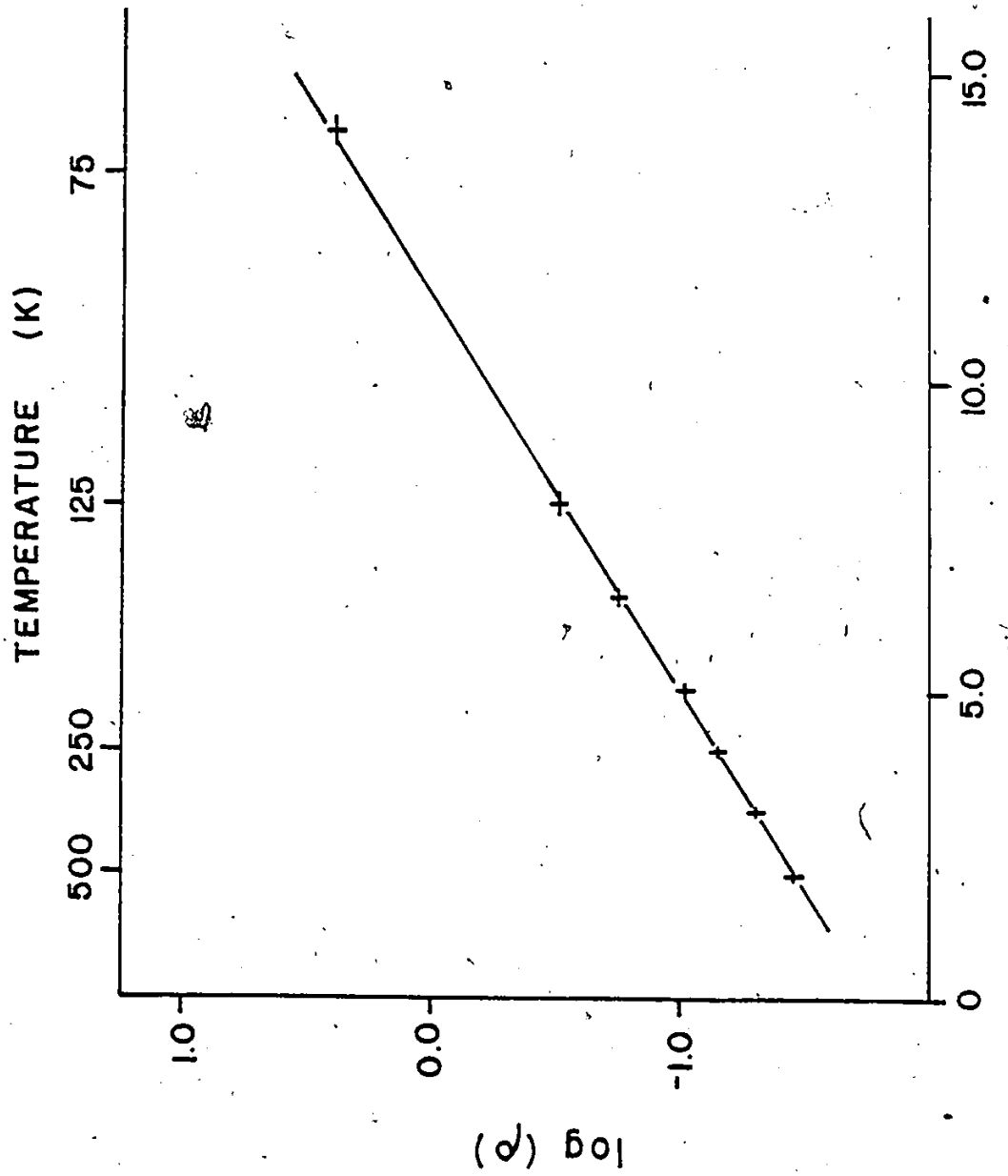

Figure 5-16 Logarithm (to base 10) of the resistivity (in ohm-cm) versus reciprocal temperature for $NdTiO_3$.

This absorption at low temperatures has been studied in the perovskites $BaTiO_3$,[87] and $LaCoO_3$,[88] which undergo transport by small polaron conduction. The minimum absorption coefficient, α, in the infrared for $LaCoO_3$ due to this band-like absorption is $\sim$ 200 cm^{-1}. If one assumes that the relationship

$$I = I_o \exp[-\alpha d] \qquad (5\text{-}6)$$

is valid for absorption in $NdTiO_3$, where I_o is the intensity of the incident radiation, I is the intensity of the transmitted radiation, α is the absorption coefficient and d is the sample thickness, then for the sample used in this experiment (d = 0.0309 cm) one can estimate the fraction of incident radiation transmitted if absorption occurs due to polaron band formation. Using α = 200 cm^{-1} from the isostructural $LaCoO_3$, the result is

$$I/I_o \approx 0.002$$

The equipment used in this experiment can detect a signal only for $I/I_o > \sim 0.01$ in the geometry used.[89] This means that one would not expect to detect a signal for this sample at low temperatures if a small polaron mechanism is operative. The fact that the sample does highly absorb at these temperatures, then, is consistent with the model of localized Ti^{+3} d-electrons and transport via a small polaron mechanism.

5.4 $GdTiO_3$ and $YTiO_3$

The reciprocal susceptibility of $GdTiO_3$ is shown as a function of temperature in Figure 5-17, and the molar magnetization as a function of temperature (at an applied field of 0.0400 T) in Figure 5-18. This magnetic behaviour is typical of a ferrimagnet.[90,9] The data of Figure 5-18 indicate a ferrimagnetic ordering temperature of 34 ± 2 K.

Néel has shown[92] that for a two-sublattice ferrimagnet, the high temperature susceptibility, analyzed as χ^{-1}, is a hyperbola and has expressed it in the form

$$\chi^{-1} = \frac{T-\theta}{C} - 0\frac{\zeta}{T-\theta'} \qquad (5\text{-}7)$$

The high temperature susceptibility of $GdTiO_3$, analyzed after equation (5-7), yields C = 8.12, θ = -4.7 K, ζ = 48.1 and θ' = 40.1 K. The molecular field coefficients, derived from these parameters, are γ_{Ti-Ti} = 10.6, γ_{Gd-Gd} = 3.2 and γ_{Gd-Ti} = -8.1. The constant C is determined from the Curie-Weiss part of the curve and should be equal to $C_{Gd^{+3}} + C_{Ti^{+3}}$ = 8.25. The observed value is slightly reduced from this value, as is also found for $GdCrO_3$.[93] γ_{Ti-Ti} is positive (ferromagnetic) and is considerably larger than the Gd-Gd interaction. γ_{RE-Ti} is intermediate in magnitude and is antiferromagnetic.

Figure 5-19 shows the saturation moment of $GdTiO_3$ as a function of applied field at 1.2 K. These data suggest that the magnetization of $GdTiO_3$ approaches saturation at a value of 6.0 ± 0.1 μ_B-mole^{-1}. As the free ion value for the saturation moment of Gd^{+3} (a $4f^7$ ion) is 7.0 μ_B-ion^{-1} and spin-only value for Ti^{+3} (a $3d^1$ ion) is 1.0 μ_B-ion^{-1}, the data suggest an antiparallel coupling of the Gd^{+3} and Ti^{+3} moments.

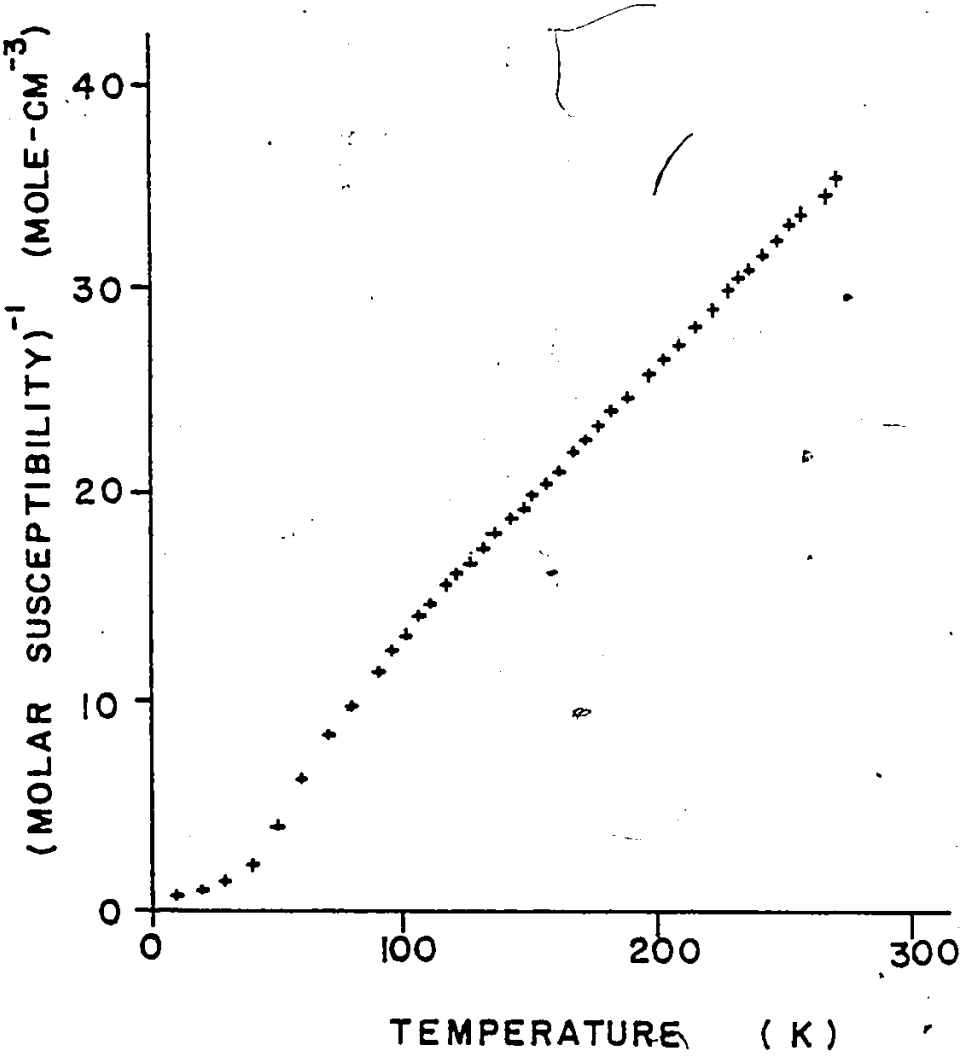

Figure 5-17. Reciprocal susceptibility versus temperature for $GdTiO_3$ at 1.08 T.

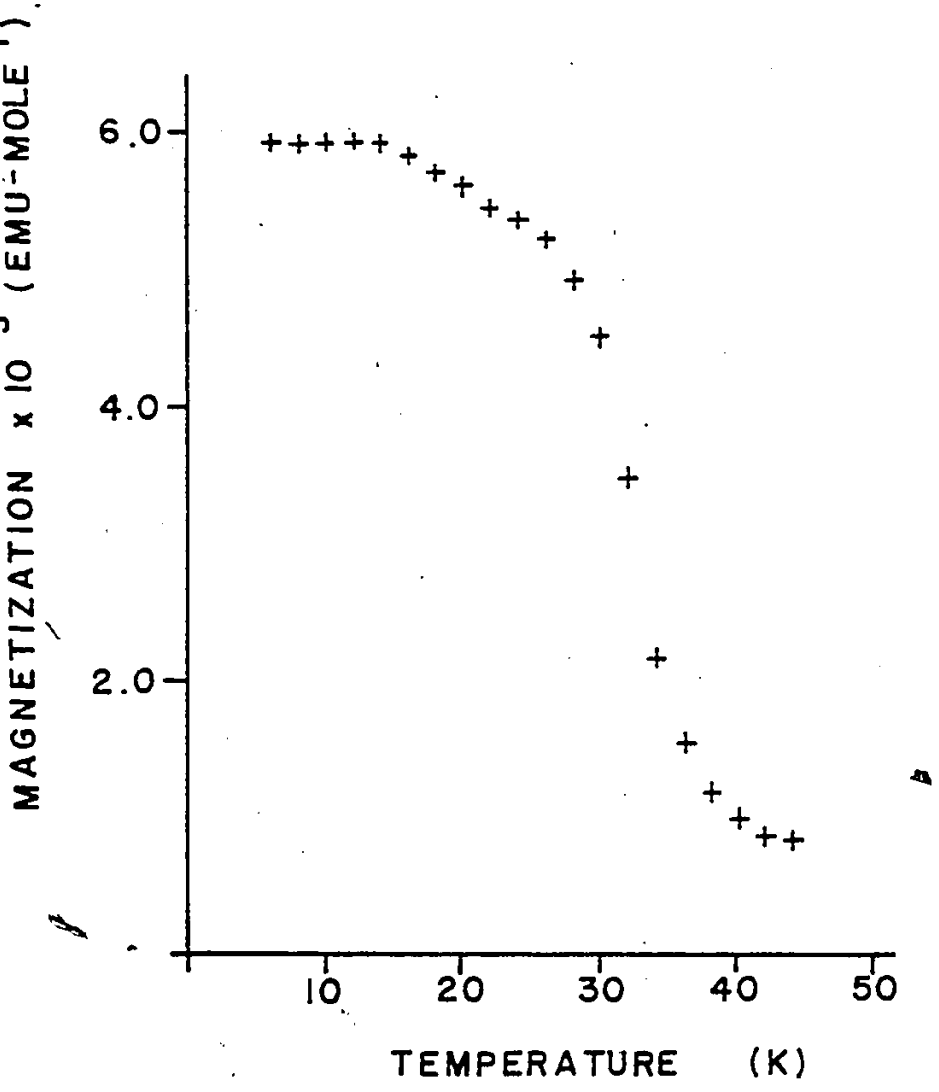

Figure 5-18. Magnetization versus temperature for $GdTiO_3$ at 0.0400 T.

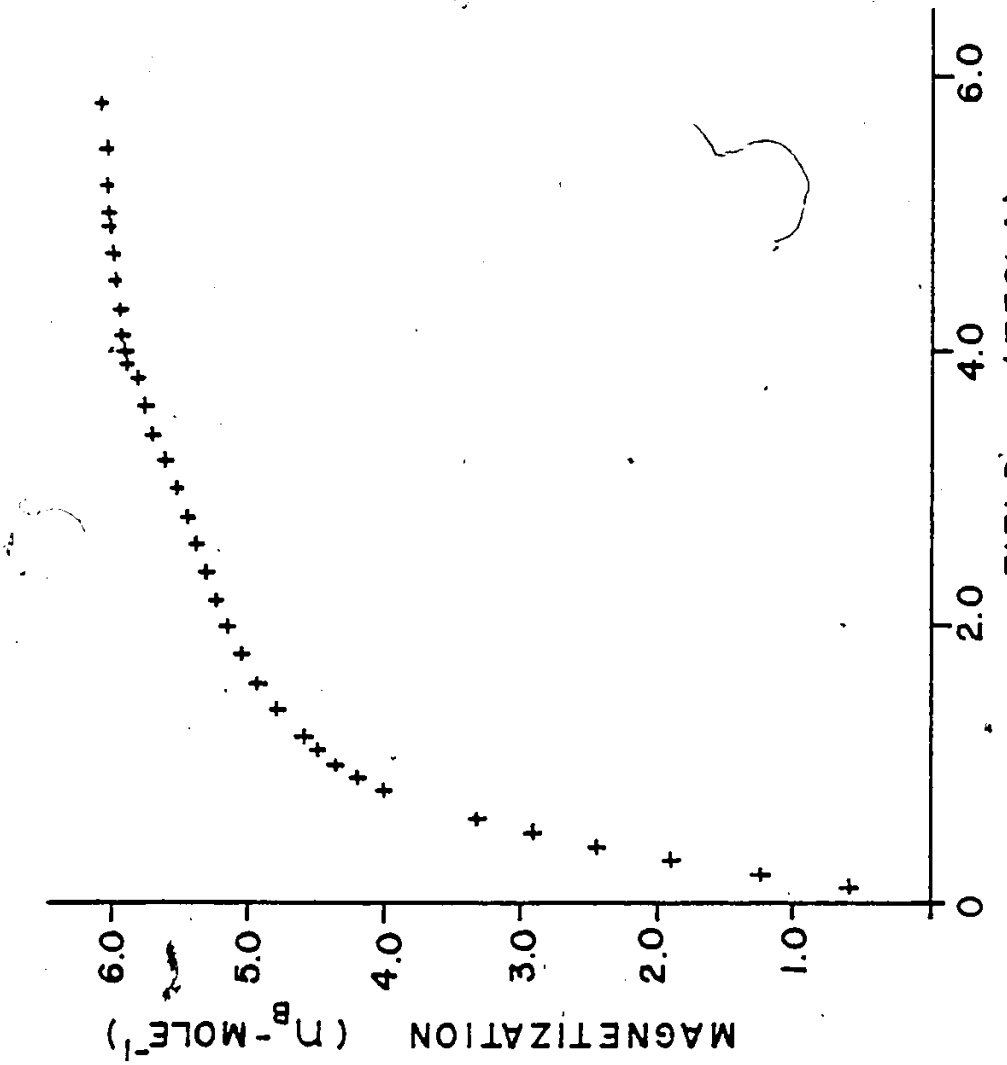

Figure 5-19 Magnetization versus field at 1.2K for $GdTiO_3$.

This conclusion implies the existence of a full local moment on Ti^{+3} and thus indicates localized d-electrons in $GdTiO_3$. These magnetic data are in poor agreement with the early low-temperature work of Bozorth et al.,[55] who reported on ordering temperature of 21 K and a much lower saturation moment.

The temperature dependence of the resistivity of $GdTiO_3$ is shown in Figure 5-20. The strong magnetic evidence for localized Ti^{+3} d-electrons suggests that the observed activated resistivity should be interpreted as being a consqeuence of small polaron transport as was the case for $PrTiO_3$ and $NdTiO_3$. The data, analyzed after equation (5-5), indicate E_a = 0.18 eV (high temperature) and 0.10 eV (low temperature). As for $PrTiO_3$, the lower temperature activation energy may be accounted for by the presence of impurity sites in the sample. These transport data are in good agreement with the high temperature work of Bozuev et al.,[26] who report an activation energy of 0.19 eV.

The results of the room temperature transmission infrared investigation of a single crystal of $GdTiO_3$ are shown in Figure 5-21, and of a low temperature (1.4 K) far-infrared investigation in Figure 5-22. Features of these spectra will be discussed later in this section, together with the optical results for $YTiO_3$.

The response of the magnetization of polycrystalline

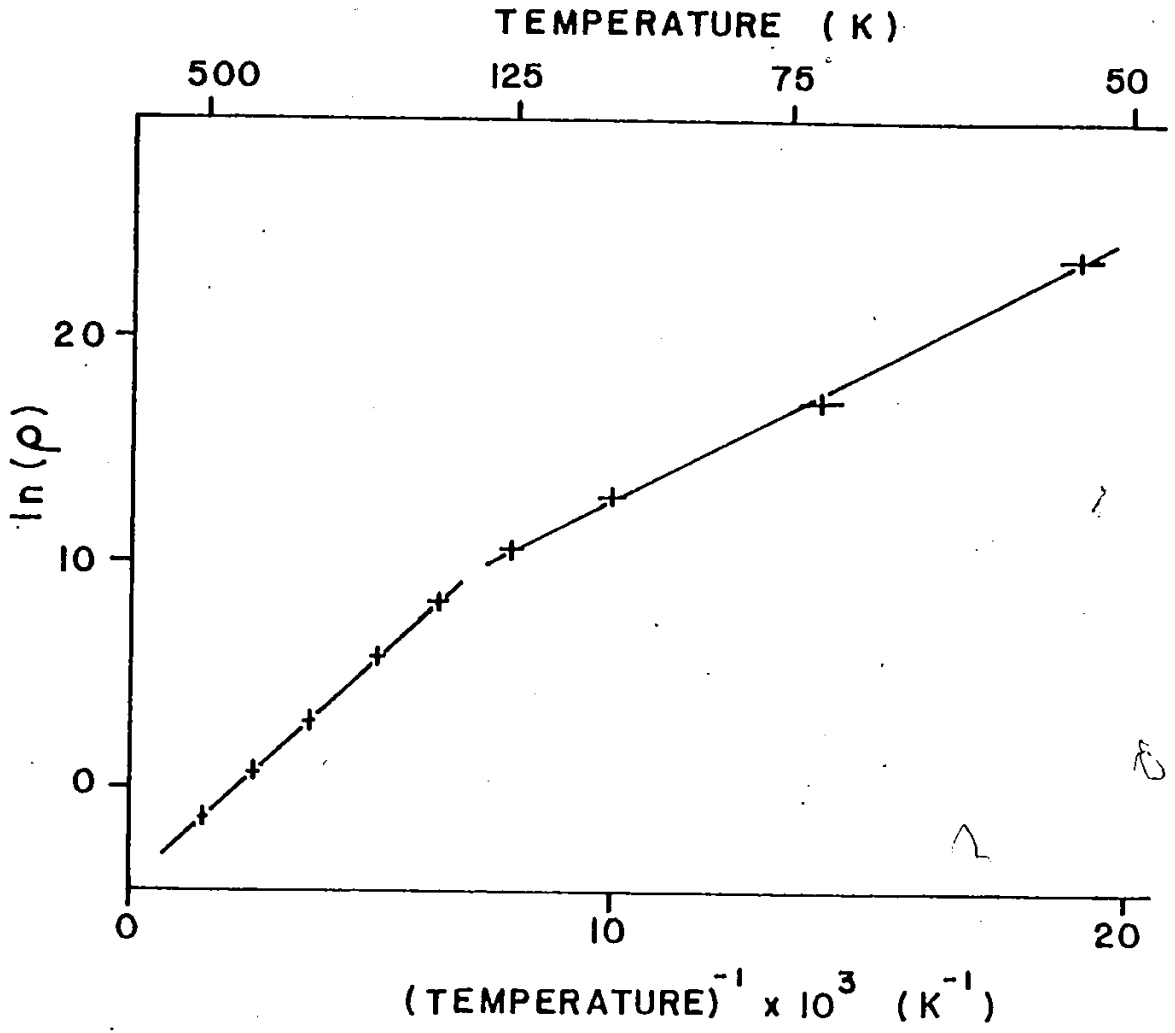

Figure 5-20 Natural logarithm of the resisitivity (in ohm-cm) versus reciprocal temperature for $GdTiO_3$.

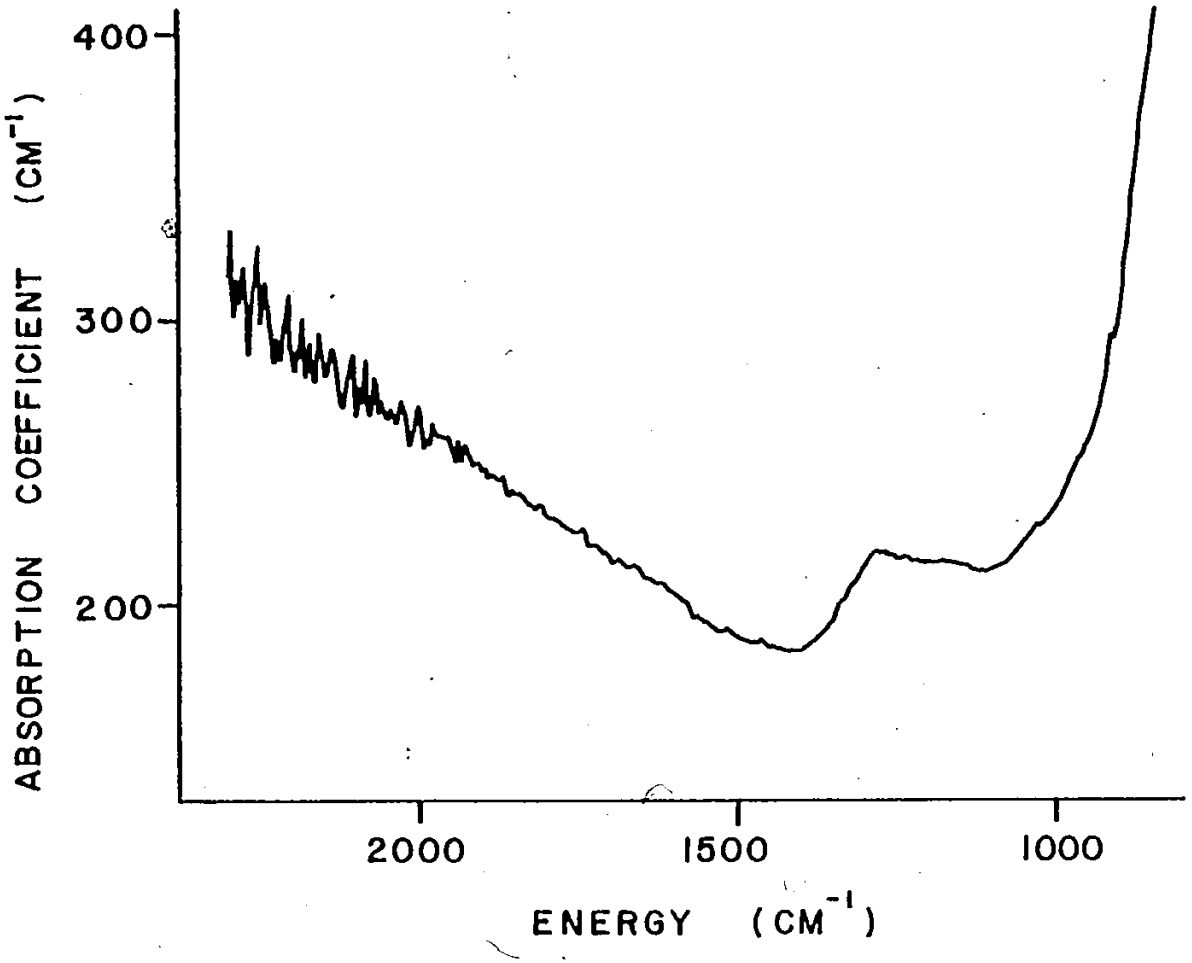

Figure 5-21 Absorption spectrum of $GdTiO_3$ in the range 800 cm^{-1} to 2500 cm^{-1}, obtained at 300K.

$YTiO_3$ to temperature in an applied field of 0.0800 T is shown in Figure 5-23. These data indicate that ferromagnetic ordering occurs at $T_c = 29 \pm 1$ K. The magnetic moment as a function of applied field at 4.2 K is shown in Figure 5-24. The magnetization data appear to saturate at $\sim 0.85\ \mu_B \cdot \text{mole}^{-1}$, although a gradual increase is noted with increasing field. As the Y^{+3} ion has no moment associated with it, the magnetic ordering must correspond to a ferromagnetic ordering of the Ti^{+3} d-electrons. These magnetic data are in excellent agreement with the low temperature work of Johnston.[56]

A single crystal of $YTiO_3$ (30.0 mg) of roughly ellipsoidal shape was used for orientational magnetic studies at low temperature (4.2 K). Figure 5-25 shows the magnetization as a function of crystal orientation in the a-c plane at an applied field of 0.1500 T. Figure 5-26 shows the field dependence of the magnetization for two crystal orientations. Figure 5-26(a) corresponds to the c-axis of the crystal being parallel to the pole axis of the magnet while Figure 5-26(b) corresponds to the a-axis being parallel to the pole axis. The facile magnetization in Figure 5-26(a) indicates that the c-axis is the easy direction for magnetization in the a-c plane of the crystal, while Figure 5-26(b) indicates that the a-axis is the hard direction for magnetization. Anisotropy of this kind exists in some materials because the electron spins are coupled to the orbital angular momentum through spin-orbit coupling, of the form $\lambda \underline{L} \cdot \underline{S}$.

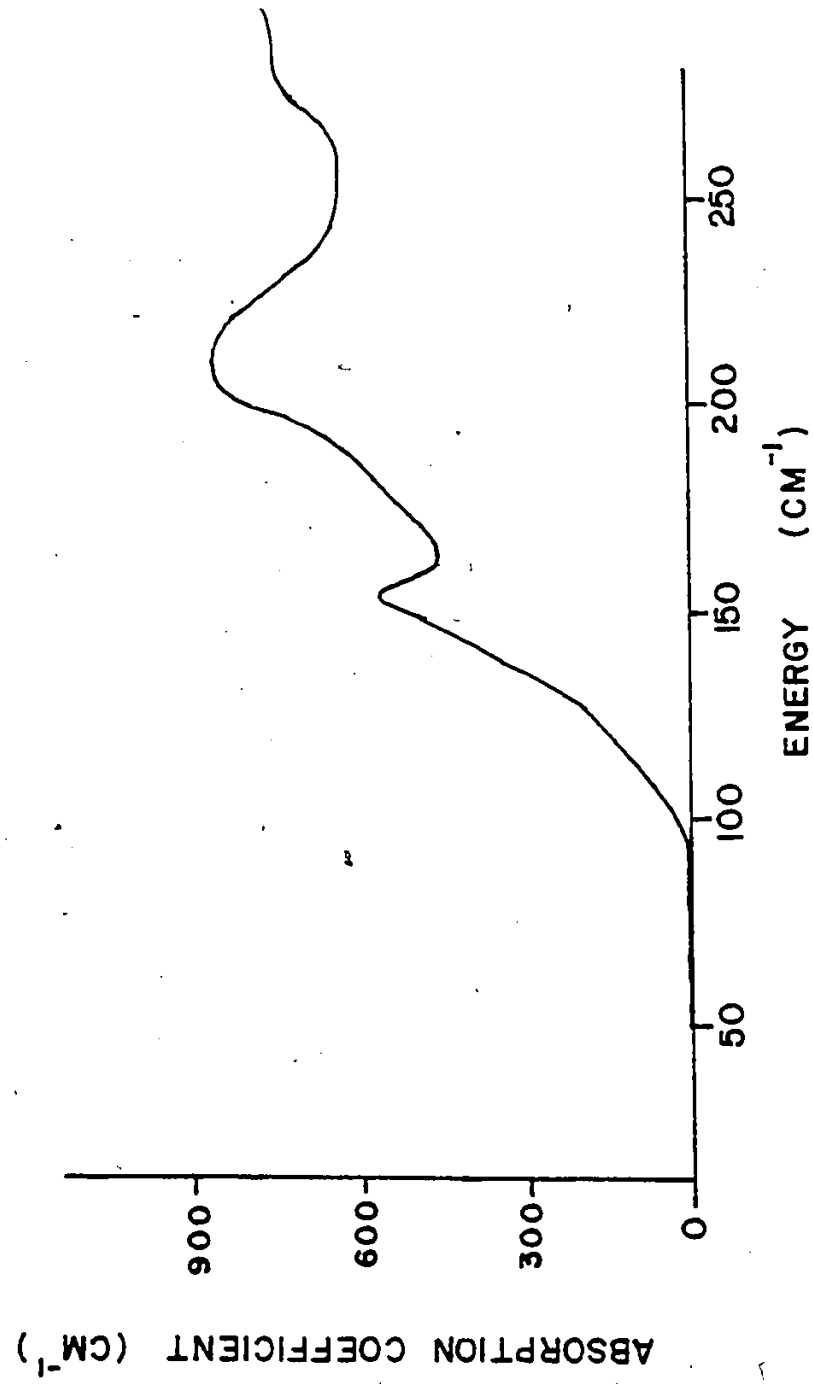

Figure 5-22 Linear absorption coefficient of $GdTiO_3$ as a function of energy in the range 50 cm^{-1} to 250 cm^{-1}. Data were obtained at 1.4K.

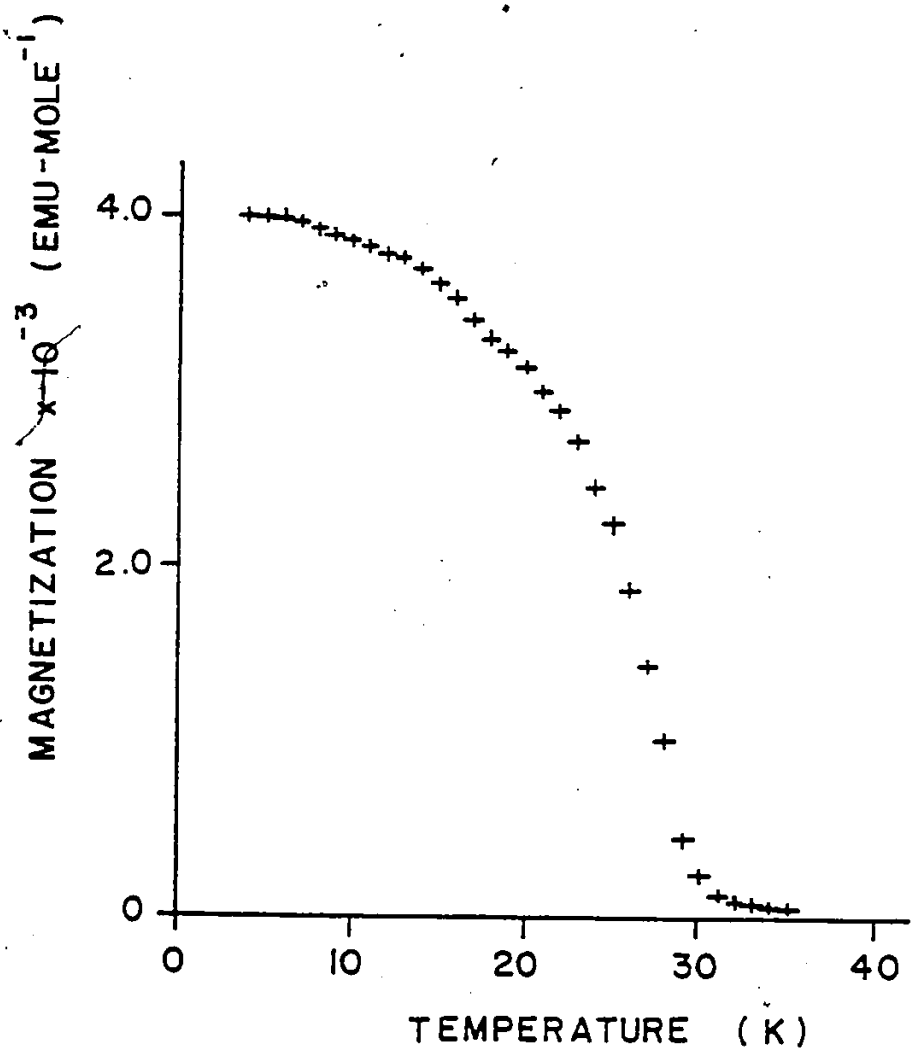

Figure 5-23. Magnetization versus temperature at 0.080 T for polycrystalline $YTiO_3$.

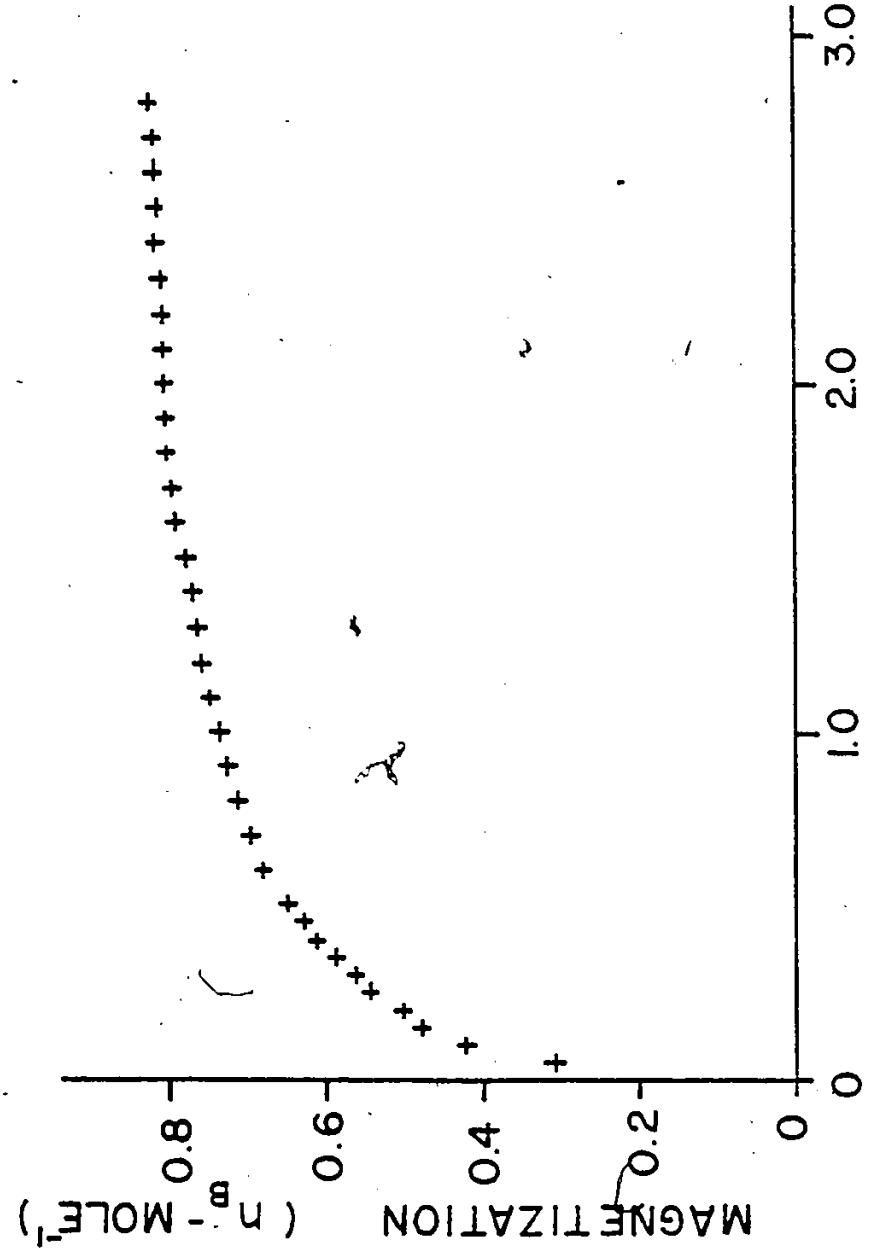

Figure 5-24 Magnetization versus field for polycrystalline $YTiO_3$ at 4.2K.

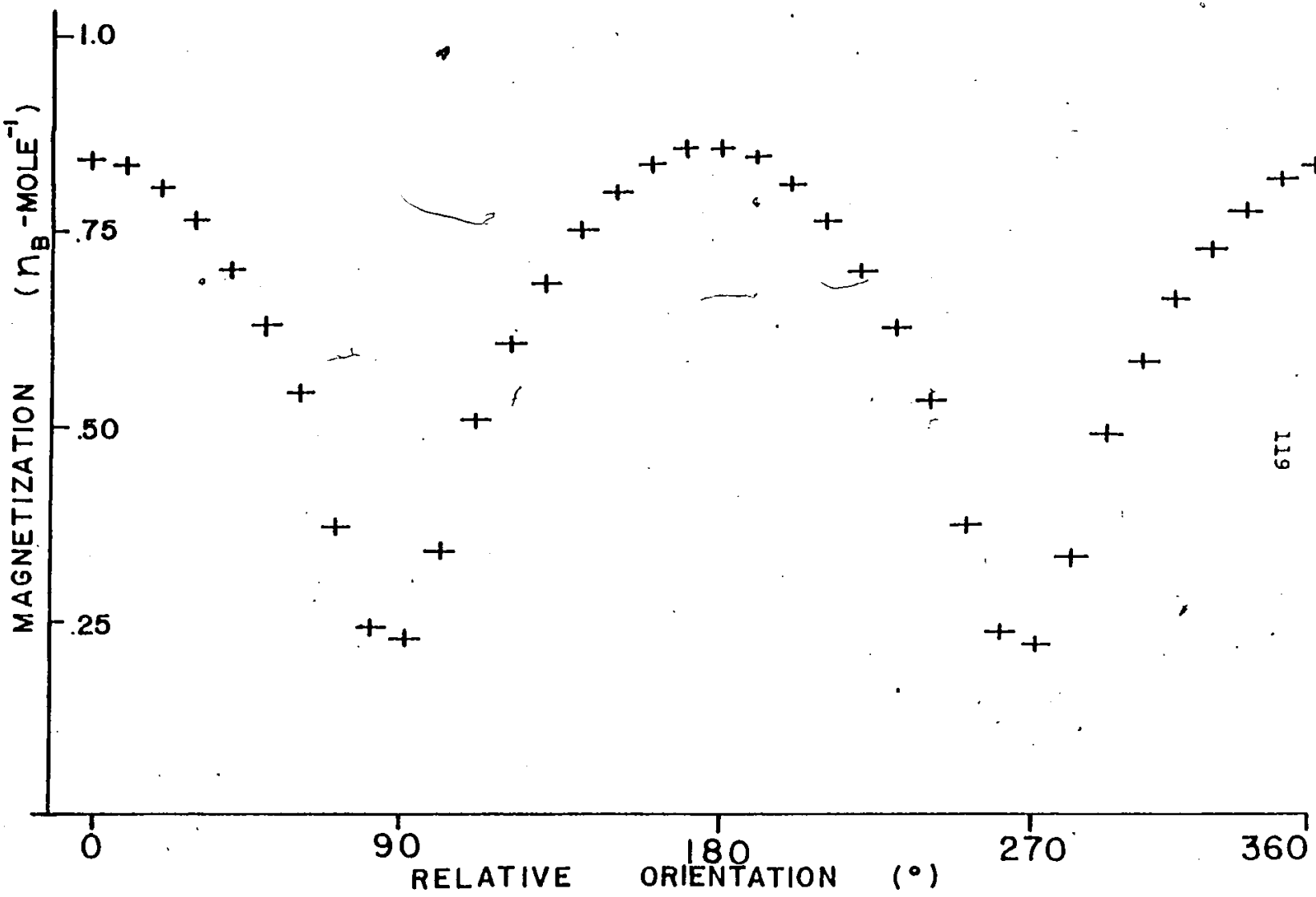

Figure 5-25. Magnetization of single crystal $YTiO_3$ at 4.2K and .15T as a function of orientation in the a-c plane. 0^o corresponds to the c-axis being parallel to the pole axis of the magnet, while 90^o corresponds to the a-axis being parallel.

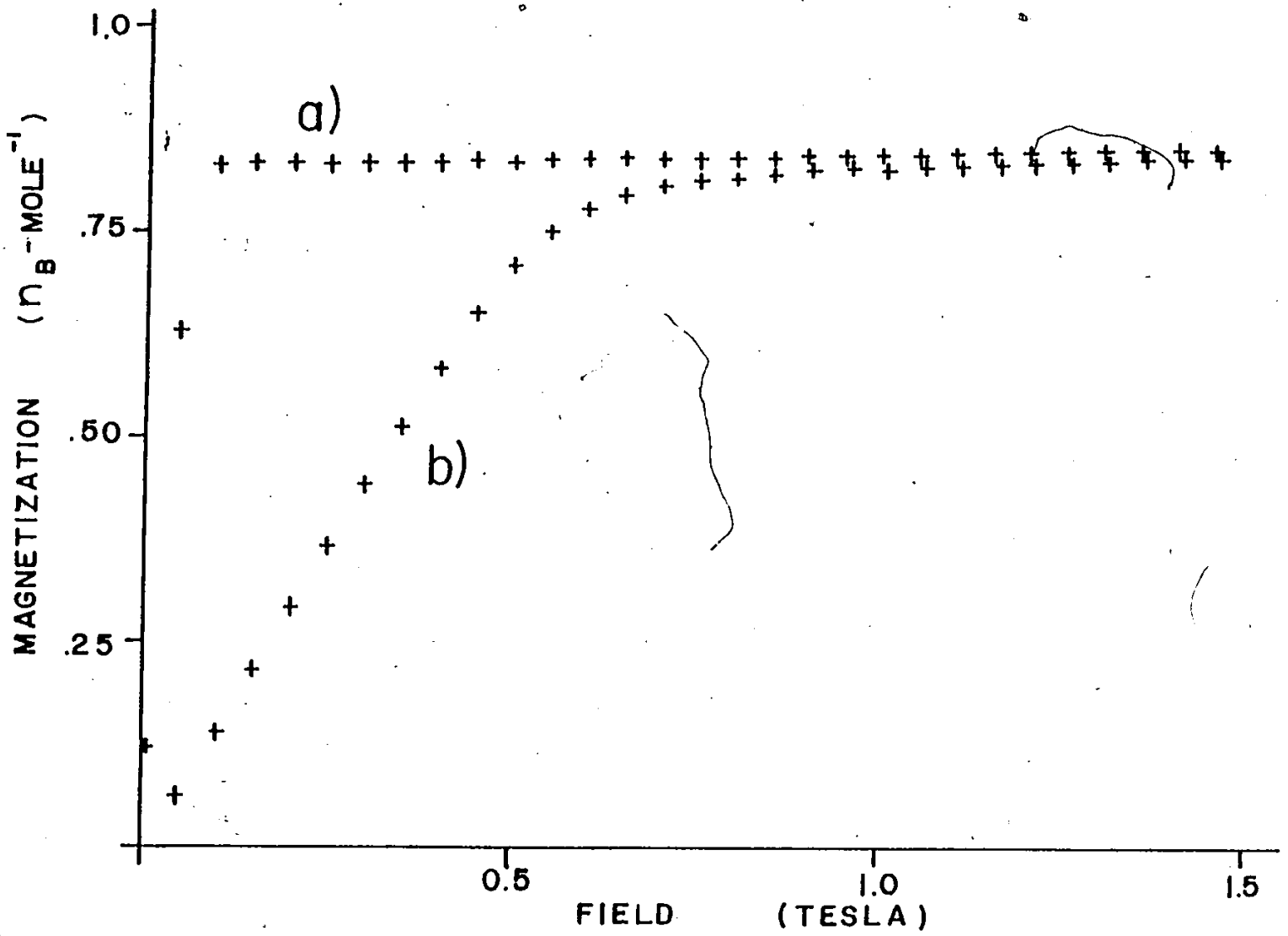

Figure 5-26 Magnetization as a function of applied field at 4.2K for single crystal $YTiO_3$. (a) and (b) correspond to orientations of 0^o and 90^o, respectively, referred to the orientation axis of Figure 5-25.

The orbital part of the ground state wave function is acted upon by the crystal field, and determines a preferred direction for the total magnetic moment. The anisotropy energy is the energy required to move the total moment from its preferred direction to the direction of the applied field.

A similar study was conducted looking at the a-b plane of the crystal. The anisotropy curve, shown in Figure 5-27, was obtained at an applied field of 0.2000 T. The magnetization versus field data at orientations of 0° and 90° (referred to the orientation axis of Figure 5-27) are shown in Figures 5-28 (a) and (b), respectively. These data indicate that the easy direction in the a-b plane of $YTiO_3$ is along the b-axis, and that the hard direction is along the a-axis. Note that curve "b" of Figure 5-26 corresponds to the same crystal orientation as curve "b" of Figure 5-28. The fact that these curves have different shapes presumably arises from a slight misorientation from the a-axis of the crystal being parallel to the pole axis of the magnet when these data were obtained. Figure 5-27 illustrates that the value of the magnetization changes quickly for a small change of orientation for orientations near the hard axis direction (90° in Figures 5-27).

Note for the hard direction in the a-b plane that

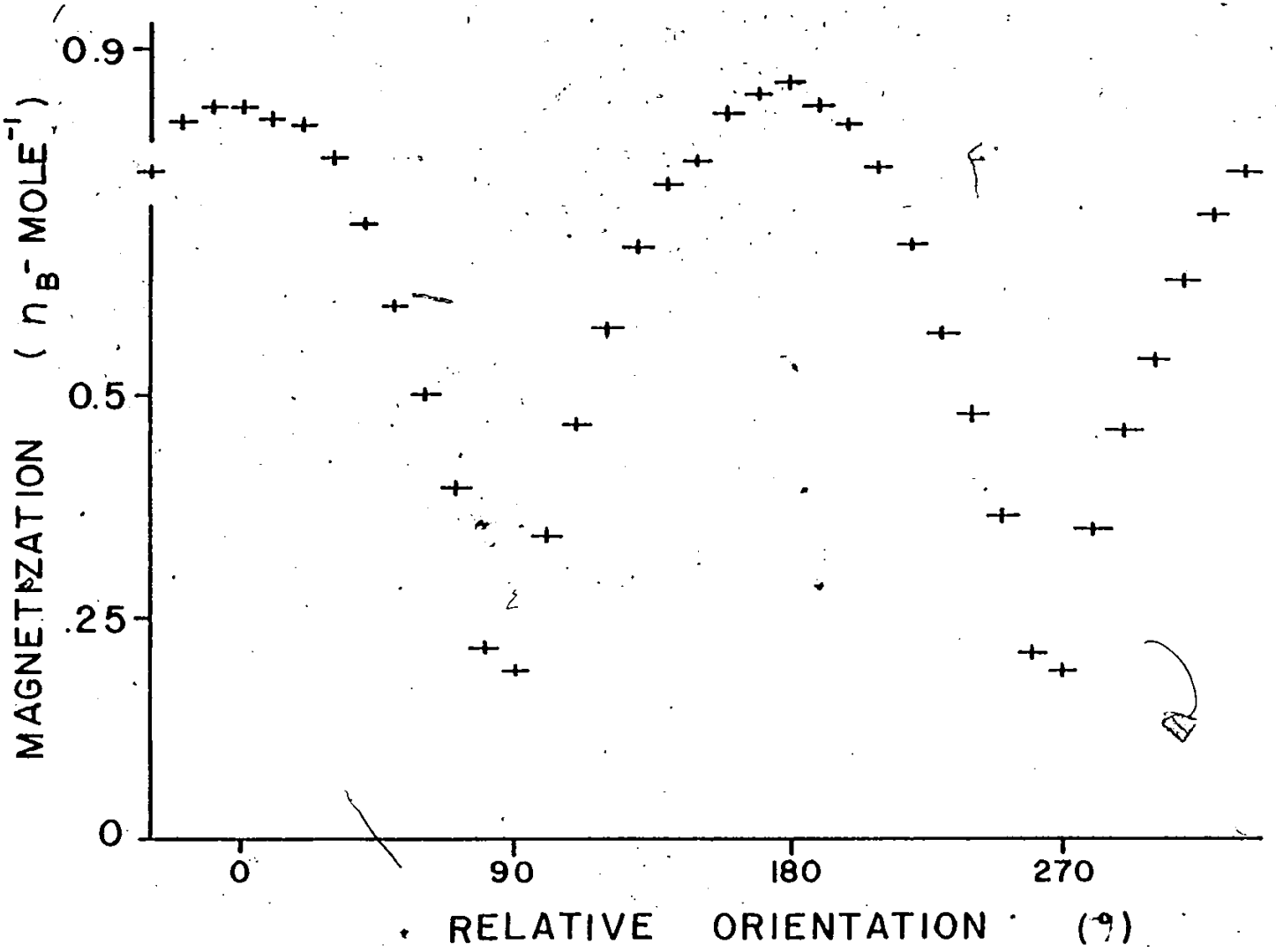

Figure 5-27. Magnetization of single crystal $YTiO_3$ at 4.2K and .2T as a function of orientation in the a-b plane. 0^o corresponds to the b-axis of the crystal being parallel to the pole axis of the magnet, while 90^o is for the a-axis being parallel.

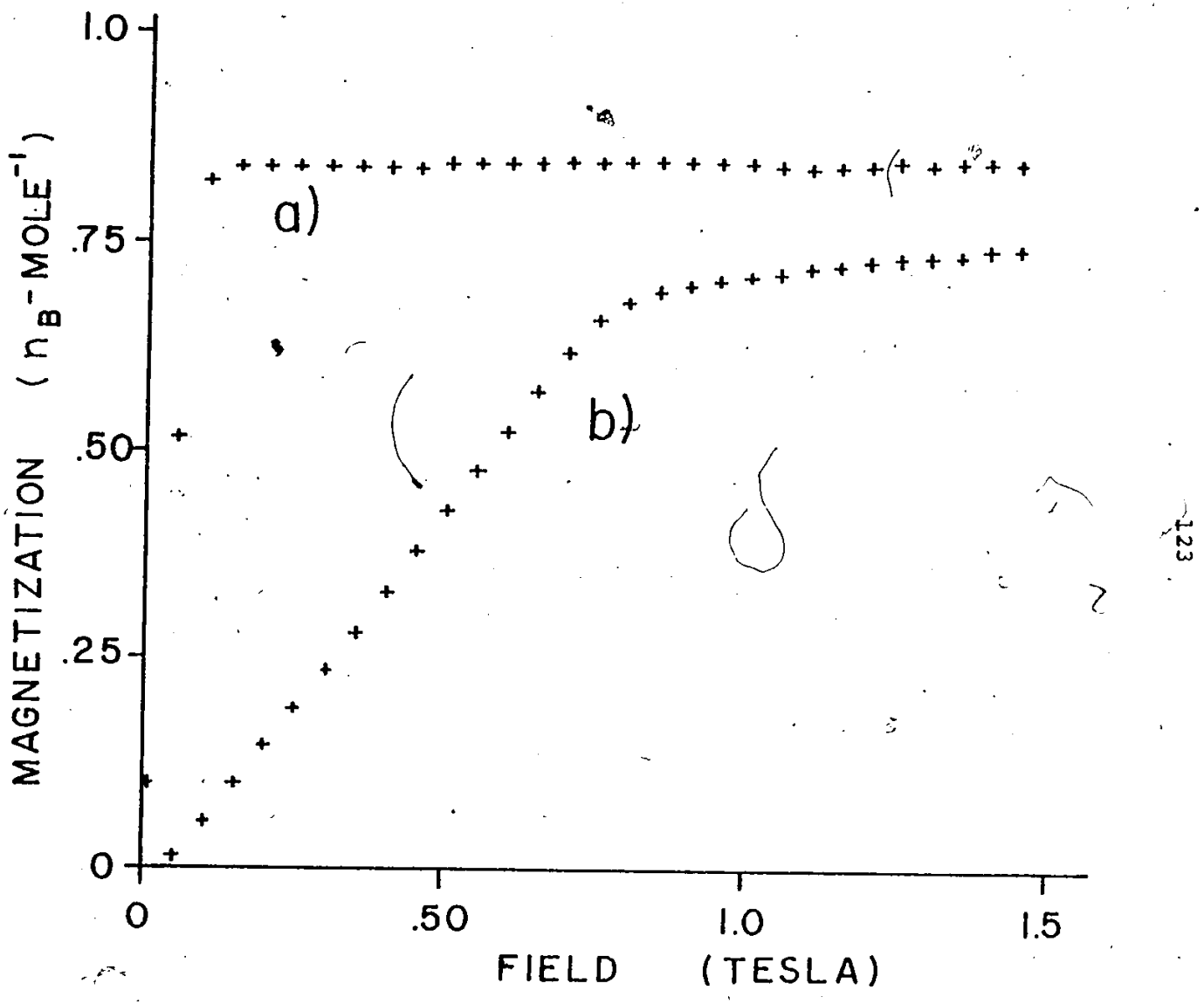

Figure 5-28. Magnetization as a function of applied field at 4.2K for single crystal $YTiO_3$. (a) and (b) correspond to orientations of 0° and 90°, respectively, referred to the orientation axis of Figure 5-27.

the magnetization has not saturated at 1.5 T. This is presumably responsible for the gradual increase in the saturation moment of polycrystalline $YTiO_3$ with increasing field observed in Figure 5-24.

The room temperature infrared spectrum obtained for $YTiO_3$ is shown in Figure 5-29, and a low temperature (1.4 K) far-infrared spectrum in Figure 5-30. These spectra have a number of features in common with those of $GdTiO_3$, Figures 5-21 and 5-22.

Both room temperature spectra show strong absorption from $\sim$ 1000 cm^{-1} to lower energy. This corresponds to Ti-O and RE-O vibrations reported by Bazuev et al.[62] Both spectra also show a marked decrease in the absorption coefficient as the frequency decreases to $\sim$ 1400 cm^{-1} (0.17 eV) for $GdTiO_3$ to $\sim$ 1300 cm^{-1} (0.16 eV) for $YTiO_3$. This suggests that there may be weak absorption edges for these materials at approximately those energies. The transport data of $GdTiO_3$ indicate that the activation energy for conduction near room temperature is $\sim$ 0.18 eV. This suggests a connection between the weak absorption edge and the conduction mechanism in this crystal.

Another feature which is common to both room-temperature spectra is the presence of weak absorption bands occurring just before the onset of strong lattice vibrations. For $YTiO_3$, there are two distinct absorptions, one at 1195 $\pm$ 20 cm^{-1}, the other at 1315 $\pm$ 20 cm^{-1}. For $GdTiO_3$, the absorption

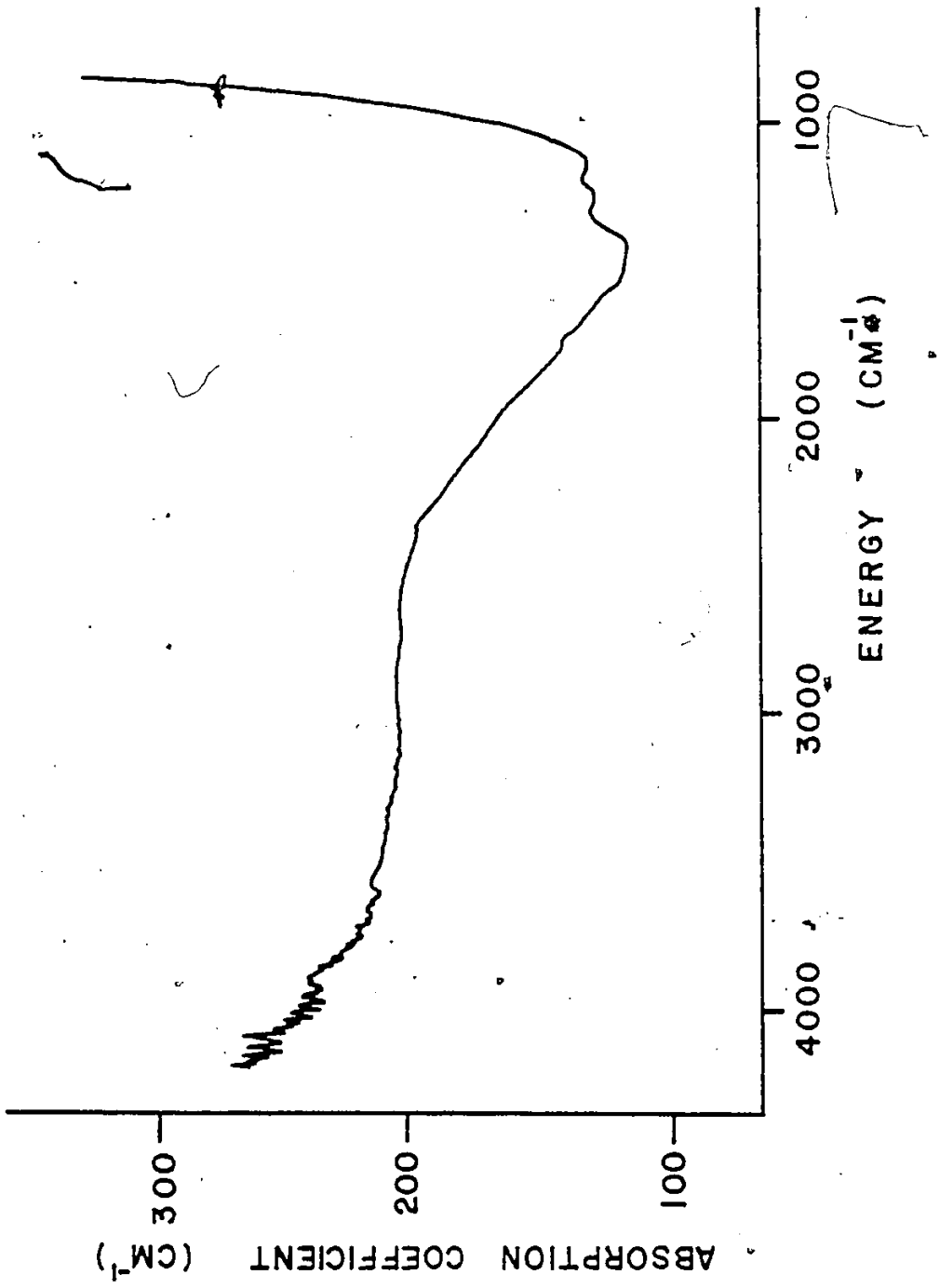

Figure 5-29 Absorption spectrum of $YTiO_3$ in the range 800 cm^{-1} to 4000 cm^{-1}, obtained at 300K.

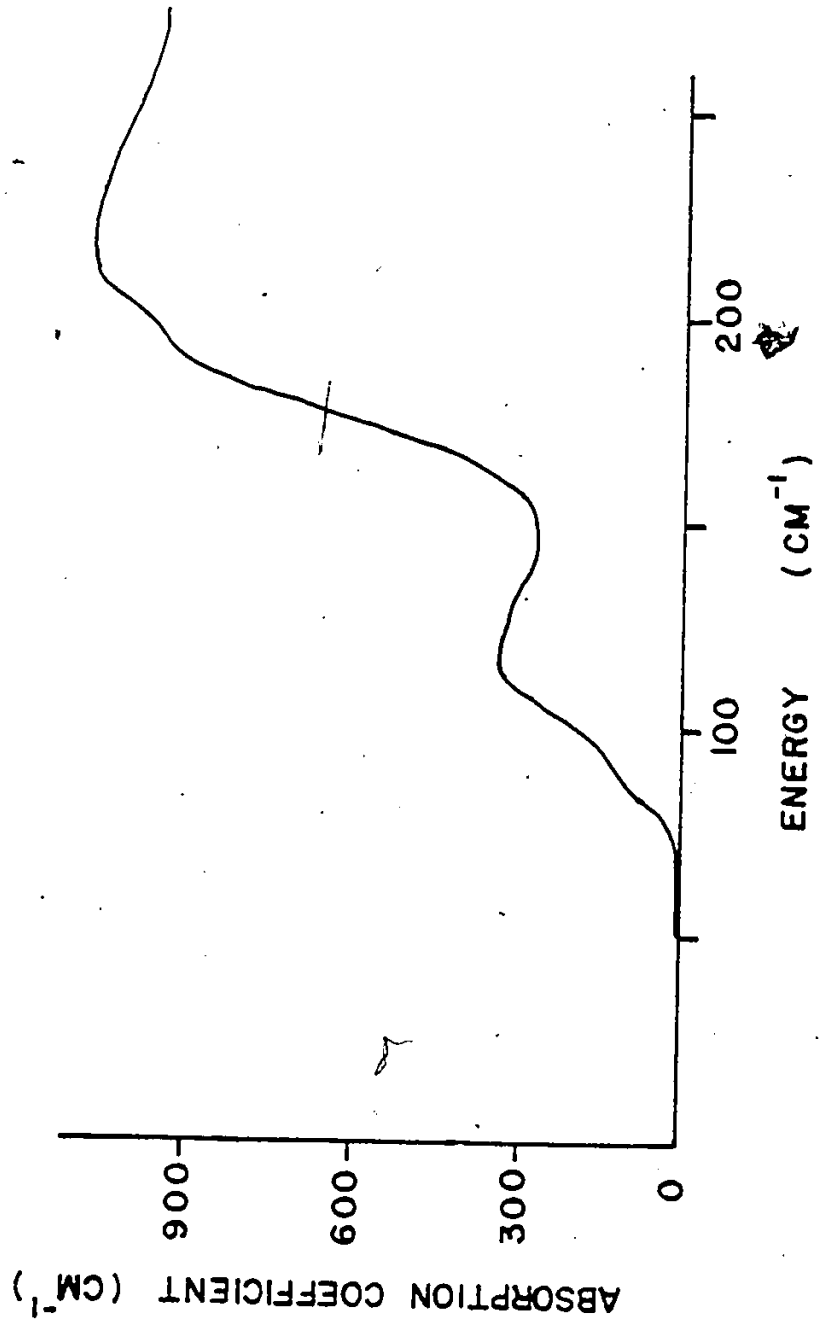

Figure 5-30 Linear absorption coefficient of $YTiO_3$ as a function of energy in the range 50 cm^{-1} to 250 cm^{-1}. Data were obtained at 1.4K.

band is broader, perhaps containing more than one peak, but only the centre of the absorption band can be located, occurring at $\sim$ 1200 cm^{-1}.

The low temperature spectra of $GdTiO_3$ and $YTiO_3$ both show transparency below $\sim$ 80 cm^{-1}, indicating that there is no delocalized electron behaviour in these materials. There is a weak absorption for $YTiO_3$ at $\sim$ 120 cm^{-1} and one for $GdTiO_3$ at $\sim$ 155 cm^{-1}.

The molar extinction coefficients for these absorption peaks ($\sim$ 400-600 cm^{-1}) are similar to those of the weak peaks observed at 1200-1300 cm^{-1}. It is possible that the absorptions at 120-150 cm^{-1}, along with those observed at 1200-1300 cm^{-1} in $GdTiO_3$ and $YTiO_3$, are due to d-d transitions within the Ti^{+3} ion. This possibility will now be considered further.

Recall that the solution of the crystal structures of $GdTiO_3$ and $YTiO_3$ in Chapter 3 revealed a distortion of the TiO_6 octahedron for both these compounds. (Details of the environment of the TiO_6 octahedron are given in Table 3-7.) The nature of this distortion is a tetragonal-like elongation of $\sim$ 3% along one of the Ti-O axes. This kind of distortion has an effect upon the d-energy levels of transition metal ions and has been considered by Orton[94] and Ballhausen.[95] The results for a tetragonally distorted TiO_6 octahedron will be presented in a qualitative way.

Figure 5-31 shows the qualitative splitting of the 3d energy levels of a d^1 ion by the successive application of various perturbations. The free ion term for a d^1 ion is ^2D. In an octahedral crystal field, the levels are split into a lower set of T_2 symmetry and an upper set of E symmetry, separated by an energy Δ_o, as shown in Figure 5-31(a). Figure 5-31(b) shows the effect of a tetragonal elongation, like that observed in $GdTiO_3$ and $YTiO_3$, giving rise to the splitting δ in the T_2 multiplet. The effect of spin-orbit coupling, described by the spin-orbit coupling constant ζ, is included in Figure 5-31(c).

The energy level scheme that results has two levels separated by an energy on the order of the spin-orbit coupling constant as lowest in energy. The next level is at an energy $\sim \delta$ above these, the magnitude of δ depending upon the extent and effect of the tetragonal elongation. The states arising from the E multiplet are higher in energy, the amount determined by Δ_o.

The value of the spin-orbit coupling constant for free ion Ti^{+3} is 154 cm^{-1},[96] although, for an ion in a crystal, ζ is usually 20-30% below the free ion value.[94] The value of Δ_o found for Ti^{+3} in oxide environments similar to those in $GdTiO_3$ and $YTiO_3$ is $\sim$ 19,000 cm^{-1}.[97] The value of δ, however, can be quite small for Ti^{+3} in some cases ($\sim$ 110 cm^{-1} for Ti^{+3} in Al_2O_3 [98]) and considerably larger in others ($\sim$ 7,500 cm^{-1} for Ti^{+3} in titanium triacetyl-

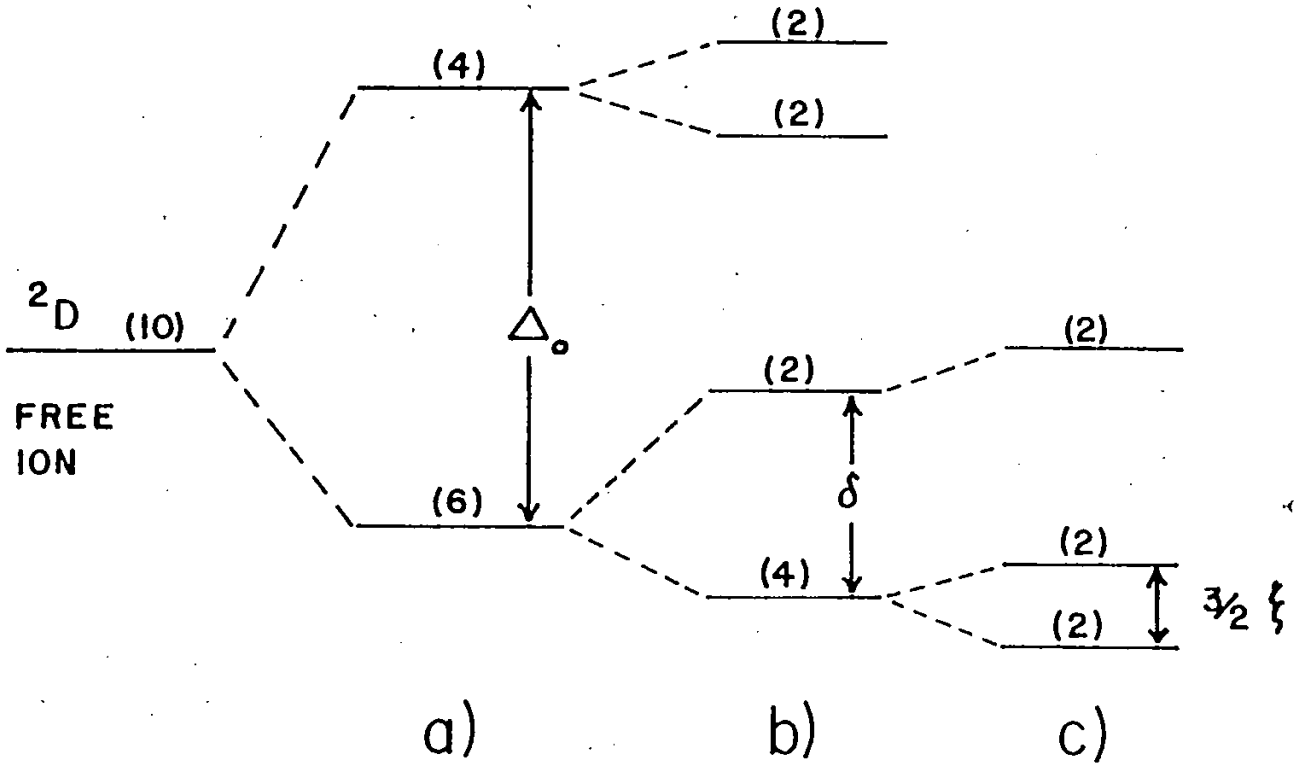

Figure 5-31 A schematic energy level splitting scheme for a ^{2}D free ion term under (a) a cubic crystal field; (b) including a tetragonal elongation and (c) spin orbit coupling. (After reference 97.).

acetonate[99]).

If the weak absorption bands in $GdTiO_3$ and $YTiO_3$ at $\sim$ 120-150 cm^{-1} and $\sim$ 1200-1300 cm^{-1} are due to d-d transitions, the low energy transitions would be occurring between the lowest two energy levels of Figure 5-32(c) and would be of energy $\sim \zeta$. The transitions at $\sim$ 1200-1300 cm^{-1} clearly will not correspond to Δ_o, but are more likely to arise from transitions between the T_2 multiplet levels which are separated by an energy of $\sim \delta$. One would expect to see one transition at low energy ($\sim \zeta$) and two transitions at an energy $\sim \delta$ separated by $\sim \zeta$. This is exactly the pattern that is observed for the weak absorptions in $YTiO_3$.

Orton has done a more quantitative treatment of the effect of tetragonal elongations including spin-orbit coupling on the energy levels within a Ti^{+3} ion. The way in which the energies of the three levels arising from the T-multiplet shift as a function of increasing elongation is shown in Figure 5-32. In $YTiO_3$ and $GdTiO_3$, for which δ/ζ appears to be $\sim$ 8, an energy level scheme like the lower portion of Figure 5-31(c) is predicted. However, the wave functions of the ground state doublet E_o are non-magnetic, as the orbital and spin contributions to the magnetic moment exactly cancel.[94] Nonetheless, $YTiO_3$ and $GdTiO_3$ do order magnetically at 29 K and 34 K, respectively. If the ground state in these systems is E_o, then magnetic ordering may be occurring by an exchange induced moment mechanism as is proposed for rare earth ions with singlet ground states that order magnetically (i.e., HoP, ErN).[100,101,102]

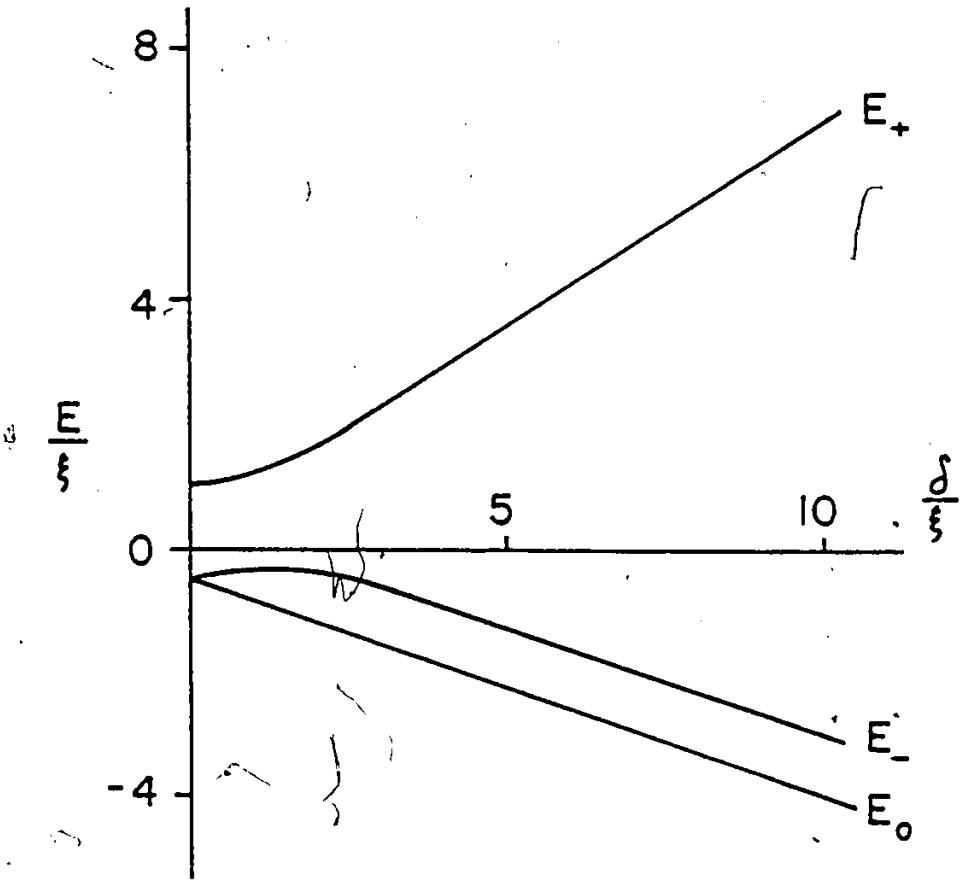

E_o doublet wave functions - $|\Psi_+\rangle = |-1,+\tfrac{1}{2}\rangle$

$|\Psi_-\rangle = |+1,-\tfrac{1}{2}\rangle$

E_- doublet wave functions - $|\Psi_+\rangle = a_1|-1,-\tfrac{1}{2}\rangle + a_2|g,+\tfrac{1}{2}\rangle$

$|\Psi_-\rangle = a_1|1,\tfrac{1}{2}\rangle - a_2|g,-\tfrac{1}{2}\rangle$

where $|g\rangle \equiv 1/\sqrt{2}(|2\rangle - |-2\rangle)$

Figure 5-32. Splitting of the energy states arising from the T multiplet of the Ti^{+3} ion in an octahedral field as a function of increasing tetragonal elongation. Wave functions for the lowest two doublets are shown.

One should also consider that the actual distortion of the TiO_6 octahedron in $YTiO_3$ and $GdTiO_3$ is not purely tetragonal (note the bond angles and distances in Table 3-7), so that the energy levels of Figure 5-32 may be shifted enough in $GdTiO_3$ and $YTiO_3$ to result in the ground state being E_-, which is magnetic.

Thus, the weak absorption bands in $GdTiO_3$ and $YTiO_3$ may be due to d-d transitions in Ti^{+3}. This implies localized d-electron behaviour for these compounds, and is consistent with the magnetic and transport data for these materials which suggest the same conclusion.

5.5 $La_xY_{1-x}TiO_3$ Series

Compounds in the series of solid solutions $La_xY_{1-x}TiO_3$ are of interest as they span the unit cell parameters and presumably the Ti^{+3} d-electron behaviour of the $RETiO_3$ series from $LaTiO_3$ to $YTiO_3$. As both La^{+3} and Y^{+3} are closed shell ions, the only magnetic species in these materials is Ti^{+3}. An advantage in studying members of this series, then, is that one is observing the behaviour of the Ti^{+3} d-electron only, with no "interference" from the presence of local moments on the rare earth ion.

The magnetic properties of two end-members of this series, $LaTiO_3$ and $YTiO_3$, have been discussed earlier in this chapter. Results from those studies will be reproduced in this section where appropriate.

The molar susceptibility, corrected for diamagnetism, has been measured as a function of temperature in the range 80 K to 300 K for polycrystalline $La_xY_{1-x}TiO_3$, x = 0.1, 0.2, 0.4 and 0.7. These data, presented as reciprocal susceptibility versus temperature, are shown in Figure 5-33. Non-linear behaviour is evident, and deviations from linearity occur in the same way as for $CeTiO_3$. These $La_xY_{1-x}TiO_3$ data were analyzed in the same way as the $CeTiO_3$ data, i.e., they were fitted to equation (5-4). The parameters of these fits are given in Table 5-3, and the inverse susceptibility, $(\chi'_M)^{-1}$, where $\chi'_M = \chi_M - \chi_{T.I.P.}$, is shown as a function of temperature in Figure 5-34. Of particular interest is the variation of the magnitude of the temperature-independent term in the susceptibility, $\chi_{T.I.P.}$, with x. The relationship, shown in Figure 5-35, reveals a roughly linear dependence. If, as in $LaTiO_3$ and $CeTiO_3$, this term corresponds to a delocalized electron Pauli susceptibility, these data suggest that there may be two "kinds" of d-electrons in these phases. Some of the d-electrons may be delocalized, giving rise to the Pauli term, while others may be localized on Ti^{+3} sites, giving rise to a Curie-Weiss term in the susceptibility. The Curie-Weiss contribution does not appear to be near the spin-only value. Notice in Table 5-3 that as x increases, the value of θ_c tends to become increasingly negative. This may reflect the importance of negative exchange interactions or crystal field effects or both.

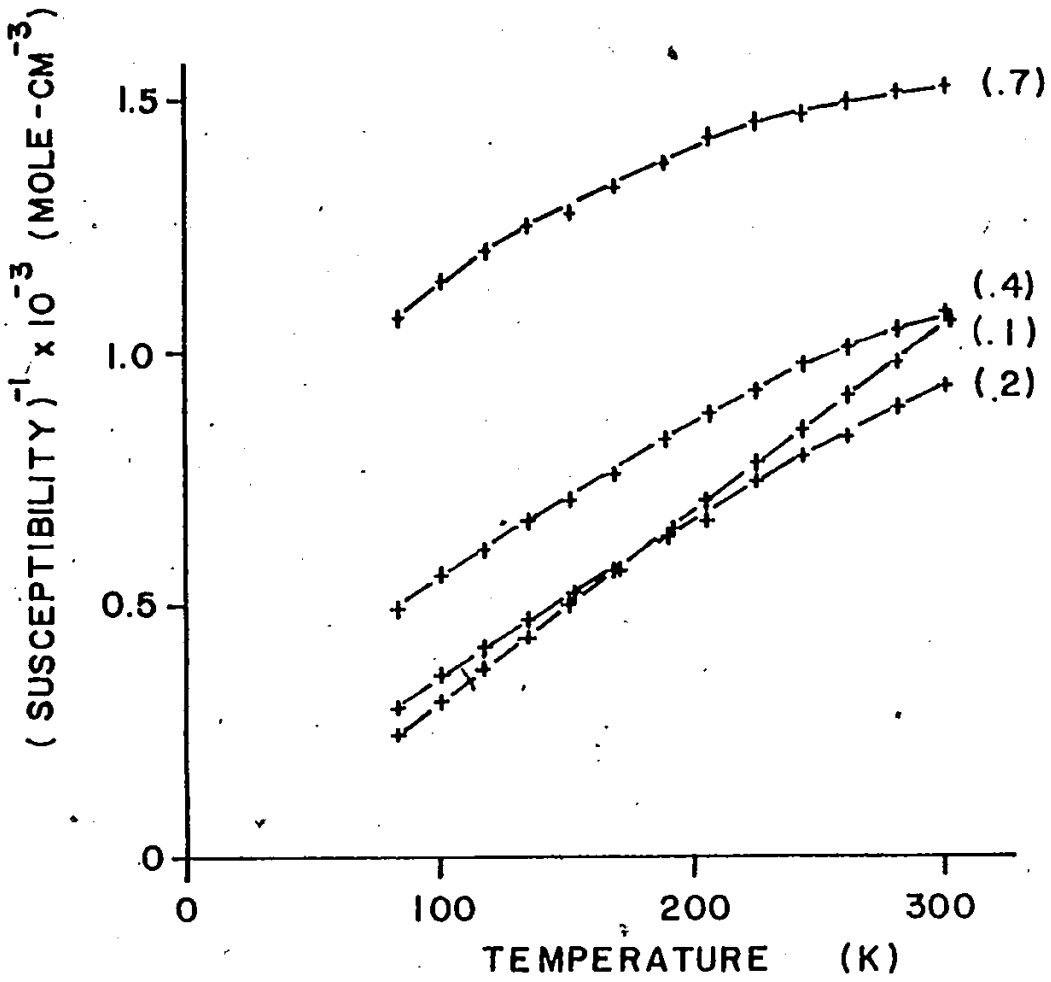

Figure 5-33 Raw inverse susceptibility versus temperature for various $La_xY_{1-x}TiO_3$ phases. The value of x is shown in brackets beside the appropriate curve.

Table 5-3

Parameters obtained from the fitting of $La_xY_{1-x}TiO_3$ susceptibility data to equation (5-4)

x	0*	0.1	0.2	0.4	0.7	1.0**
$\chi_{T.I.P.}$ (10^{-6}cm^3 mole^{-1})	0.0	0.0	180.0	380.0	510.0	800.0
C (cm^{3}K mole^{-1})	0.35	0.27	0.27	0.17	0.04	---
θ_c (K)	33.0	19.0	1.0	-20.0	-13.0	---
Regression Coefficient	--	.9999	.9997	.9989	.9970	---

* Data from Reference 56.

** Data from section 5-2.

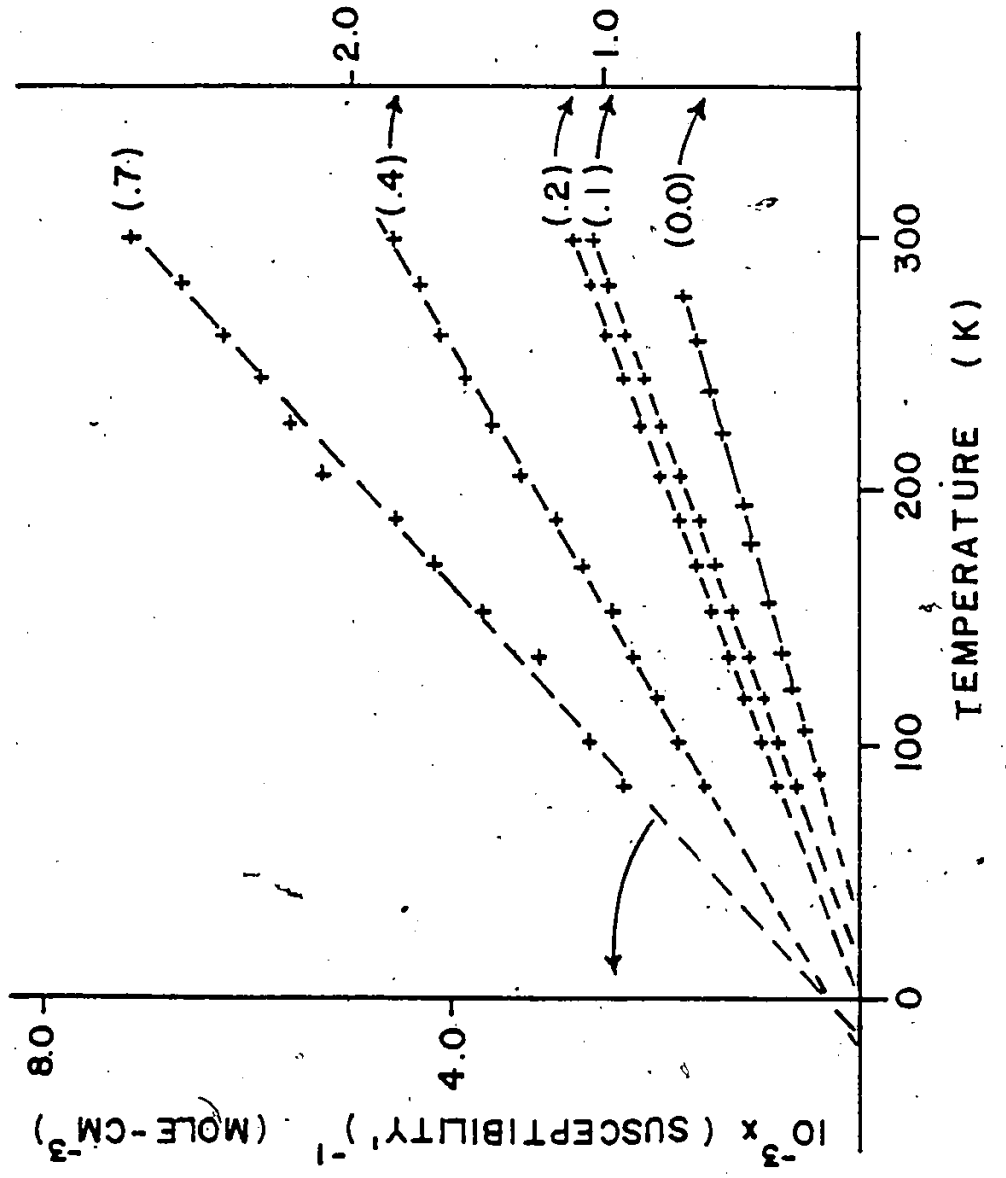

Figure 5-34 Reciprocal susceptibility (corrected after equation 5-4) versus temperature for various $La_xY_{1-x}TiO_3$ phases. The value of x is shown in brackets beside the appropriate curve.

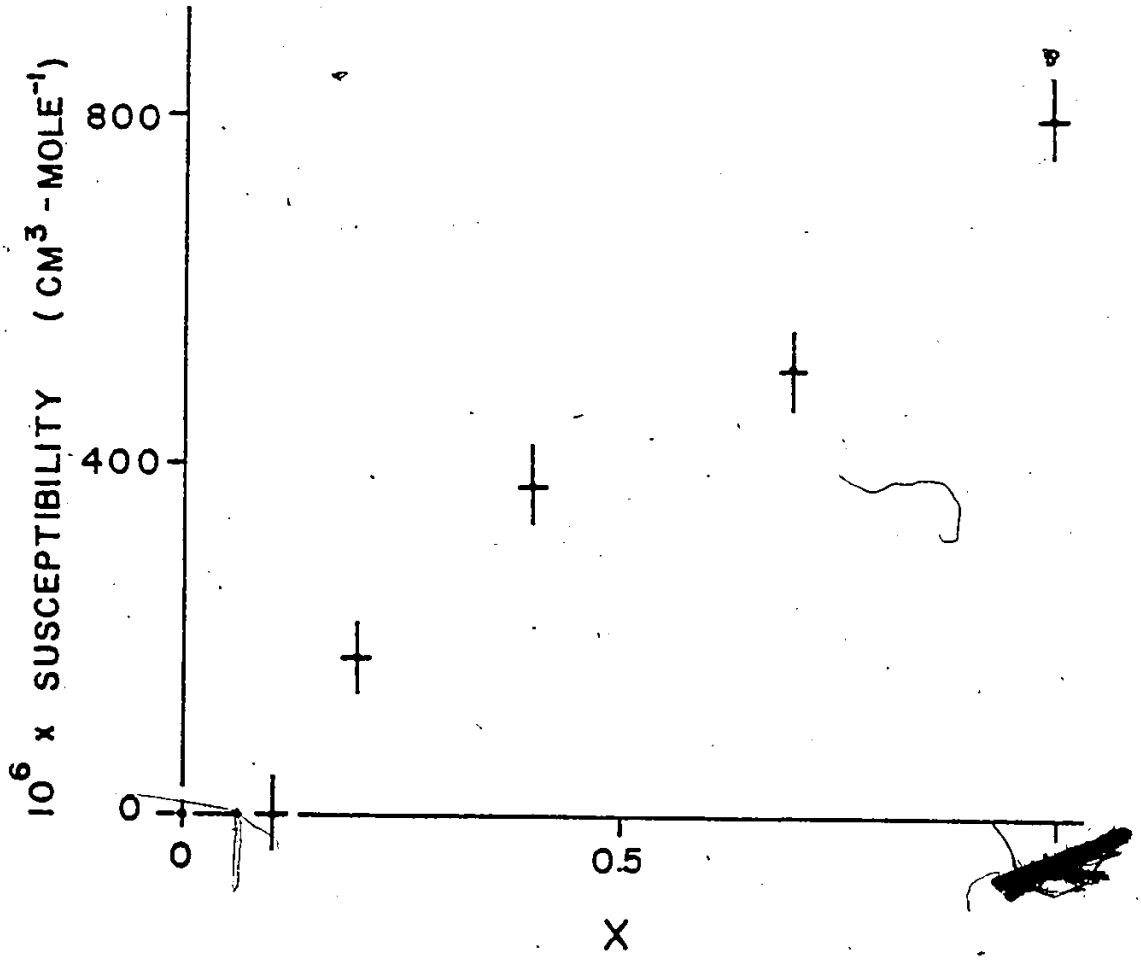

Figure 5-35. The value of temperature-independent susceptibility as a function of x in the series $La_xY_{1-x}TiO_3$.

The results of low temperature (4.2 K) magnetic studies of various members of the solid solution $La_xY_{1-x}TiO_3$ are shown in Figures 5-36 and 5-37, and the results are summarized in Figure 5-38, where both the saturation moment and the Curie temperature are plotted as a function of unit cell volume in order to facilitate comparison with other $RETiO_3$ phases. Notice the sharp drop in saturation moment for small values of x, reaching the small saturation moment of $\sim 0.02\ \mu_B$ for $x \sim 0.5$. The ordering temperature also decreases with increasing x, but in a less dramatic way. Above $x = 0.4$, the magnetization-temperature curves are very similar and the Curie temperature is difficult to locate but does not appear to change very much. The composition for which all signs of magnetic order disappear is difficult to locate exactly as sample signals become quite small, but appears to be about $x = 0.7$.

The cell volume of $GdTiO_3$ is shown along the volume axis of Figure 5-38. If the saturation moment of Ti^{+3} is a function of cell volume only, one would expect to observe a saturation moment of $\sim 0.2\ \mu_B$ for Ti^{+3} in $GdTiO_3$. Recall, however, that $GdTiO_3$ appears to be a collinear ferrimagnet, with a value of about $1.0\ \mu_B$ for the Ti^{+3} moment. Thus, the saturation moment on Ti^{+3} in the $RETiO_3$ phases seems to be dependent not only on the size of the RE ion but also upon its magnetic moment.

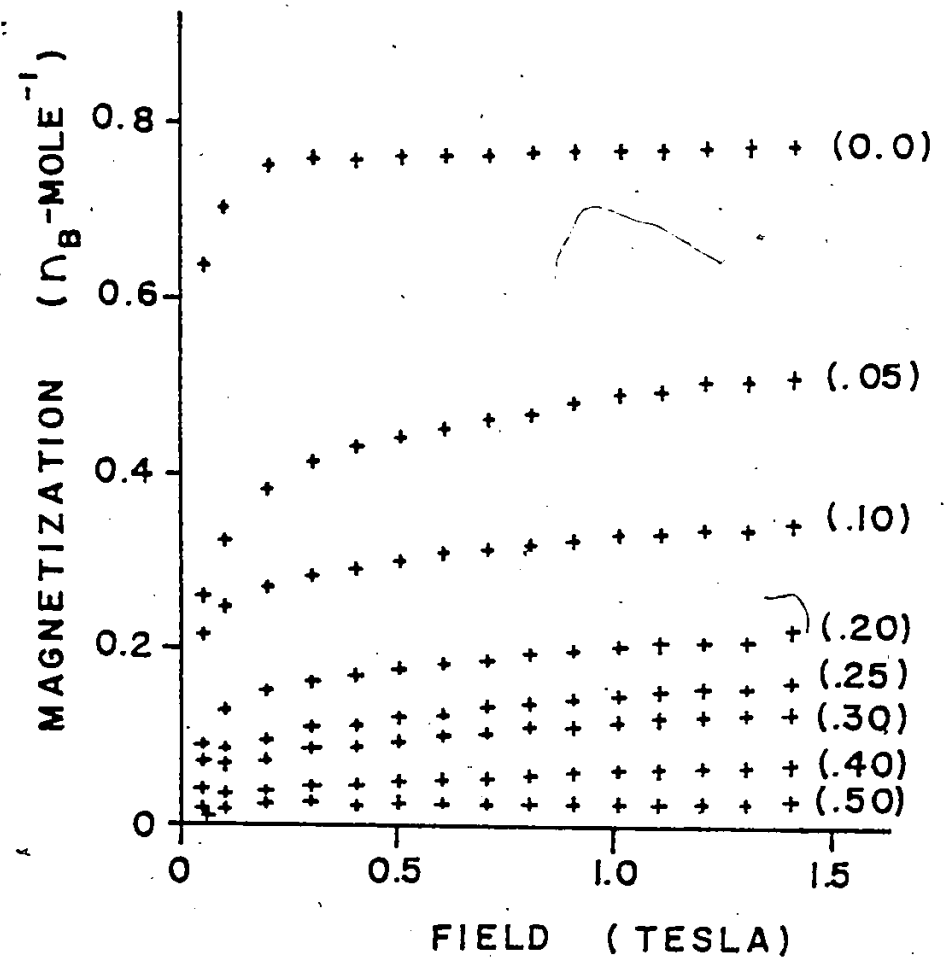

Figure 5-36. Magnetization as a function of applied field at 4.2 K for various $La_xY_{1-x}TiO_3$. The value of x is indicated in brackets beside the appropriate curve.

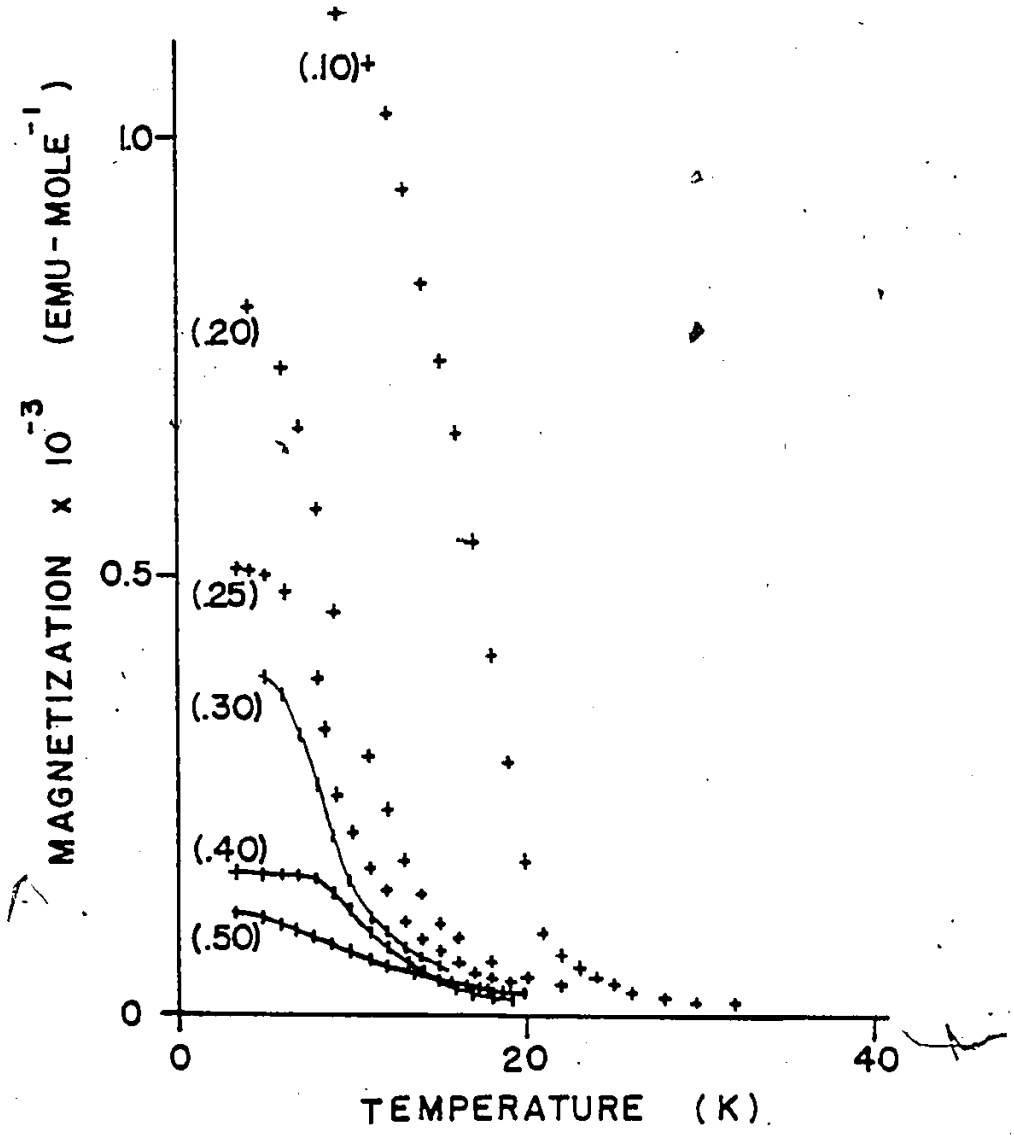

Figure 5-37. Magnetization versus temperature for various $La_xY_{1-x}TiO_3$ phases. The value of x is indicated in brackets beside the appropriate curve. Data for x = 0.1 and x = 0.4 were obtained at 0.08 T; data for the other phases at 0.14 T.

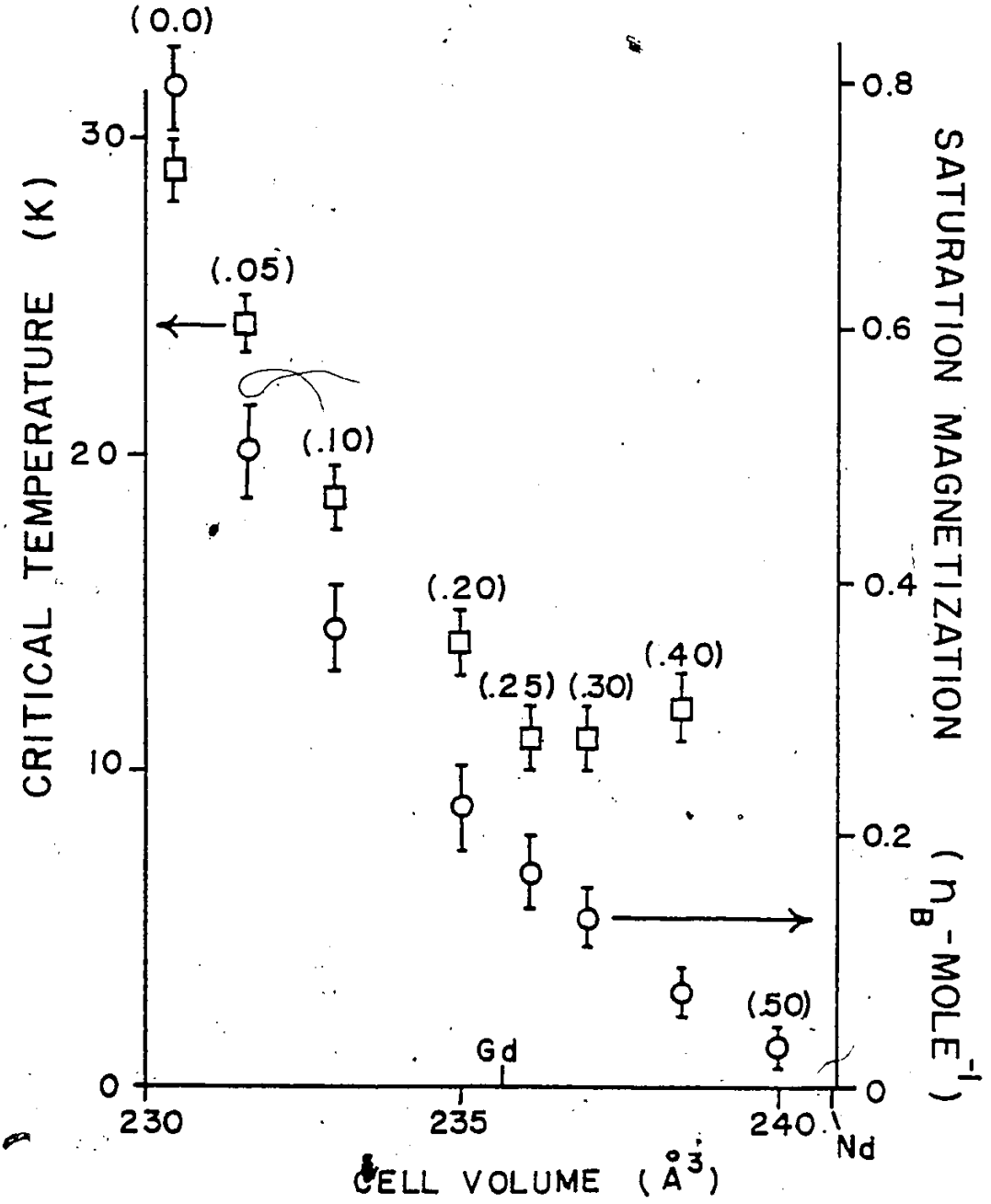

Figure 5-38. Critical temperatures and saturation moments at 4.2 K of various $La_xY_{1-x}TiO_3$ phases as a function of unit cell volume. The value of x is shown in brackets above the appropriate data points. The cell volume of $GdTiO_3$ is also indicated.

A more detailed study of the $La_xY_{1-x}TiO_3$ series is being conducted by another member of our group* at this time. That study involves the preparation of single crystal samples of various members of the series along with magnetic and transport measurements in an attempt to gain a fuller understanding of the properties of this series.

---

* J.P. Goral.

Chapter 6

CONCLUSIONS

6.1 The Present

Table 6-1 briefly summarizes some of the properties observed for the $RETiO_3$, RE = La, ..., Y. For RE = La, Ce, the Ti^{+3} d-electron appears to be best described on the delocalized electron model. For RE = Gd, Y, a local model seems more appropriate. The case for RE = Pr, Nd is more intermediate in nature, but appears to call for the local model. These findings suggest, then, that a change in the electronic behaviour of the Ti^{+3} d-electron occurs across the $RETiO_3$ series, RE = La, ..., Y.

The crystallographic studies of the $RETiO_3$ that have been reported in Chapter 3 provide a means of determining whether these findings agree qualitatively with the phenomenological phase diagram proposed for the $RETiO_3$ by Goodenough and shown in Figure 1-3. As discussed in section 1.4, the phase diagram related physical properties in different temperature regimes to the magnitude of the transfer integral, b. The magnitude of b is a measure of the strength of the interaction between neighbouring Ti^{+3} ions. The collective d-electron behaviour in $LaTiO_3$ and $CeTiO_3$ suggests that b is large ($b > b_m$ in Figure 1-3),

Table 6-1

RE in $RETiO_3$	Magnetic Properties	Electrical Conductivity	Optical Properties
La	T_c = 130 K, T > 130 K, Temperature Independent Paramagnetism T < 130 K, Complex, $\mu_{sat} \approx 10^{-3}\ \mu_B$	T > 130 K, metallic T < 130 K, semiconducting $E_g \approx 0.008$ eV	Opaque down to 6 meV
Ce	T_c = 116 K T > 116 K, Curie-Weiss plus temperature independent paramagnetic term T < 116 K, Complex	T > 60 K, metallic T < 60 K, semiconducting $E_g \approx 0.001$ eV	--
Pr	T_c = 96 K T > 96 K, Curie-Weiss, $C_M = 1.73\ cm^3\text{-K-mole}^{-1}$ T < 96 K, Complex	Semiconducting, $E_a \approx 0.04$ eV	--
Nd	Curie-Weiss, $C_M = 1.77\ cm^3\text{-K-mole}^{-1}$	Semiconducting $E_a \approx 0.03$ eV	Opaque down to 6 meV
Gd	T_c = 34 K, Ferrimagnet, $\mu_{sat} = 6.0\ \mu_B\text{-mole}^{-1}$	Semiconducting $E_a \approx 0.18$ eV	Transparent in IR
Y	T_c = 29 K, Ferromagnet, $\mu_{sat} = 0.85\ \mu_B\text{-mole}^{-1}$	--	Transparent in IR

while the localized d-electron behaviour in the $RETiO_3$, RE = Gd and Y, suggests that $b < b_c$ for those compounds. The case for RE = Pr, Nd is less clear as the magnetic evidence for localized electron behaviour in these compounds is not unambiguous.

As discussed in Chapter 1, the strength of the interaction between Ti^{+3} ions (and hence the magnitude of b) will depend upon the effectiveness of the overlap of the Ti^{+3} d-orbitals with the p-orbitals of the neighbouring oxygen atoms. This, in turn, will depend upon the angle subtended at the oxygen by the two neighbouring Ti^{+3} ions, since the Ti-atoms must interact via that intervening oxygen ion. When the Ti-O-Ti bond angle is 180°, as in the ideal perovskite structure, the overlap of the Ti-orbitals with the oxygen orbitals is maximal. If the Ti-O-Ti bond angle is decreased from 180° (as it is in the orthorhombically distorted perovskites), the overlap is less effective and hence the magnitude of b is lower. The Ti-O-Ti bond angle as a function of rare earth radius in the $RETiO_3$ is shown in Figure 3-8. In going from RE = La to RE = Y, the average Ti-O-Ti bond angle decreases from 155° to 143°, so that the value of the transfer integral, b, is presumably also decreasing. Based upon these qualitative arguments, it is possible that the values of b scan part of the phase diagram of Figure 1-3 from right to left as the rare earth changes from La to Y and in accord with the gross

features of Figure 1-3 one observes a transition from collective to localized behaviour for the d-electrons.

The phase diagram predicts that the first ordered phase encountered upon decreasing b will be an antiferromagnetic spiral. One interpretation of the properties of $LaTiO_3$ invokes an itinerant antiferromagnetic model. The phase diagram also predicts ferromagnetic ordering as b decreases, and this is found, unequivocally, for RE = Gd to Lu.

There are a number of observations, however, that are not predicted in detail by Figure 1-3. The variation of the critical temperatures across the $RETiO_3$ series, reported in Table 6-2, bears little resemblance to the behaviour predicted by the phase diagram. For example, T_c decreases from La to Pr rather than the predicted increase. There is also no way to understand a $T_c \approx 0K$ for RE = Nd or the considerable scatter from RE = Gd to Lu. The $La_xY_{1-x}TiO_3$ series, which, in principle, should be well represented by the phase diagram as there are no "interfering" moments on the rare earth atoms, shown an initial rapid decrease in T_c with increasing x, (increasing b), rather than the expected increase.

Interactions of the titanium d-electrons with the rare earth ions are outside the scope of Goodenough's model, in that it applies only to the d-electrons. These inter-

Table 6-2

Magnetic Critical Temperatures for the $RETiO_3$ *

RE in $RETiO_3$	T_c(K)	RE in $RETiO_3$	T_c(K)
La	130	$La_{1.0}Y_{0.0}$	130
Ce	116	$La_{0.5}Y_{0.5}$	
Pr	96	$La_{0.4}Y_{0.6}$	12
Nd	< 1.2	$La_{0.3}Y_{0.7}$	11
Gd	34	$La_{0.25}Y_{0.75}$	11
Tb	49	$La_{0.2}Y_{0.8}$	14
Dy	64	$La_{0.1}Y_{0.9}$	18
Ho	56	$La_{0.05}Y_{0.95}$	24
Y	29	$La_{0.0}Y_{1.0}$	29
Er	39		
Tm	58		
Lu	30		

* Critical temperatures for those $RETiO_3$ not studied in this work taken from reference 71.

actions are clearly important in $GdTiO_3$, where ferrimagnetic ordering occurs, and may be important in $CeTiO_3$ and $PrTiO_3$, where complicated magnetic behaviour is observed.

As has been mentioned briefly in section 5.2, the number of titanium d-electrons per unit cell for the $RETiO_3$ is four, not just one as would be the case for a cubic perovskite cell. This means that for the case of delocalized d-electron behaviour, it may be possible to have a band semiconductor. This possibility does not exist in Goodenough's approach, which focuses upon a single pseudo-perovskite cell and predicts only metallic behaviour for delocalized electrons. If the change from metallic to semiconducting resistivity in $LaTiO_3$ and $CeTiO_3$ results from a metal-collective-electron semiconductor transition, this, too, is neither predicted nor explainable on the basis of Goodenough's model.

It is interesting to note the correlation between the standard deviation of the Ti-O bond lengths in the $RETiO_3$ (see Fig. 3-7) with certain physical properties. For RE = La (collective d-electrons), σ(Ti-O) $\approx$ 0. For RE = Gd and Y, where localized d-electron behaviour is observed, σ(Ti-O) is relatively large. σ(Ti-O) is smaller for RE = Pr, Nd, for which there is only indirect evidence for a full local moment on titanium. It is also interesting that when RE = Pr, Nd (small σ(Ti-O)) activation energies for conduction are small, while for RE = Gd, Y (large σ(Ti-O)),

the activation energies are significantly larger.

The findings of this work have differed significantly in a number of details from the previously reported results of other workers (i.e., Bazuev et al. and Ganguly et al.). Many of the experiments reported in this work were performed for the first time on single crystals of the $RETiO_3$, and are more likely to reflect the true properties of these materials better than measurements on polycrystalline samples. As well, many of these experiments have extended to lower temperature the range over which these materials have been studied, and, in doing so, have revealed many unusual low temperature properties which could not have been predicted from data obtained at higher temperatures.

6.2 The Future

This work has opened numerous potential avenues for further examination.

All of the materials studied in this thesis are candidates for Hall effect experiments. Such studies should reveal the sign and concentration of the charge carriers, and in conjunction with resistivity data, can be used to determine charge carrier mobilities. The temperature dependence of the Hall mobility provides a critical experiment to distinguish the collective from the localized electron regime.

Diffuse reflectance studies of the $RETiO_3$,

RE = Pr, Nd, Gd and Y, may reveal absorptions at $\sim$ 19,000 cm^{-1} due to d-d transitions between levels of T_2 symmetry and E symmetry in the Ti^{+3} ion.

Neutron diffraction studies of the materials $CeTiO_3$ and $PrTiO_3$ may reveal fascinating magnetic structures. It will be of interest to examine the magnetic structures at different temperatures, as the undulations in the low field magnetization versus temperature plots for these compounds suggest changes in the magnetic structure with temperature.

The interesting properties of the $La_xY_{1-x}TiO_3$ series warrant further study. The first step should involve the preparation of single crystal samples which could then be used for transport and optical studies.

It should be possible to put the delocalized-localized electron transition on a more quantitative footing. The interatomic distances and angles in the $RETiO_3$ are now well known from this work. Band calculations on $LaTiO_3$ and $CeTiO_3$ would be valuable, the results of which may clear up some of the confusion regarding these materials. It may also be possible to calculate the relevant overlap integrals, and perhaps estimate values for the transfer integrals for the individual $RETiO_3$.

APPENDIX

Observed (FO) and Calculated (FC) structure factor amplitudes for the $RETiO_3$, RE = La, Nd, Sm, Gd and Y.

STRUCTURE FACTORS TABLE FOR LA TI O3

(UNOBSERVED REFLECTIONS ARE MARKED +)

H	K	L	FO	FC	H	K	L	FO	FC	H	K	L	FO	FC	H	K	L	FO	FC	H	K	L	FO	FC
0	2	1	77	73	1	4	10	8	5	2	5	0	4+	2	3	6	2	3+	2	4	7	2	3+	5
0	2	3	83	79	1	5	1	95	94	2	5	2	5	7	3	6	3	5	6	4	7	3	5+	1
0	2	5	47	47	1	5	3	89	89	2	5	3	1+	3	3	6	4	12	13	4	7	4	5	6
0	2	7	52	52	1	5	5	75	76	2	5	4	4	3	3	6	6	5	6	4	8	1	44	42
0	2	9	30	31	1	5	7	65	65	2	5	6	4	4	3	6	8	4	4	5	0	-5	15	15
0	2	11	28	27	1	5	9	51	51	2	5	8	5	4	3	7	1	58	59	5	1	1	25	20
0	4	1	105	102	1	6	0	9	9	2	6	1	78	79	3	7	3	54	55	5	1	3	29	30
0	4	3	81	79	1	6	2	15	15	2	6	3	64	65	3	7	5	52	50	5	1	5	12	10
0	4	5	89	90	1	6	5	2+	2	2	6	5	70	72	3	8	0	4+	1	5	1	7	22	23
0	4	7	55	55	1	6	6	3+	4	2	6	7	48	47	3	8	2	12	11	5	1	9	5	8
0	4	9	56	56	1	6	8	3+	4	2	6	9	50	48	3	8	4	4+	3	5	2	0	5	7
0	4	11	38	37	1	7	1	68	68	2	8	1	46	45	4	1	0	23	22	5	2	2	10	11
0	6	1	77	77	1	7	3	65	64	2	8	3	50	48	4	1	2	12	10	5	2	-3	12	12
0	-6	3	80	84	1	7	5	59	56	2	8	5	36	35	4	1	-3	27	28	5	2	4	6	7
0	6	5	57	58	1	7	7	52	48	3	0	-3	15	14	4	1	4	10	11	5	2	6	5	7
0	6	7	66	65	1	8	0	12	10	3	1	1	38	39	4	1	10	3+	5	5	2	8	3+	6
0	6	9	42	41	1	8	2	1+	4	3	1	3	22	20	4	2	1	54	51	5	2	10	5	3
0	8	1	53	50	1	8	4	4+	6	3	1	5	36	37	4	2	3	53	52	5	3	1	58	58
0	8	3	43	40	2	1	0	18	17	3	1	7	12	13	4	2	5	40	39	5	3	3	47	47
0	8	5	50	47	2	1	1	33	31	3	1	9	19	20	4	2	7	38	37	5	3	5	52	53
1	0	-1	11	7	2	1	2	19	17	3	1	11	9	10	4	2	9	25	26	5	3	7	34	34
1	1	1	47	43	2	-1	-3	23	21	3	2	0	18	18	4	2	11	22	22	5	3	9	37	35
1	1	3	49	45	2	1	8	6	3	3	2	-1	4	3	4	3	0	3+	1	5	4	0	17	17
1	1	5	28	26	2	1	10	5+	1	3	2	4	12	11	4	3	-1	20	22	5	4	-1	5+	3
1	1	7	28	28	2	1	12	3+	3	3	2	-5	13	12	4	3	2	19	18	5	4	2	11	10
1	1	9	16	17	2	2	1	75	72	3	2	6	2+	5	4	3	4	4+	4	5	4	4	12	13
1	1	11	16	14	2	2	3	56	55	3	2	10	5	5	4	3	6	11	8	5	4	6	11	9
1	2	0	17	16	2	2	5	59	60	3	3	1	77	75	4	3	8	8	8	5	4	8	5	8
1	2	1	18	12	2	2	7	36	37	3	3	3	79	78	4	3	10	5+	2	5	5	1	59	68
1	2	2	21	19	2	2	9	34	36	3	3	5	55	55	4	4	1	76	76	5	5	3	58	59
1	-2	-3	20	15	2	2	11	23	23	3	3	7	54	56	4	4	3	65	65	5	5	5	49	49
1	2	4	1+	4	2	3	0	16	15	3	3	9	38	37	4	4	5	64	66	5	5	7	46	46
1	2	8	6	3	2	3	1	18	17	3	3	11	33	32	4	4	7	47	47	5	6	0	7	9
1	2	10	3+	1	2	3	2	3+	2	3	4	1	6	5	4	4	9	44	43	5	6	1	4+	3
1	2	12	2+	3	2	3	4	8	6	3	4	2	21	20	4	5	0	11	13	5	6	2	15	14
1	3	1	100	97	2	-3	5	10	7	3	4	4	0+	5	4	5	1	8	7	5	6	4	9	9
1	3	3	85	83	2	3	6	5	3	3	4	6	10	9	4	5	2	5	7	5	6	6	11	9
1	3	5	78	76	2	3	8	1+	2	3	4	8	7	8	4	5	4	11	10	5	7	1	46	45
1	3	7	55	57	2	3	10	5	4	3	4	10	1+	2	4	5	6	8	7	5	7	3	44	43
1	3	9	47	47	2	4	1	88	87	3	5	1	80	81	4	5	8	6	6	6	1	0	9	6
1	3	11	36	34	2	4	3	93	93	3	5	3	73	74	4	6	1	63	63	6	1	2	15	14
1	4	0	24	24	2	4	5	61	64	3	5	5	67	69	4	6	3	64	64	6	1	-5	17	18
1	4	2	10	11	2	4	7	66	68	3	5	7	53	54	4	6	5	50	50	6	2	1	38	37
1	4	3	10	9	2	4	9	43	44	3	5	9	49	46	4	6	7	50	50	6	2	3	36	34
1	4	4	13	12	2	4	11	39	39	3	6	0	18	18	4	7	0	6	7	6	2	5	31	31

STRUCTURE FACTORS TABLE FOR LA TI 03

H	K	L	FO	FC	H	K	L	FO	FC	H	K	L	FO	FC	H	K	L	FO	FC	H	K	L	FO	FC
6	2	7	27	25	6	4	7	40	39	7	1	3	16	9	7	3	3	40	40	8	1	2	3+	1
6	2	9	22	21	6	5	0	10	10	7	1	5	19	19	7	3	5	28	28	8	1	4	9	7
6	3	0	19	19	6	5	-1	4+	6	7	1	7	9	6	7	4	0	14	13	8	2	1	27	24
6	3	2	6	5	6	5	2	12	14	7	2	0	10	7	7	4	2	10	11	8	2	3	22	22
6	3	-3	19	16	6	5	4	12	10	7	2	2	9	8	7	4	-3	7	7	8	2	5	21	21
6	3	4	13	14	6	5	6	10	10	7	2	4	6	7	7	4	4	11	11	8	3	0	8	7
6	3	6	3+	8	6	6	1	49	49	7	2	-5	10	13	7	5	1	42	43	8	3	2	16	14
6	4	1	54	54	6	6	3	46	46	7	2	6	4+	6	7	5	3	39	39	8	3	4	9	7
6	4	3	49	51	7	0	-7	12	13	7	3	1	36	37	8	1	0	12	10	8	4	1	35	35
6	4	5	44	45	7	1	1	22	17															

STRUCTURE FACTORS TABLE FOR HO FI 03

PAGE 2 OF 2

STRUCTURE FACTORS TABLE FOR SM TI OS

(UNOBSERVED REFLECTIONS ARE MARKED +)
(UNRELIABLE REFLECTIONS ARE MARKED U)

STRUCTURE FACTORS FOR SH T1 03

PAGE 2 OF 2

H	K	L	FO	FC
0	0	2	44	43
0	0	4	38	38
0	0	6	11	9
0	0	8	26	28
0	0	10	6	6
0	0	12	26	26
0	0	14	6	6
0	0	16	33	33
0	0	18	13	13
0	0	20	23	24
0	0	22	35	35
0	0	24	7	7
0	0	26	45	45
0	0	28	32	32
0	0	30	27	27
0	0	32	37	37
0	0	34	35	35
0	0	36	26	26
0	0	38	33	33
0	0	40	16	16
0	0	42	35	35
0	0	44	26	26
0	0	46	35	35
0	0	48	22	22
0	0	50	42	42
0	0	52	55	55
0	0	54	35	35
0	0	56	30	30
0	0	58	22	22
0	0	60	45	45
0	0	62	35	35
0	0	64	27	27
0	0	66	32	32
0	0	68	35	35
0	0	70	27	27
0	0	72	32	32
0	0	74	27	27
0	0	76	32	32
0	0	78	27	27
0	0	80	32	32
0	0

STRUCTURE FACTORS TABLE FOR GD T1 03

(UNOBSERVED REFLECTIONS ARE MARKED +)

H	K	L	FO	FC	H	K	L	FO	FC	H	K	L	FO	FC	H	K	L	FO	FC	H	K	L	FO	FC
4	3	4	56	43	4	5	3	16	17	5	1	6	109	109	5	4	0	54	55	6	1	3	53	54
4	3	5	25	25	4	5	4	33	33	5	2	0	55	55	5	4	1	11	10	6	1	4	26	27
4	3	6	41	42	4	6	0	49	48	5	2	1	46	46	5	4	2	53	57	6	1	5	55	55
4	3	7	5+	5	4	6	1	46	46	5	2	2	49	49	5	4	3	12	10	6	2	0	74	73
4	4	0	12	11	5	0	1	73	74	5	2	3	41	41	5	4	4	51	51	6	2	1	61	60
4	4	1	109	103	5	0	3	71	72	5	2	4	40	40	5	5	0	58	57	6	2	2	22	23
4	4	2	54	54	5	0	5	61	61	5	2	5	40	40	5	5	1	62	61	6	2	3	63	63
4	4	3	100	100	5	0	7	55	55	5	2	6	42	42	5	5	2	23	24	6	2	4	70	70
4	4	4	9	3	5	1	0	76	74	5	3	0	16	13	6	0	0	118	116	6	3	0	71	72
4	4	5	35	34	5	1	1	38	37	5	3	1	08	09	6	0	2	44	44	6	3	1	10	9
4	4	6	43	44	5	1	2	128	126	5	3	2	69	69	6	0	4	100	101	6	3	2	62	61
4	5	0	34	34	5	1	3	53	53	5	3	3	77	70	6	1	0	20	21	6	3	3	19	19
4	5	1	33	32	5	1	4	62	62	5	3	4	11+	3	6	1	1	61	61	-7	0	1	76	76
4	5	2	39	38	5	1	5	24	24	5	3	5	01	01	6	1	2	39	40					

STRUCTURE FACTORS TABLE FOR Y TI 03

(UNOBSERVED REFLECTIONS ARE MARKED +)

H	K	L	FO	FC	H	K	L	FO	FC	H	K	L	FO	FC	H	K	L	FO	FC	H	K	L	FO	FC
0	0	2	36	37	1	2	1	16	14	2	0	6	22	22	2	6	1	24	24	3	5	0	82	80
0	0	4	143	146	1	2	2	37	35	2	1	0	94	93	2	6	2	76	76	3	5	1	36	36
0	0	6	56	56	1	2	3	18	17	2	1	1	23	20	2	6	3	13	13	3	5	2	11	9
0	0	8	83	84	1	2	4	12	11	2	1	2	49	47	2	6	4	21	20	3	5	3	40	39
0	0	10	106	105	1	2	5	15	16	2	1	3	25	24	2	6	5	26	24	3	5	4	62	62
0	2	1	64	63	1	2	6	4+	3	2	1	4	31	30	2	6	6	14	14	3	5	5	30	29
0	2	2	46	43	1	2	7	7	5	2	1	5	3+	4	2	7	0	16	16	3	6	0	16	17
0	2	3	84	85	1	2	8	15	16	2	1	6	32	33	3	0	1	17	18	3	6	1	21	20
0	2	4	104	107	1	2	9	7+	1	2	1	7	7+	2	3	0	3	31	31	3	6	2	10	8
0	2	5	41	41	1	3	0	55	54	2	1	8	20	20	3	0	5	10	12	3	6	3	16	16
0	2	6	10	6	1	3	1	96	96	2	1	9	13	12	3	0	7	19	19	3	6	4	96	97
0	2	7	51	52	1	3	2	65	66	2	1	10	16	16	3	0	9	25	24	3	6	5	13	14
0	2	8	80	81	1	3	3	82	83	2	2	0	122	120	3	1	1	44	43	3	6	6	82	84
0	2	9	38	33	1	3	4	35	35	2	2	1	78	77	3	1	2	123	124	3	6	7	14	13
0	4	0	32	33	1	3	5	74	76	2	2	2	12	12	3	1	3	11	13	3	6	8	62	61
0	4	1	75	76	1	3	6	40	40	2	2	3	53	53	3	1	4	27	27	3	7	0	35	37
0	4	2	58	53	1	3	7	60	59	2	2	4	87	90	3	1	5	41	41	3	7	1	31	31
0	4	3	44	45	1	3	8	19	19	2	2	5	63	64	3	1	6	85	87	3	7	2	2+	3
0	4	4	24	25	1	4	0	40	40	2	2	6	8	9	3	1	7	16	15	3	7	3	37	38
0	4	5	70	71	1	4	1	4+	6	2	2	7	41	41	3	1	8	22	21	4	0	4	13	16
0	4	6	44	44	1	4	2	7+	1	2	2	8	56	54	3	2	0	40	39	4	0	5	23	22
0	4	7	41	40	1	4	3	9	8	2	2	9	36	35	3	2	1	14	13	4	0	6	21	19
0	4	8	18	18	1	4	4	16	16	2	3	0	21	20	3	2	2	25	24	4	0	7	27	27
0	6	0	18	17	1	4	5	6+	4	2	3	1	3+	7	3	2	3	2+	4	4	0	8	67	67
0	6	1	14	12	1	4	6	20	19	2	3	2	4+	7	3	2	4	26	26	4	1	0	53	54
0	6	2	92	93	1	4	7	5+	4	2	3	3	24	25	3	2	5	14	15	4	1	1	9	10
0	6	3	25	25	1	4	8	10	1	2	3	4	11	12	3	2	6	23	24	4	1	2	51	51
0	6	4	22	21	1	5	0	78	76	2	3	5	12	12	3	2	7	7+	5	4	1	3	59	60
0	6	5	3+	5	1	5	1	58	59	2	3	6	12	12	3	2	8	14	14	4	1	4	43	43
1	0	1	17	15	1	5	2	13	15	2	3	7	12	5	3	3	0	3+	4	4	1	5	9	9
1	1	3	37	34	1	5	3	52	53	2	3	8	20	21	3	3	1	60	61	4	1	6	36	37
1	1	5	25	25	1	5	4	74	74	2	4	0	64	64	3	3	2	46	46	4	2	0	25	25
1	1	7	8	7	1	5	5	49	50	2	4	1	55	56	3	3	3	65	66	4	2	1	13	12
1	1	9	11	1	1	5	6	5+	7	2	4	2	75	76	3	3	4	18	18	4	2	2	36	37
1	1	0	28	27	1	5	7	40	40	2	4	3	21	20	3	3	5	47	47	4	2	3	6	6
1	1	1	52	49	1	6	1	4+	4	2	4	4	47	46	3	3	6	51	51	4	2	4	28	28
1	1	2	123	120	1	6	2	15	15	2	4	5	46	46	3	3	7	46	47	4	2	5	16	16
1	1	3	59	53	1	6	3	13	14	2	4	6	54	53	3	4	0	24	23	4	2	6	21	21
1	1	4	20	20	1	6	4	4+	6	2	4	7	7	8	3	4	1	10	11	4	2	7	3+	1
1	1	5	30	30	1	6	5	8+	1	2	5	0	7+	5	3	4	2	37	36	4	3	0	18	16
1	1	6	94	96	1	7	0	82	81	2	5	1	5+	2	3	4	3	8	9	4	3	1	59	58
1	1	7	33	33	1	7	1	21	22	2	5	2	17	17	3	4	4	26	26	4	3	2	48	49
1	1	8	13	14	2	0	0	123	118	2	5	3	6+	4	3	4	5	8	9	4	3	3	54	53
1	1	9	23	24	2	0	2	62	61	2	5	4	4+	5	3	4	6	20	20	4	3	4	16	14
1	2	0	11	9	2	0	4	117	120	2	5	6	29	28	3	4	7	8	7	4	3	5	50	50

STRUCTURE FACTORS TABLE FOR Y TI 03

H	K	L	FO	FC	H	K	L	FO	FC	H	K	L	FO	FC	H	K	L	FO	FC	H	K	L	FO	FC
4	4	6	40	40	5	1	1	16	15	5	2	5	25	25	5	4	3	10	7	6	1	3	22	24
4	5	0	13	16	5	1	2	75	79	5	2	6	23	23	5	4	4	25	25	6	1	4	17	16
4	5	1	22	23	5	1	3	30	31	5	3	0	30	30	5	5	0	41	40	6	2	0	44	45
4	5	2	23	22	5	1	4	16	16	5	3	1	44	43	5	5	1	26	26	6	2	1	28	28
4	5	3	8	7	5	1	5	3+	6	5	3	2	52	52	6	0	0	75	75	6	2	2	7+	4
4	5	4	17	17	5	1	6	70	69	5	3	3	34	34	6	0	2	8	7	6	2	3	33	33
4	6	0	14	14	5	2	0	31	31	5	3	4	19	18	6	0	4	62	61	6	2	4	46	45
5	0	1	43	43	5	2	1	27	28	5	3	5	40	40	6	1	0	10	9	6	3	0	43	43
5	0	3	45	45	5	2	2	25	24	5	4	0	26	24	6	1	1	29	29	6	3	1	2+	1
5	0	5	34	34	5	2	3	21	22	5	4	1	4+	6	6	1	2	24	25	6	3	2	35	34
5	1	0	25	24	5	2	4	25	25	5	4	2	31	30										

REFERENCES

1. J.B. Goodenough, Magnetism and the Chemical Bond, Interscience Publishers, New York, 1963.
2. J.B. Goodenough, Prog. Solid State Chem. 5, 145 (1971).
3. J.B. Goodenough, J. Appl. Phys. 37, 1415 (1966).
4. J.B. Goodenough, Czech. J. Phys. B17, 304 (1967).
5. P.M. Raccah and J.B. Goodenough, Phys. Rev. 155, 155 (1967).
6. C.N.R. Rao and G.V. Subba Rao, Phys. Status Solidi A 1, 597 (1970).
7. D. Adler, Solid State Physics 21, 1 (1968).
8. C.N.R. Rao, J. Indian Chem. Soc. 51, 979 (1974).
9. C. Kittel, Introduction to Solid State Physics, 4th ed., J. Wiley and Sons, Inc., New York, 1971.
10. N.W. Ashcroft and N.D. Mermin, Solid State Physics, Holt, Rinehart and Winston, New York, 1976.
11. T. Holstein, Ann. Phys. 8, 343 (1959).
12. I.G. Austin and N.F. Mott, Adv. Phys. 18, 41 (1968).
13. N.F. Mott, Metal-Insulator Transitions, Taylor and Francis, London, 1974.
14. O. Madelung, Introduction to the Solid State, Springer-Verlag, Heidelberg, 1978.
15. D. Adler, Rev. Modern Phys. 40, 714 (1968).
16. I.G. Austin and N.F. Mott, Science 168, 71 (1970).
17. J.M. Honig and L.L. Van Zandt, Annu. Rev. Mater. Sci. 5, 225 (1975).
18. L.L. Van Zandt and J.M. Honig, Annu. Rev. Mater. Sci. 4, 191 (1974).

19. J.B. Goodenough and J.M. Longo, Crystallographic and Magnetic Properties of Perovskite and Perovskite-Related Compounds, Landolt-Bornstein Tabellen, New Series III/4a, Springer-Verlag, Berlin, 1970.

20. P. Ganguly, O. Parkash and C.N.R. Rao, Phys. Status Solidi A 36, 669 (1976).

21. M. Kestigian and R. Ward, J. Am. Chem. Soc. 76, 6027 (1954).

22. W.D. Johnston and D. Sestrich, J. Inorg. Nucl. Chem. 20, 32 (1961).

23. V.H. Holzapfel and J. Sieler, Z. Anorg. Allg. Chem. 343, 174 (1966).

24. G.J. McCarthy, W.B. White and R. Roy, Mater. Res. Bull. 4, 251 (1969).

25. G.V. Bazuev, V.A. Perelyaev and G.P. Shveikin, Izv. Akad. Nauk. SSSR, Neorg. Mater. 10, 1066 (1974).

26. G.V. Bazuev and G.P. Shveikin, Izv. Akad. Nauk SSSR, Neorg. Mater. 14, 267 (1978).

27. G.V. Bazuev, O.V. Makarova and G.P. Shveikin, Zh. Neorg. Khim. 23, 1451 (1978).

28. M. Kestigian and R. Ward, J. Am. Chem. Soc. 77, 6199 (1955).

29. L.H. Brixner, Inorg. Chem. 3, 1065 (1964).

30. D.C. Stockbarger, Rev. Sci. Instrum. 7, 133 (1936).

31. R.A. Laudise, The Growth of Single Crystals, Prentice-Hall, New Jersey, 1970.

32. J. Czochralski, Z. Phys. Chem. (Leipzig) 92, 219 (1917).

33. T.B. Reed and E.R. Pollard, J. Crys. Growth 2, 243 (1968).

34. B.C. Tofield and W.R. Scott, Jr. Solid State Chem. 10, 183 (1974).

35. B.T.M. Willis in Thermodynamic and Transport Properties of Uranium Dioxide and Related Phases, Chapter II, International Atomic Energy Agency, Vienna, 1965.

36. H.E. Swanson, National Bureau of Standards Circular, Monograph 25, Section 1-8, 1962-70.

37. H.F. Kay and P.C. Bailey, Acta Crystallogr. 10, 219 (1957).

38. S. Geller, J. Chem. Phys. 24, 1236 (1956).

39. S. Geller and E.A. Wood, Acta Crystallogr. 9, 563 (1956).

40. E.F. Bertaut and F. Forrat, J. Phys. Radium 17, 129 (1956).

41. G.P. Shveikin and G.V. Bazuev, Z. Neorg. Khim. 18, 291 (1973).

42. M. Marezio and P.D. Dernier, Mater. Res. Bull. 6, 23 (1971).

43. D.T. Cromer and J.T. Waber, Acta Crystallogr. 18, 104 (1965).

44. D.T. Cromer, Acta Crystallogr. 18, 17 (1965).

45. M. Marezio, J.P. Remeika and P.D. Dernier, Acta Crystallogr. B 26, 2008 (1970).

46. R.D. Shannon and C.T. Prewitt, Acta Crystallogr. B 25, 925 (1969).

47. P.W. Selwood, Magnetochemistry, 2nd ed., Interscience, New York, 1956.

48. J. Crangle and G.M. Goodman, Proc. Royal Soc. London A 321, 477 (1971).

49. L.J. Van der Pauw, Philips Res. Repts. 13, 1 (1958).

50. H. Navarro, Ph.D. Thesis, McMaster Univeristy, 1980.

51. D.B. Rogers, A. Ferretti, D.H. Ridgley, R.J. Arnott and J.B. Goodenough, J. Appl. Phys. 37, 1431 (1966).

52. D.S. Rajoria, V.G. Bhide, G. Rama Rao and C.N.R. Rao, J. Chem. Soc., Faraday Trans. 70, 512 (1974).

53. W. Werner, Thesis, Technische Universität, Berlin, 1965.

54. G.V. Bazuev, N.N. Iutin, I.I. Natveenko and G.P. Shveikin, Fiz. Tverd. Tela 17, 1167 (1975).

55. R.M. Bozorth, H.J. Williams and D.E. Walsh, Phys. Rev. 103, 572 (1956).

56. D. Johnston, Ph.D. Thesis, University of California, San Diego, 1975.

57. R.D. Shannon, B.E. Taylor, A.D. English and T. Berzins, Electrochim. Acta 22, 783 (1977).

58. R.D. Shannon, Inorg. Chem. 17, 958 (1978).

59. T.A. Bither, J.L. Gillson and H.S. Young, Inorg. Chem. 5, 1559 (1966).

60. J.T. Last, Phys. Rev. 105, 1740 (1957).

61. M. Couzi and P.V. Huong, J. Chim. Phys. Phys. Chim. Biol. 69, 1339 (1972).

62. G.V. Bazeuv and G.P. Shveikin, Izv. Akad. Nauk SSSR, Neorg. Mater. 11, 2195 (1975).

63. B.L. Chamberland, Solid State Commun. 5, 663 (1967).

64. A.J. Heeger, Solid State Phys. 23, 284 (1969).

65. W.M. Star in Magnetism, Selected Topics, S. Foner, ed., Gordon and Breach, New York, 1976, p. 173.

66. J.P. Franck, Proc. Royal Soc. A 263, 494 (1961).

67. D. Taylor, New Scientist 3, 513 (1976).

68. N.B. Hannay in Semiconductors, N.B. Hannay, ed., Reinholt, New York, 1960, p. 32.

69. D.R. Lovett, Semimetals and Narrow Bandgap Semiconductors, Pion, 1977.

70. W.M. Yim and A. Amith, Solid State Electron. 15, 1141 (1972).

71. C.W. Turner and J.E. Greedan, J. Solid State Chem., in press.

72. P. Dougier, J.C.C. Fan and J.B. Goodenough, J. Solid State Chem. 14, 247 (1975).

73. J.B. Goodenough, J.M. Longo and J.A. Kafalas, Mater. Res. Bull. 3, 471 (1968).

74. J.C. Slater, Phys. Rev. 82, 538 (1951).

75. M.M. Schieber, Experimental Magnetochemistry, J. Wiley and Sons, New York, 1967.

76. G.A. Candela, A.H. Kahn, T. Negas and C.L. McDaniel in The Rare Earths in Modern Science and Technology, G.J. McCarthy and J.J. Rhyne, eds., Plenum Press, New York, 1978, p. 441.

77. A.C. Larson, Acta Crystallogr. 23, 664 (1967).

78. V.V. Kazantsev, V.I. Rogovich, E.I. Krylov, A.T. Chupin and A.K. Borisov, Izv. Akad. Nauk SSSR, Neorg. Mater.

11, 2006 (1975).

79. R.M. Bozorth, Phys. Rev. Lett. 1, 362 (1958).

80. R.M. Bozorth, V. Kramer and J.P. Remeika, Phys. Rev. Lett. 1, 3 (1958).

81. G.V. Subba Rao, B.M. Wanklyn and C.N.R. Rao, J. Phys. Chem. Solids 32, 345 (1971).

82. H.L. Tuller and A.S. Nowick, J. Phys. Chem. Solids 38, 859 (1977).

83. L.G. Shcherbakova, L.G. Mamsurova and G.E. Sukhanova, Usp. Khim. 48, 423 (1979).

84. D. Adler and J. Feinleib, Phys. Rev. B 2, 3112 (1970).

85. J. Appel, Solid State Phys. 21, 193 (1968).

86. L. Friedman, Phys. Rev. 135, 233 (1964).

87. P. Gerthsen, R. Groth, K.H. Hardtl, D. Heese and H.G. Reik, Solid State Commun. 3, 165 (1965).

88. H.G. Reik and R. Mühlstroh, Solid State Commun. 5, 105 (1967).

89. G. Zaraté, private communication.

90. B.D. Cullity, Introduction to Magnetic Materials, Addison Wesley, Reading, Mass., 1972.

91. J.S. Smart, Effective Field Theories of Magnetism, W.B. Saunders, Philadelphia and London, 1966.

92. L. Néel, Ann. Phys. (Paris) 3, 137 (1948).

93. E.F. Bertaut, J. Mareschal, G. de Vries, R. Aléonard, R. Pautlenet, J.P. Rebouillat and V. Zarubicka, IEEE Trans. Magn. MAG-2, 453 (1966).

94. J.W. Orton, Electron Paramagnetic Resonance, Gordon and Breach, New York, 1968.

95. C.J. Ballhausen, Introduction to Ligand Field Theory, McGraw-Hill, New York, 1962.

96. J.S. Griffith, The Theory of Transition Metal Ions, Cambridge University Press, 1961, p. 437.

97. F.E. Mabbs and D.J. Machin, Magnetism and Transition Metal Complexes, Chapman and Hall, London, 1973.

98. E.D. Nelson, J.Y. Wong and A.L. Schawlow in Optical Properties of Ions in Crystals, H.M. Crosswhite and H.W. Moos, eds., Interscience, New York, 1967, p. 375.

99. A. Carrington and A.D. McLachlan, Introduction to Magnetic Resonance, Harper and Row, New York, Evanston and London, 1967, p. 157.

100. H.R. Child, M.K. Wilkinain, J.W. Cobb, W.L. Koehler and E.O. Wollan, Phys. Rev. 131, 922 (1963).

101. B.R. Cooper, J. Appl. Phys. 40, 1344 (1969).

102. Y.L. Wang and B.R. Cooper, Phys. Rev. 172, 539 (1968).